

Near-Real-Time GPS Sensing of Atmospheric Water Vapour

by

Zhengdong Bai

B.A., Tongji University, People's Republic of China, 1990

M.S., Tongji University, People's Republic of China, 1993

A thesis submitted to
the Faculty of Built Environment and Engineering
in partial fulfilment of
the requirements for the degree of
Doctor of Philosophy

Cooperative Research Centre for Satellite Systems
Queensland University of Technology
G.P.O. Box 2434, QLD 4001, Australia

April 2004

Abstract

An important goal in modern weather prediction is to improve short-term weather forecasts, especially of severe weather and precipitation. However, the ability to achieve this goal is hindered by the lack of timely and accurate observations of atmospheric water vapour, which is one of the most poorly measured and least understood constituents of the Earth's atmosphere due to its high temporal and spatial variability. This situation is being addressed by the Global Positioning System (GPS) technology. GPS radio signals are slowed and bent by changes in temperature, pressure and water vapour in the atmosphere. Traditionally, the GPS signal propagation delay is considered a nuisance parameter that is an impediment to obtaining precise coordinates using GPS. Recent development in GPS precise positioning and orbit determination has enabled the atmospheric parameters to be determined to a high degree of accuracy on a routine basis, using continuous tracking data from ground-based GPS receivers.

The aim of this research is to address several critical scientific challenges in estimating the atmospheric water vapour content in near-real-time (NRT) in Australia. Contributions are made to the field of GPS meteorology in the following five areas:

First of all, research efforts were made to develop a technical platform for the ground-based GPS meteorology studies and demonstration of GPS Precipitable Water Vapour (PWV) estimation using observations from Australian Regional GPS Networks (ARGN). Methods of estimation of water vapour from GPS and radiosonde data have been developed and tested. GAMIT-based GPS data processing strategies and compare analysis with radiosonde water vapour solutions from the Australia Upper Air Network (AUAN) were undertaken, providing an effective technical basis for further studies.

Secondly, the research has developed techniques to allow estimation of atmospheric water vapour from GPS data and surface meteorological observations collected around the GPS sites. Ideally a dedicated meteorological sensor is installed adjacent

to the GPS antenna. However, meteorological sensors are normally not installed at most Australian GPS stations. Installing a new meteorological sensor at each GPS station would involve additional cost at the level of one-third or half of the geodetic GPS receiver cost. We have experimentally developed and demonstrated interpolation methods for making use of hourly collected surface meteorological data from the Australian Automatic Weather Station (AWS) network operated by the Bureau of Meteorology (BOM) to estimate atmospheric water vapour.

Thirdly, the research has studied ocean tidal loading and its effects on GPS derived precipitable water vapour estimates. The periodic motion of the Earth's surface due to ocean loading is one of the largest periodic motions. However, very little work has been done to quantify their effects on GPS-derived solutions at the GPS sites in the Australian region surrounded by ocean waters. The research presents the theoretical analysis and experimental results from the ARGN network, focusing on ocean loading and its effects on GPS derived precipitable water vapour estimates.

The fourth important effort was the development of techniques for estimating high-rate Slant Water Vapour (SWV) values for future operational meteorological applications in Australia, including addressing such issues as slant-path delay recovery from post-fit double-difference residuals, and overcoming site multipath effects. The experimental results have demonstrated the efficiency of the proposed methods.

Finally, in order to address the meteorological applications with the existing and anticipated GPS reference stations in the Australian region, and measure the atmospheric water vapour content in near-real-time, the technical issues to implement NRT GPS water vapour estimation were identified and discussed, including the data requirements for meteorological and climate applications, NRT data processing and quality control procedures for GPS orbits. The experimental GPS PWV results from NRT and post data processing are compared and presented.

Table of Contents

Abstract.....	i
List of Figures.....	vii
List of Tables.....	x
List of Symbols.....	xii
List of Acronyms.....	xvii
Statement of Authorship.....	xx
Acknowledgements.....	xxi
1. Introduction.....	1
1.1 Overview of the Global Positioning System (GPS).....	1
1.2 GPS Meteorology and Research Background.....	4
1.2.1 The Concept of GPS Meteorology.....	4
1.2.2 Water Vapour Observing Systems.....	6
1.2.3 Current Research and Development Status.....	10
1.3 The Objectives and Main Contributions of the Study.....	14
1.3.1 Major Research Objectives.....	14
1.3.2 Contributions and Benefits of the Research.....	16
1.3.3 The Scope and Limitation of the Research.....	16
1.4 Organization of the Thesis.....	17
2. Principles Water Vapour Estimation: Concepts, Models and Estimations....	19
2.1 The Atmosphere Delay.....	19
2.1.1 Ionospheric Delay.....	19
2.1.2 Tropospheric Delay.....	21
2.2 Modelling of Troposphere Delay.....	22
2.2.1 Tropospheric Delay Models Based on Atmospheric Refractivity Profiles	22
2.2.2 Empirical Models of Zenith Tropospheric Delay.....	25
2.2.2.1 Zenith Hydrostatic Delay Models.....	25
2.2.2.2 Zenith Wet Delay Models.....	28
2.2.3 Conversion of Wet Delays into Precipitable Water Vapour.....	29

2.3 Mapping Functions.....	31
2.3.1 Marini Mapping Function.....	32
2.3.2 Chao Mapping Function.....	33
2.3.3 Davis Mapping Function.....	33
2.3.4 Herring Mapping Function.....	34
2.3.5 Niell Mapping Function (NMF).....	35
2.3.6 Comparison of Mapping Function.....	37
2.4 Mean Weighted Temperature of the Atmosphere.....	37
2.4.1 Linear Regression Method.....	38
2.4.2 Extended Linear Regression Method.....	39
2.4.3 The Meteorology Models.....	40
2.5 Estimation of Precipitable Water Vapour from Radiosonde Data.....	41
3 Estimating Atmospheric Water Vapour from GPS Observations.....	43
3.1 GPS Observations.....	43
3.2 Modelling Tropospheric Delays in GPS Data Processing.....	46
3.3 Least Squares Parameters Estimation.....	48
3.4 GPS Data Processing Scheme and Software.....	49
3.4.1 GPS Data Processing Scheme.....	49
3.4.2 GPS Data Processing Software.....	50
3.5 Experimental Studies.....	51
3.5.1 Experimental Description.....	51
3.5.2 Daily GPS Data Processing.....	53
3.5.3 Computing PWV from GPS ZTD and Surface Meteorological Data.....	53
3.5.4 Experimental Results and Discussion.....	56
3.5.5 Improving the Agreement.....	61
3.5.6 Summary.....	63
4. GPS Water Vapour Estimation Using Interpolated Surface Meteorological Data from Australian Automatic Weather Stations.....	65
4.1 Introduction.....	65
4.2 Accuracy Requirements for Surface Meteorological Data.....	66
4.2.1 Influence of the Pressure Error.....	67
4.2.2 Influence of the Temperature Error.....	68

4.3 Description of Surface Meteorological Data and Interpolation Procedures....	69
4.3.1 Data Conversion between a Reference Level and Station Level.....	70
4.3.2 Interpolation Methods.....	71
4.4 Interpolation Results With a Local AWS Network.....	73
4.5. GPS Water Vapour Experiments and Results.....	74
4.5.1 Experimental Description.....	74
4.5.2 Experimental Results and Discussion.....	75
4.6. Summary.....	77
 5. Measuring Ocean Loading and Its Effects on GPS Derived Precipitable Water Vapour.....	78
5.1 Introduction.....	78
5.2 Ocean Loading Models and Effects on Australian ARGN Sites.....	78
5.3 GPS Measurements and Data Analysis.....	84
5.4 Impact of Ocean Loading on ZTD Estimates.....	85
5.5 Impact of Ocean Loading on PWV Estimates.....	89
5.6 Conclusion.....	91
 6. GPS Sensing of Slant Water Vapour.....	93
6.1 Definition.....	93
6.2 Data Processing Techniques for SWV Estimation.....	95
6.3 Obtaining One-way Phase Residuals from Double-Differenced Residuals....	96
6.4 Construction of Stacking Multipath Map.....	99
6.5 Experiment Description and Analysis.....	100
6.6 A Perspective for Applications of GPS Sensed SWV.....	106
 7. Near-Real-Time GPS Water Vapour Estimation.....	108
7.1 Requirements from Meteorological Community.....	108
7.2 Near-Real-Time Data Processing.....	109
7.2.1 Definition.....	109
7.2.2 Differences between Near-Real-Time and Post Data Processing.....	110
7.3 The Impact of Orbits on NRT Water Vapour Estimates.....	111
7.3.1 Availability of GPS Orbits.....	111
7.3.2 Comparison of Orbits for Near-Real-Time Water Vapour Estimation. .	112

7.3.3 Reducing Effects of Orbital Errors on NRT Water Vapour Estimates...	115
7.4 Data Processing Techniques.....	117
7.5. Conclusion.....	120
8. Conclusions and Recommendations.....	121
References.....	123
Appendices.....	139
Appendix A Useful Meteorological Constants and Equalities.....	139
Appendix B ITRF 2000 Coordinates for ARGN Stations.....	140
Appendix C Ocean Loading Tide Coefficients for ARGN Stations.....	141

List of Figures

Figure 1.1 Space-based GPS Meteorology: GPS Occultation Geometry.....	5
Figure 1.2 Some existing techniques for measuring atmospheric water vapour.....	7
Figure 1.3 Illustration of GPS zenith delay geometry (left) and slant-path delay geometry (right).....	12
Figure 1.4 Operational IGS hourly sites in the Australian region (left) and the Land Victoria GPS network (right).....	14
Figure 2.1 Layers of the Earth's Atmosphere. Note that the thermosphere ranges to height of 500km or so and the ionosphere to more than 1,000km.....	20
Figure 2.2 Comparison of empirical ZHD models with the radiosonde derived ZHD.....	27
Figure 2.3 Comparison of empirical ZWD models with the radiosonde derived ZWD.....	29
Figure 2.4 The ratio Π =PWV/ZWD as a function of the mean weighted temperature T_m	31
Figure 2.5 Weighted mean temperature T_m as function of surface temperature T_s . The read solid line is the regression line for the whole data set.....	39
Figure 3.1 GPS data processing scheme.....	50
Figure 3.2 Australian Regional GPS Network (ARGN).....	52
Figure 3.3 Locations of Some Australian Upper Air Network (AUAN) stations.....	53
Figure 3.4 Reduction of T_{rad} and P_{QNH} to T_{GPS} and P_{GPS} , which is highly sensitive to the height difference between GPS and radiosonde sites.....	55
Figure 3.5 RMS of GPS-PWV estimates for 24 hours.....	57
Figure 3.6 The differences of GPS-PWV estimates at UTC 0h for five ARGN stations.....	57
Figure 3.7 Comparison of GPS-PWV estimates (blue solid line) and Rad-PWV estimates (red dot) and their differences (green dot) for a 3-month period at the five ARGN sites: ALIC, COCO, DARW, HOB2 and TOW2.....	59
Figure 3.8 A scatter-plot for all the five sites comparing GPS-PWV solutions against the radiosonde PWV estimates.....	60
Figure 3.9 T_m estimates (upper) and their difference from radiosonde data and linear regression models.....	62
Figure 4.1 Distribution of about 400 hourly updated automatic weather stations (AWS) all over Australia (left), including about 60 sites in Victoria (right).....	70
Figure 4.2 Different variograms for the Ordinary Kriging method. The maximum range a is set to 1000km (left) and 1500km (right) respectively.....	72
Figure 4.3 The network of 36 hourly updated AWS sites, covering the area between 33°S and 38°S and between 140°E and 150°E in Australia. Asterisks indicate outlying points.....	73
Figure 4.4 Interpolated pressures standard deviation (STD) and mean values over the 33 data points against time, excluding three outlying data points.	74
Figure 4.5 GPS-PWV estimates against Rad-PWV estimates at Alice Springs, Darwin, Hobart and	

Townsville stations.....	76
Figure 4.6 A scatter-plot for all four sites comparing GPS-PWV solutions against the radiosonde estimates, with interpolated T and P.....	76
Figure 5.1 Vertical displacements on June 1 2000 at ARGN site COCO.....	81
Figure 5.2a Ocean loading displacements on June 1 2000 at ARGN site ALIC.....	82
Figure 5.2b Ocean loading displacements on June 1 2000 at ARGN site COCO.....	82
Figure 5.3 Ocean loading displacement time series at ARGN site COCO.....	83
Figure 5.4 Vertical displacement time series over 3 days derived from GPS measurements versus ocean loading predictions at ARGN site COCO.....	85
Figure 5.5a Time series of the ZTD differences for the ARGN site COCO, between the solution with ocean loading corrections and the solution without ocean loading corrections.....	86
Figure 5.5b Time series of the modelled vertical position variations due to ocean loading at ARGN site COCO.....	87
Figure 5.6 Illustration of ZTD difference between a solution with ocean loading correction and a solution without ocean loading correction, as a function of the vertical component of the predicted site position computed using the CSR4.0 ocean tide model.....	87
Figure 5.7 Time series of ZTD difference and the vertical displacement predicted using the CSR4.0 ocean tide model. The ZTD difference was multiplied by 3.9 in order to match the vertical displacement.....	88
Figure 5.8 Power spectrum of the ZTD difference time series at ARGN site COCO, based on 1 month of continuous data sampled at 30 min intervals.....	89
Figure 5.9 PWV differences between GPS-PWV estimates and radiosonde PWV estimates from day of year 180 to 280 in 2000 at ARGN station COCO.....	90
Figure 6.1 GPS sensed SWV along each ray path from GPS satellite to receiver.....	94
Figure 6.2 Day-to-day repeatability of LC one-way residuals. Curves show one-way errors for ARGN site ALIC, satellite PRN 01, for three days. The data from day 161 have been offset in amplitude by +60 mm and in time by 8 min; data from day 162 have been offset in amplitude by 0 mm and in time by 4 min; and data from day 163 have been offset in amplitude by -60 mm and in time by 0 min.....	102
Figure 6.3 Day-to-day repeatability of LC one-way residuals. Curves show one-way errors for ARGN site DARW, satellite PRN 01, for three days. The data from day 161 have been offset in amplitude by +60 mm and in time by 8 min; data from day 162 have been offset in amplitude by 0 mm and in time by 4 min; and data from day 163 have been offset in amplitude by -60 mm and in time by 0 min.....	102
Figure 6.4 Slant path delay (SPD) residuals with respect to satellite elevation and azimuthal angles (“sky plot”) at ARGN site ALIC (left) and DARW (right) on day of year 161, 2000. The upper panel is the original postfit SPD residuals and the middle panel is the multipath constructed from 10 days SPD residuals. The lower panel is the corrected SPD residuals obtained by subtracting the multipath map from the observed SPD residuals.....	103
Figure 6.5 Illustration of dependency of the LC post-fit residuals on the elevation angle and azimuth	

at ARGN site ALIC on day 161,.....	104
Figure 6.6 Slant water vapour time series at ARGN site ALIC.....	106
Figure 6.7 Slant water vapour time series at ARGN site DARW.....	106
Figure 7.1 RMS of ZTD differences between the solutions using different IGS and JPL orbits.....	113
Figure 7.2 Mean difference of ZTD estimates between the solutions using different IGS and JPL orbits.....	114
Figure 7.3 Comparison of IGS rapid, ultra rapid orbits and JPL 15 minute orbits with respect to IGS final orbit. For the IGS ultra rapid orbit, only the predicted portions (the parts from 3-15 and from 15-3 UTC) were used.....	114
Figure 7.4 Comparison of IGS rapid, ultra rapid orbits and JPL 15 minute orbits with respect to IGS final orbit on day of year 41, 2004.....	115
Figure 7.5 RMS of ZTD difference between the results from different orbits using the iterative satellite rejection method.....	117
Figure 7.6 Mean difference between ZTD estimates from different orbits using the iterative satellite rejection method.....	117
Figure 7.7 RMS difference versus processing time.....	119

List of Tables

Table 2.1 Comparison of empirical ZHD models with the radiosonde derived ZHD.....	27
Table 2.2 Comparison of empirical ZWD models with the radiosonde derived ZWD.....	29
Table 2.3 Coefficients of the Niell hydrostatic mapping function (average values).....	36
Table 2.4 Seasonal variations/amplitudes of the Niell hydrostatic mapping function.....	36
Table 2.5 Coefficients of the Niell hydrostatic mapping function (height correction).....	36
Table 2.6 Coefficients of the Niell wet mapping function. This table contains average values in dependency of latitude. Seasonal variations are not modeled for the wet component.....	36
Table 2.7 Conversion coefficients for the mixed mean temperature model for ARGN sites.....	40
Table 3.1 Linear Combinations of the L_1 and L_2 observations.....	46
Table 3.2 The main characteristics of GPS data processing.....	54
Table 3.3 Separation between ARGN GPS sites and AUAN Radiosonde sites.....	54
Table 3.4 Average number of radiosonde samples.....	58
Table 3.5 Comparison of GPS PWV estimate with radiosonde PWV estimates during a 3-month period at five ARGN sites: ALIC, COCO, DARW, HOB2 and TOW2.....	60
Table 3.6 Average PWV estimate errors as a function of T_m errors of 3K and 5K for the five stations...	62
Table 3.7 Comparison of GPS PWV estimates with radiosonde PWV estimates during a 3-month period, where one estimate uses T_m from Linear Regression Model and the other uses T_m from Radiosonde data. A total of 566 comparisons are included in the mean, standard deviation, root mean squares (mm).....	63
Table 4.1 Influence of the pressure error on PWV estimation.....	68
Table 4.2 Summary of interpolated pressure errors and predicted ZHD and PWV errors.....	74
Table 4.3 Overall consistency of GPS PWV with interpolated T and P and Radiosonde PWV.....	77
Table 5.1 Differences between the ocean tide models.....	81
Table 5.2 Comparison of GPS PWV estimates with radiosonde PWV estimates during a 3-month period. (ocean loading correction not applied).....	90
Table 5.3 Comparison of GPS PWV estimates with radiosonde PWV estimates during a 3-month period. (ocean loading correction applied).....	91
Table 6.1a RMS of LC post-fit residual before and after multipath correction for ALIC.....	105
Table 6.1b RMS of LC post-fit residual before and after multipath correction for COCO.....	105
Table 6.1c RMS of LC post-fit residual before and after multipath correction for DARW.....	105
Table 6.1d RMS of LC post-fit residual before and after multipath correction for HOB2.....	105
Table 6.1e RMS of LC post-fit residual before and after multipath correction for TOW2.....	105
Table 7.1 Generic requirements for operational meteorology.....	108
Table 7.2 Generic requirements for climate monitoring and prediction.....	109

Table 7.3 Differences between near-real-time and post data processing.....	111
Table 7.4 GPS satellite orbits available from IGS.....	112
Table 7.5 Comparison of ZTD estimates using different orbit products. The ZTD estimates obtained using the IGS Final orbits were used as reference to compare the other results with. All ZTD estimates at 30min interval from 15 ARGN stations over 2 weeks were included (there are only 13-day predicted orbits available for processing)	113
Table 7.6 Comparison of computing burden and accuracy of ZTD estimates for different session lengths.....	119

List of Symbols

The symbols used in this work are listed in the following. Note that certain symbols may have several meanings depending on the particular context. In many cases, the symbols are explained separately under each formula where they appear.

α	elevation cut-off angle
α	mapping function coefficients
$\alpha(\varphi)_{average}$	mean value
$\alpha(\varphi)_{amplitude}$	amplitude of seasonal variations
β	temperature lapse rate
γ_{ij}	variogram
Δclk	combined receiver and satellite clock corrections
ΔH	height difference
Δhw	hardware biases of the receiver and the transmitter
Δion	ionospheric delay
ΔL	total tropospheric delay
ΔL^0	total tropospheric delay in the zenith direction
ΔL_h^0	zenith hydrostatic delay (ZHD)
ΔL_w^0	zenith wet delay (ZWD)
$\Delta orien$	receiver/transmitter antenna orientation correction
Δpcv	antenna phase centre variation correction
Δrel	relativistic effects
Δsyn	synchronization error
$\Delta trop$	tropospheric delay
δX	vector of corrections
ε	elevation angle
θ	angular distance
κ	constant
λ	longitude
λ	wavelength of the carrier signal

$\Pi(T_m)$	dimensionless conversion factor
ρ	total mass density of the air
ρ	density of liquid water
ρ_i	mass density
σ_{12}	standard deviation of the combined phase observation
$\sigma_{L_1}, \sigma_{L_2}$	systematic errors on L_1 and L_2 observation
$\sigma_{L_{12}}$	systematic error on the combined observation
σ_{PWV}	error in PWV
σ_P	uncertainty on the pressure measurements
σ_d	uncertainty on the calculated ZHD
σ_T	uncertainty on the temperature measurements
Φ_{IF}	ionosphere-free carrier phase
Φ_{L1}	phase of the primary carrier ($L1$)
Φ_{L2}	phase of the secondary carrier ($L2$)
φ	latitude
φ, λ	spherical coordinates of the loading point
φ', λ'	spherical coordinates of the estimation point
w_{AB}^i	satellite-dependent weighting for the site pair AB and satellite i
w_I^i	weighting for the i'th satellite at the I'th site
A	design matrix
A	azimuthal angle
a	maximum range
a, b, c, \dots	profile dependent coefficients
$C_{\hat{x}}$	covariance matrix
DD_{AB}^{12}	double difference
DOY	day of year
DOY_w	day of year for "maximum winter"
ds	ray path
dt	clock

e	partial water vapour pressure
e	residual errors
f_1	frequency of the primary carrier (L1)
f_2	the frequency of the secondary carrier (L2)
G	geometrical straight-line path length
$G(\theta, A)$	mass-loading Green's function
G_{rad}	Green's functions in radial direction
G_{hor}	Green's functions in horizontal direction
H	height above the ellipsoid
H	ocean tidal height
H_0	height of site above sea level
H_{stn}	Station height
H_T	tropopause height
h	height of upper edge troposphere
h'_n, l'_n	loading Love numbers of order n
k_1, k_2, k_3, k_4	refraction coefficients
k'_2	weighted mean value for the derived constant
L	curved ray path
$L(\phi', \lambda')$	ocean load tide
L_1	L_1 phase measurement
L_2	L_2 phase measurement
L_{12}	combined phase measurement
L_A^1, L_A^2	observations of satellite 1 and 2 by receiver A
L_B^1, L_B^2	observations of satellite 1 and 2 by receiver B
L_C	ionosphere-free combination
L_G	geometry-free combination
L_N	narrow lane combination
L_W	wide lane combination
M_e	mass of the Earth

$M_h(\epsilon)$	hydrostatic mapping function
$M_w(\epsilon)$	wet mapping function
N	ambiguity
N	atmospheric refractivity
N_d	dry refractivity
N_h	hydrostatic refractivity
N_w	wet refractivity
$n(s)$	index of refraction
P_{MSL}^0	standard pressure at mean sea level
P_{MSL}	pressure at mean sea level
P_{QFE}	QFE pressure
P_{QNH}	QNH pressure
P_c	partial pressures of carbon dioxide
P_d	partial pressures of the dry gases
P_i	partial pressure of an atmospheric constituent
P_n	Legendre function of degree n
P_s	surface pressure at the station
P_v	partial pressures of water vapour
P_x	apriori weighted constraints
R	geometrical distance from satellite to receiver
R	radius of the Earth
RH_s	relative humidity at station level
R_i	specific gas constant
R_v	specific gas constant for water vapour
RH	relative humidity
S	curved path length
SD_{AB}^1, SD_{AB}^2	single differences
S_i	non-isotropic component of the slant water
T	absolute temperature

T_m	mean weighted temperature of the atmosphere
T_s	surface temperature in Kelvin
t	temperature
t_0	surface temperature in °C
V	vector of residuals
W	misclosure vector
X	unknown parameters
X_0	apriori parameters and observations
\hat{X}	estimated parameters
x, y, z	station position
Z_d^{-1}	inverse compressibility factors for dry air
Z_v^{-1}	inverse compressibility factors for water vapour

List of Acronyms

A/S	anti-spoofing
ARGN	Australian Regional GPS Network
AUAN	Australian Upper Air Network
AUSLIG	Australian Surveying and Land Information Group
AWS	Automatic Weather Stations
BOM	Bureau of Meteorology
C/A	coarse/acquisition code
C/N	signal-to-noise ratio
COST	an intergovernmental framework for European Cooperation in the field of Scientific and Technical Research
CRCSS	Cooperative Research Centre for Satellite Systems, Australia
EC	European Community
DOY	day of year (range: 1 ... 365/366; start: 1 = January, 1st)
DOW	day of week (range: 0 ... 6, start: 0 = Sunday)
ECEF	Earth-centred earth-fixed coordinate system
EOP	Earth orientation parameters
FSL	Forecasting System Laboratory, NOAA, USA
GASP	GPS Atmosphere Sounding Project, German
GDAS	Global Data Assimilation System
GEONET	GPS Earth Observing Network, Japan
GFZ	GeoForschungsZentrum Potsdam, Germany
GPS	Global Positioning System
GNSS	Global Navigation Satellite Systems
GPSnet	GPS base station network of Land Victoria, Australia
IERS	International Earth Rotation Service
IGP	IGS predicted orbits, predicted for 24 up to 48 hours
IGR	IGS rapid orbits, delivered with a latency of 2 days
IGS	International GPS Service
IGS	IGS final orbits, delivered with a latency of 2 weeks
IGU	IGS ultra-rapid orbits
InSAR	Interferometric Synthetic Aperture Radar

ITRF	International Terrestrial Reference Frame
IWV	integrated water vapour
JPL	Jet Propulsion Laboratory
LEO	low-earth orbiter, satellite with small orbit altitude (500-1000 km)
LIDAR	light detection and ranging
LOS	line of sight
MCS	Master Control Station
MEO	medium-earth orbiter, satellite with medium orbit altitude (>20,000km)
MIT	Massachusetts Institute of Technology
NASA	National Aeronautics and Space Administration, USA
NCEP	National Centres for Environmental Prediction, USA
NGS	National Geodetic Survey, USA
NOAA	National Oceanic and Atmospheric Administration, USA
NRT	near-real-time
NWP	numerical weather prediction
NWM	numerical weather model
PCV	phase centre variation, filename suffix of antenna calibration tables
PRN	pseudo-random noise
PW	Precipitable water
PWV	Precipitable Water Vapour; alternative term for PW used by some authors
RH	Relative Humidity
RINEX	receiver-independent exchange format
RMS	root mean square
S/A	selective availability
SIO	Scripps Institution of Oceanography
SPD	slant-path delay
SHD	slant hydrostatic delay
SWD	slant wet delay
SWV	slant-path wet vapour
TEC	total electron content
VLBI	very long baseline interferometry
USAF	the United States Air Force
WMO	World Meteorology Organisation

WVR	water vapour radiometer
ZHD	zenith hydrostatic delay
ZTD	zenith total delay or zenith tropospheric delay
ZWD	zenith wet delay

Statement of Authorship

The work contained in this thesis has not been previously submitted for a degree or diploma at this or any other higher education institution. To the best of my knowledge and belief, the thesis contains no material previously published or written by another person except where due reference is made.

Signature: _____

Date: _____

Acknowledgements

First of all I would like to thank my supervisor, Dr. Yanming Feng, for directing me towards this research topic and providing me with excellent advice and guidance. Moreover, he has consistently helped me to stay motivated, especially in the darkest days when the deadline loomed.

I thank my associate supervisor, Prof. Miles Moody, for his support and guidance; Philip Webster, Anthony Rasmussen and Dan Moradian for computing resources; Scott Johnson and Dee Groves for administrative support; Yi Zheng and Ning Zhou for their discussions and friendship. Thanks go to everybody else at CRCSS I didn't mentioned. I am fortunate to have had access to such an excellent facility and staff.

Special thanks go to Dr. Peng Fang and Dr Maorong Ge for their help on GAMIT data processing; Mr. Lennard Husiman for testing the interpolation methods during his internship; Mr. David Brandt and Barry Gordon for the explanation of some meteorological subjects.

Special thanks also go to the Australian Government and the CRC for Satellites Systems, QUT for the scholarship and financial assistance; the Australian Surveying and Land Information Group, Bureau of Meteorology and Land Victoria for providing GPS tracking data and meteorological/radiosonde data in this work.

Finally, I want to thank my parents and family, for raising me to believe that I could achieve anything I set my mind to, for encouraging me to take the more challenging path, and for their unwavering support during my study and my life so far.

Chapter 1

Introduction

As an introduction of the thesis, this chapter will start with an overview of the Global Positioning System (GPS); outline its current status, future modernization and major applications. Next, we turn to review GPS meteorology, its concepts, benefits for weather forecasting and climate modelling, and major research problems and research directions. In the third section, the objectives of the thesis are presented, followed by an outline of the structure of the thesis.

1.1 Overview of the Global Positioning System (GPS)

The NAVSTAR Global Positioning System (GPS) has been developed by the Department of Defence of the United States. The main purpose is to provide the military forces of the USA and its allies with a means to accurately determine their position, velocity and time, anywhere on the Earth, at any time. The GPS system consists of three major segments: SPACE, CONTROL and USER. The SPACE segment currently consists of 28 operational satellites in six orbital planes with four satellites in each plane spacing evenly and several spare satellites. The satellites operate in circular orbits of approximately 20,200 km radius at an inclination angle of 55 degrees, with about a 12-hour period. The satellite positions in the sky are the same at the same sidereal time each day, i.e. the satellites appear 4 minutes earlier each day in civilian time. The CONTROL segment consists of five Monitor Stations (Hawaii, Kwajalein, Ascension Island, Diego Garcia, Colorado Springs), three Ground Antennas (Ascension Island, Diego Garcia, Kwajalein), and a Master Control Station (MCS) located at Schriever AFB in Colorado. The monitor stations track all satellites in view, accumulating ranging data. This information is processed at the MCS to determine satellite orbits, clock errors and to update each satellite's navigation message. Updated information is transmitted to each satellite via the Ground Antennas. The USER segment consists of antennas and receiver-processors that provide positioning, velocity, and precise timing to the user.

The satellites transmit on two L-band frequencies: $L1 = 1575.42$ MHz and $L2 = 1227.6$ MHz. Three pseudo-random noise (PRN) ranging codes are in use:

- The coarse/acquisition (C/A) code has a 1.023 MHz chip rate, a period of 1 millisecond (ms) and is used primarily to acquire the P-code;
- The precision (P) code has a 10.23 MHz chip rate, a period of 7 days and is the principle military navigation ranging code;
- The Y-code is used in place of the P-code whenever the anti-spoofing (A/S) mode of operation is activated.

The C/A code is available on the L1 frequency and the P(Y)-code is available on both L1 and L2. All the satellites transmit on the same frequencies, L1 and L2, but with different PRN code assignments. Due to the spread spectrum characteristic of the signals, the system provides a large margin of resistance to interference. Each satellite transmits a navigation message containing its orbital elements, clock behaviour, system time and status messages. In addition, an almanac is also provided which gives the approximate orbit data for each active satellite. This assists the user receiver to find other visible satellites once the first one has been acquired.

Although GPS was originally developed largely for military applications, it has provided significant benefits to a wide variety of civil applications due to its flexibility and worldwide applicability. As a direct result of these benefits to the civil community, U.S. Vice President Al Gore announced a GPS modernization effort in January 1999 to extend the capabilities of GPS even further than those currently enabled by the existing GPS constellation [Gore, 1999].

One of the main components of this modernization program is that two new navigation signals will be available for civil use. These signals will be in addition to the existing civilian service broadcast at 1575.42 MHz (L1). The first of these new signals will be an open civil code located at 1227.60 MHz (L2), and will be available for general use in non-safety critical applications. The other signal, located at 1176.45 MHz (L5), will be available on GPS Block IIF satellites scheduled for launch beginning in 2005. This new L5 signal falls in a band which is protected worldwide for aeronautical radio navigation, and therefore will be

used for safety-of-life applications. Additionally, it will not cause any interference to existing systems. Therefore, with no modification of existing systems, the addition of L5 will make GPS a more robust radio navigation service for many aviation applications, as well as assist all ground-based users (maritime, railways, surface, shipping, etc.). At the current GPS satellite replenishment rate, all three civil signals (L1-C/A, L2-C/A, and L5) will be available for initial operational capability by 2010 and for full operational capability by approximately 2013.

L5 will provide more benefits above and beyond the capabilities of the current GPS constellation, even after the planned second civil frequency (L2) becomes available, including precise navigation worldwide, increased availability of precision navigation operations in certain areas of the world, and interference mitigation [MacDonald, 2002].

In the United States, GPS is regarded as the fifth utility, alongside water, electricity, gas, and telephone. US military and civilian users have developed a considerable dependence on the system. In Europe, the EC White Paper on European Transport Policy for 2010 identifies Global Navigation Satellite Systems (GNSS) as a critical technology that could revolutionize European transport infrastructure. Having identified the fast growing dependence on GPS and its significant implications on social, economic, technological, political and commercial aspects, Europe is now developing their own GNSS, known as Galileo, which is independent of and interoperable with the U.S. Global Positioning System.

Applications of GPS technologies have been identified and developed over the past 20 years in many different domains, such as industry, military, transportation, science, and personal mobility and recreation, sports, etc. In the agricultural industry, real-time positioning techniques are used in precision farming, crop dusting aircraft navigation, farming vehicle automation, and so on. In the geospatial industry, GPS is widely used for control surveying, engineering setting out, mapping and GIS data acquisition, etc. In the domain of public safety, fire, police, ambulance, search and rescue services have used GPS location information for their operations. In telecommunications, GPS timing solutions are used for

digital network timing & synchronization, site acquisition, site surveying, cellular & PCS drive test & system acceptance, and microwave path surveying. In space engineering, the applications include spacecraft navigation, precise satellite orbit determination and ground-based autonomous orbit tracking. In military, GPS is applied in intelligence and target location, command & control, search & rescue, mine laying & detection, and weapon aiming and guidance, and many more.

The scientific applications of GPS technologies are also found in many fields: archaeology, atmospheric science, environmental science, geodesy, geology & geophysics, oceanography, wildlife, space sciences, etc. This research will focus on one of the significant scientific applications - Ground-based GPS Meteorology, addressing challenges in using GPS data for meteorological applications in Australia. In the following sections, we will give a general overview for the concepts of GPS meteorology and their current research and development status, and identify the research problems to be addressed in this thesis.

1.2 GPS Meteorology and Research Background

1.2.1 The Concept of GPS Meteorology

The term ‘GPS meteorology’ was coined in 1992 [Bevis, Anthes *et al.*, 1992], and is rapidly gaining acceptance in meteorological sciences. The term refers to *remote sensing of the troposphere and the stratosphere by gauging the refraction (slowing and bending) of GPS signals that propagate through the atmosphere*. The fundamental physical basis for GPS meteorology is the pressure, temperature and humidity dependence of microwave refractivity in the neutral atmosphere. Depending on the location of GPS receivers, there are two main categories of GPS meteorology [Berbeneva *et al.*, 2001]:

- **Ground-based GPS meteorology.** Delays accumulated in the neutral atmosphere by signals propagating from GPS satellites to ground-based geodetic GPS receivers are estimated during standard geodetic analyses of network observations. These delays are very sensitive to the total quantity of water vapour integrated along the signal path. Emerging networks of continuously operating geodetic GPS receivers can be used to estimate

integrated water vapour (IWV) or precipitable water vapour (PWV)¹ at each station with a temporal resolution of seconds to 30 minutes, and in addition, to estimate the lateral gradients. Nearly all the existing GPS networks are so sparse that they can be used only to characterise IWV/PWV at each station. However, very dense arrays of GPS receivers, with inter-station spacing of a few to tens of kilometres, together with slant water vapour estimation techniques, could be used to characterise water vapour distribution in all three spatial dimensions, as well as in time.

- **Space-based GPS meteorology.** GPS receivers aboard low-earth orbit (LEO) satellites collect signals transmitted from GPS satellites during brief atmospheric occultation events [Kursinski, Schofield *et al.*, 1995]. As shown in Figure 1.1, the bending and slowing of GPS signal observed during the one minute or so that the sub-horizontal transmitter–receiver signal path sweeps vertically through the atmosphere (‘active limb sounding’) can be inverted to provide a vertical refractivity profile [Yan, Huang *et al.*, 1999]. Roughly speaking, these profiles constrain temperature distribution within the stratosphere and water vapour distribution with the troposphere.

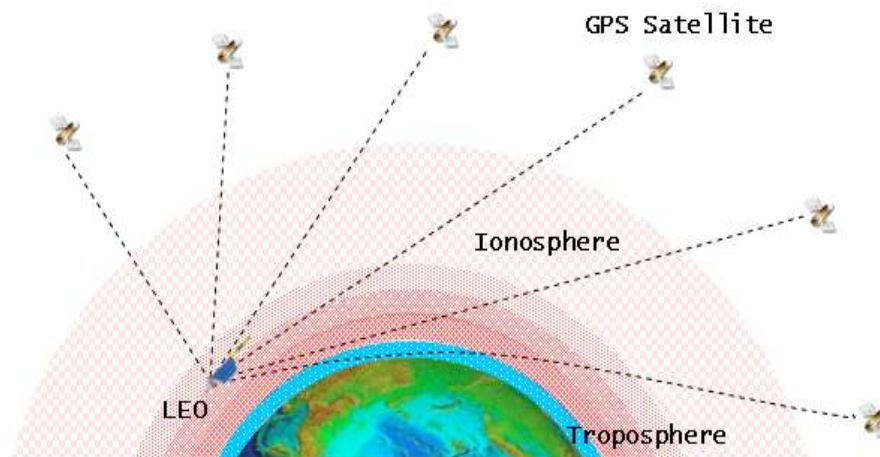


Figure 1.1 Space-based GPS Meteorology: GPS Occultation Geometry.

The space- and ground-based approaches are complementary, rather than competing, in that:

¹ Precipitable water vapour (PWV) is also referred to as precipitable water (PW) by some authors.

- Most ground-based measurements will involve vertical integration or averaging of atmospheric properties, while the space-based approach involves significant lateral averaging. Ground-based networks will be able to estimate lateral gradients in integrated water vapour at each station while a single occultation event provides no significant information on lateral variability.
- Ground-base meteorology provides continuous measurements at a network of fixed stations, while the space-based approach does not. Continuity in both space and time will be advantageous in contexts such as severe weather monitoring near major population centres and airports.
- Because of the sub-horizontal nature of its sampling geometry, space-based measurements are subject to obstruction by mountain ranges, and in adjacent low lying areas, this may render much of the lower troposphere invisible.
- Ground-based meteorology will never achieve good coverage over the oceans, while the space-based approach is essentially global.

The ground-based approach is likely to be mature more rapidly in that it can exploit the explosive growth in continuous GPS networks already underway, and can achieve its goals at little incremental cost. The space-based approach, in order to reach its full potential, requires the existence of tens of suitable GPS receivers in LEO satellites. Both the development and the maintenance costs of the space-based approach will exceed those associated with the ground-based approach. In this study, we focus on the topic of ground-based GPS Meteorology.

1.2.2 Water Vapour Observing Systems

Estimates of atmospheric water vapour are of vital importance to meteorological and climatological modelling, contributing to the understanding of a wide variety of processes from small-scale weather systems to global climate change. Water vapour, a highly variable and important part of the atmosphere, influences meteorological processes, particularly having a significant impact on mesoscale systems such as convective storms and the development of weather fronts. The transport of water vapour through the atmosphere has significant implications for

atmospheric energy transfer, since it has the ability to absorb energy from one location, hold it internally as latent heat, and then release it in an entirely different location. As a whole, water vapour is one of the least well-observed atmospheric parameters, which in turn, causes it to be one of the least well-forecast primary parameters within meteorological prediction models [Cucurull, Rius *et al.*, 2000]. In terms of climatology, water vapour is the main greenhouse gas, and thus any long-term change in water vapour concentration within the atmosphere needs to be precisely accounted for within climate models.

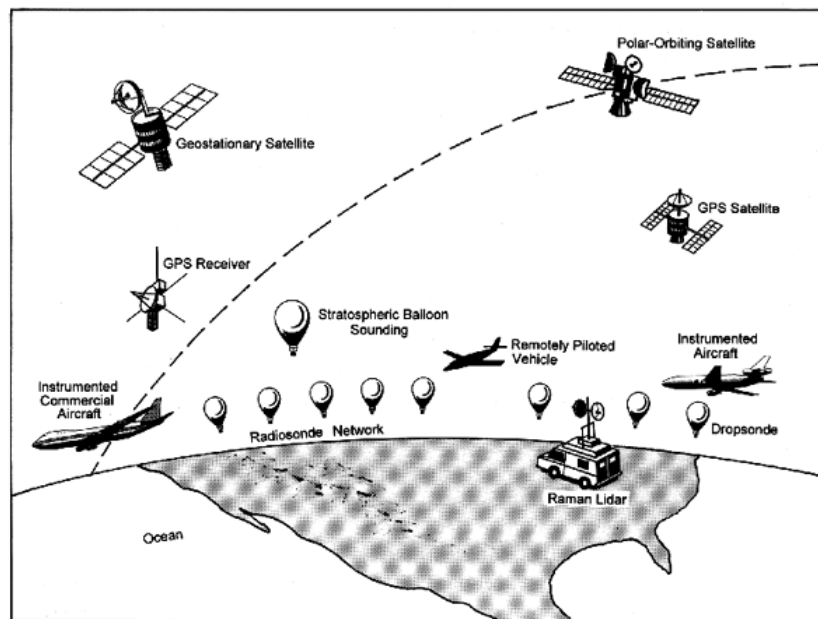


Figure 1.2 Some existing techniques for measuring atmospheric water vapour [Carter, 1997].

Figure 1.2 illustrates some existing techniques for measuring atmospheric water vapour from the ground, air and space, of which the radiosonde-network has become the cornerstone upper air observing systems for many countries. Radiosondes are balloon-borne instruments, which measure temperature, pressure and humidity through a profile of the Earth's atmosphere up to the height of approximately 30km, and transmit the observed data to a ground station. The cost of launching the radiosondes however, is relatively high and only 80% of them are reused. The high cost limits the frequency of launches and also the spatial distribution of the sites. In general, in most countries radiosondes are released every 12 or 24 hours. A further physical limitation of the radiosonde is the accuracy of the humidity sensor, which has a root mean square (RMS) uncertainty

of 5 –10% at high altitudes and ceases to operate at temperatures below 40°C. Additional inaccuracy can be caused by condensation of liquid water on the humidity sensor when liquid water content is particularly high [Liu, Chen *et al.*, 2000]. Despite their limitations, however, radiosondes are still one of the major current meteorological measurement systems. There are over 900 radiosonde stations worldwide. In Australia there are currently 52 radiosonde stations including those on islands in the Antarctic region. Through international agreements, radiosonde data are exchanged between countries and are applied to a broad spectrum of efforts.

Ground-based microwave radiometers remotely measure the background radiation emitted by atmospheric constituents [Pacione, Ferretti *et al.*, 2001]. At microwave frequencies the emission depends mainly on the concentration of oxygen and water vapour molecules. A water vapour radiometer (WVR) measures the intensity of the water vapour spectral line centred at 22.235 GHz. WVRs are capable of providing line-of-sight estimates of integrated water vapour (IWV) with very good temporal resolution, although there are again a number of limitations to the technique. The algorithms, which convert the measured sky brightness temperature, are based on radiosonde observations that involve their own inherent limitations. Liquid water can also form a layer on the WVR antenna or mirror that will bias the WVR measurements. In the presence of heavy rainfall, the algorithm breaks down and the estimates are no longer reliable. The WVR is also expensive and not very portable, hence the spatial resolution of the measurements is extremely limited and thus the practicality of using a WVR in a meteorological sense is restricted. WVRs are also found on board satellites, but their use for scanning the land surface is limited due to the complications of the variable background surface heat emissions of the Earth that mask the signal originating from the atmospheric water vapour [Pacione, Sciarretta *et al.*, 2001].

In recent years there has been considerable international interest in the use of ground-based GPS for water vapour estimation through the estimation of the atmospheric propagation delay of the GPS signals. The estimated zenith tropospheric delay (ZTD) from GPS can be divided into the ‘dry’ and ‘wet’ parts. If the pressure is known and hydrostatic equilibrium is assumed, the ‘dry’ part can

be accurately modelled and removed from the estimated total zenith delay. The remaining ‘wet’ part can then be converted to the integrated water vapour (IWV) or precipitable water vapour (PWV) by multiplying by a near constant factor [Bevis, Anthes *et al.*, 1992]. It has been consistently demonstrated that integrated water vapour can be routinely measured by GPS with an accuracy of 1 –2 kg/m² [Rocken and *et al.*, 1993; Dodson and Baker, 1998]. Compared to traditional water vapour observing systems such as radiosondes and water vapour radiometers, ground-based GPS sensing of atmospheric water vapour has the following distinct advantages:

- High temporal resolution: GPS can provide IWV/PWV estimates as accurate as those derived from the commonly used radiosonde instruments, but with a temporal resolution of 30 seconds to 30 minutes (compared with weather balloons which are released every 12 or 24 hours), and with all-weather operability and long-term measurement stability.
- Low cost equipment and maintenance: Geodetic quality GPS receivers are modestly priced (\$15-20K at present), but their operation can be unattended for long periods with high reliability, and with low telemetric data transmission cost. On the other hand, the more expensive radiosondes need regular calibration, and there is an operational cost of \$500 per release for each radiosonde station.
- High spatial resolution possible: In many countries or regions, networks of tens, and even hundreds, of GPS receivers have been (or are being) established by government agencies and private companies to support survey, geodetic and navigation applications. With some additional capital investment such networks can be upgraded for water vapour estimation with unprecedented spatial resolution.

If such a GPS-based water vapour measuring system were implemented, near-term weather forecasting would be possible, which may lead to a reduction in damages due to sudden severe weather conditions. In addition, such data could improve mid-term weather predictability, which is particularly useful for determining the likelihood of the onset of floods, or the converse, severe drought. Furthermore, GPS-sensed tropospheric delay information can be used for image correction, for example of satellite remote sensed SAR images. Long-term climatology would

also benefit from the GPS-derived water vapour time series that would become globally available.

1.2.3 Current Research and Development Status

The potential of GPS sensing of atmospheric water vapour has been demonstrated through many experiments around the world over the past few years. The first proof-of-concept study was the GPS/STORM experiment which took place in the high-tornado risk mid-western region of the United States. This experiment compared GPS water vapour measurements to radiosonde measurements during a time period which included more than 6 major storms, and demonstrated the validity of the method. Since then a number of projects have been conducted to use continuous GPS network to monitor atmospheric water vapour in support of basic meteorological research, climatology and operational weather analysis and prediction. For example, the Forecasting System Laboratory (FSL) of the National Oceanic & Atmospheric Administration (NOAA) has established a GPS Integrated Precipitable Water Demonstration Network of 291 sites in the United States. This project is working in a quasi-operational status and is mainly focused on measuring the impact of GPS PW data on numerical weather modelling and on improving quality control for near-real-time solutions. In Japan, the GPS Meteorology Project seeks to exploit about 1,000 stations from a nation wide permanent GPS array, known as GPS Earth Observation Network (GEONET) operated by the Geographical Survey Institute (GSI), to derive meteorological products to benefit real-time geodesy as well as exploit geodesy for meteorology. The first extensive European trials of GPS Meteorology were mounted through the projects WAVEFRONT, BALTEX and MAGIC funded by the EC. The EC has supported COST Action 716 "Exploitation of Ground-Based GPS for Climate and Numerical Weather Prediction Applications" in 2000, which emphasizes operational exploitation of GPS Meteorology. A German project associated with this cost action, known as the 'GPS Atmosphere Sounding Project (GASP)', is already performing near-real-time GPS PW measurements in an operational mode and more continuous operated GPS stations will be added to the existing network in the near future. This project emphasizes integration of both the ground- and space-based approaches.

Through the outcomes of these projects it has been demonstrated that the amount of precipitable water vapour (PWV) contained in the neutral atmosphere can be estimated using ground-based GPS observations with the same level of accuracy as radiosondes and microwave radiometers [Bevis, Anthes *et al.*, 1992; Rocken *and et al.*, 1993; Emardson, Elgered *et al.*, 1998; Tregoning, Boers *et al.*, 1999]. In addition, ground-based GPS receivers are portable, economic, and can provide continuous PWV estimates with higher temporal resolution than radiosondes, and are unaffected by rain and clouds. GPS could consequently become an important source of PWV observations for numerical weather prediction (NWP) models [Kuo, Zou *et al.*, 1998; Yang, Emardson *et al.*, 1999].

While the GPS-PWV technique has become relatively mature for operational use, there are still some remaining challenges. Currently, researchers have focused their efforts on the following:

Development of GPS-PWV estimation systems is progressing from daily operation towards near-real-time (NRT) operation, leading to regional water vapour observing systems in some countries. Daily estimation strategy results in PWV measurements with time latency of about several hours to some days, depending on the latency of International GPS Services (IGS) post-fit orbit products. This strategy is adequate for research and scientific purposes. However, to take full advantages of the GPS water vapour estimation techniques for NRT meteorological forecasting application, water vapour solutions have to be produced on an hourly or half-hourly basis. One major remaining technical challenge is to ensure the quality and integrity of the GPS orbit solutions available in NRT [Fang *et al.*, 2001]. The other challenges are to maintain efficient data flow and reduce the computational time for orbit determination and PWV estimation to an acceptable level, while as many tracking sites as possible are incorporated into the processing system. *These challenges will be addressed in the thesis.*

*Research in GPS water vapour sensing techniques turns the focus from GPS PWV estimation to slant-path water vapour (SWV) estimation [Braun, *et al.*, 2001].* The

GPS PWV technique is relatively mature and ready for operational use. What remains a challenge is to estimate the line-of-sight PWV from an individual satellite to a receiver, commonly referred to as the 'Slant-path Water Vapour' (SWV), converted from the slant-path delay (SPD) estimates (just as the PWV is converted from ZTD). Recent computer simulations by NOAA FSL scientists indicate that it may be possible to retrieve the vertical distribution of moisture in the atmosphere using 3-dimensional variational analysis techniques [MacDonald *et al*, 2000]. SWV estimation technique is highly desirable and potentially important. However, as shown in Figure 1.3, SWV values are more difficult to measure than PWV. GPS PWV measurements are essentially an average over all SWV measurements taken over a period of time, in the direction of each satellite in view, and scaled to the zenith direction. For a single site recording data at 30 seconds from average 8 satellites, what is generated is a 30-minute PWV estimate, averaged from 480 SWV observations. To directly recover these SWV measurements, the sources of measurement error that are successfully accounted for by measurement modelling of the zenith tropospheric signal delay will have to be dealt with in other ways. *This challenge will also be addressed in the thesis.*

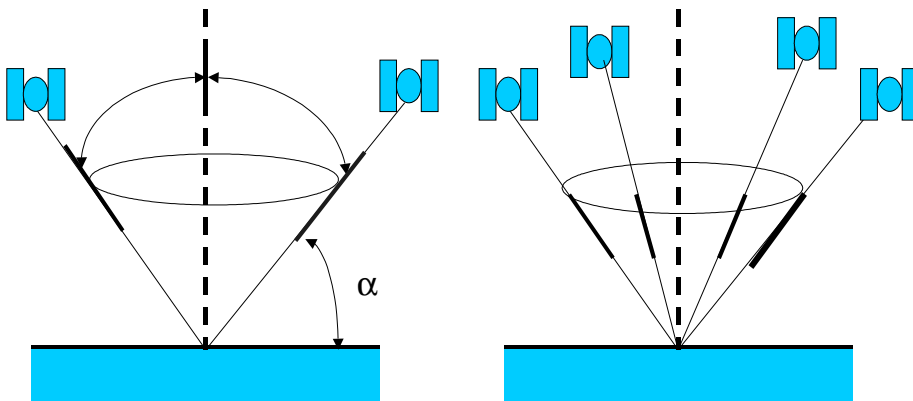


Figure 1.3 Illustration of GPS zenith delay geometry (left) and slant-path delay geometry (right).

*Investigation into GPS water vapour applications is moving from experimental demonstrations and validations of PWV/SWV estimation capability towards assimilation of GPS PWV/SWV measurements into numerical weather prediction (NWP) models or modelling of the vertical distribution of moisture using 3-dimensional variational analysis techniques [Iwabuchi *et al.*, 2000, MaCDonald *et al.*, 2000, Smith *et al.*, 2001]. Other applications, such as GPS-sensed*

tropospheric delay information for Interferometric Synthetic Aperture Radar (InSAR) image corrections and wide area differential GPS corrections are also under investigation [Zheng, Y, 2004]. Such investigations are however beyond the scope of this thesis.

Research on GPS Meteorology in Australia has so far been limited to some experimental studies, including the work on comparison of GPS PWV solutions and microwave water vapour radiometer (WVR) measurements [e.g. Tregoning, 1999] and the author's work at the CRC for Satellite Systems (CRCSS).

To establish a dedicated system like the FSL's GPS meteorological network of several hundreds of stations to cover Australia would initially cost tens of millions of dollars. Fortunately there are a number of permanent GPS networks operating on a continuous basis, recording GPS raw measurements every hour, which allow Australian scientists to carry out GPS water vapour sensing research such as described in this thesis without the initial infrastructure spending. Examples of the networks are:

- As illustrated in Figure 1.4, there are fourteen IGS stations around Australia operated by Geoscience Australia (formerly AUSLIG), and the data sets are made accessible to scientific users free of charge. These stations form an ideal fiducial network for water vapour estimation projects in Australia.
- Land Victoria is currently establishing a GPS base station network (GPSnet) of 22 stations (<http://www.land.vic.gov.au/>) to support accurate positioning services within Victoria, the hourly data sets are generated and made available online to users with small annual fees.
- Queensland Department of Natural Resources and Mines (NRM) has deployed a GPS Virtual Reference Stations network in South-East Queensland, which currently has 4 stations, with possible extension to cover most of Queensland's regional areas. The system is designed primarily for real-time and near-real-time surveying services, but the data recorded could be provided for the GPS meteorological research.
- In New South Wales, a GPS network of 15 stations is being established for real-time positioning services. The data could also be available for GPS meteorological research.



Figure 1.4 Operational IGS hourly sites in the Australian region (left) and the Land Victoria GPS network (right).

There will be more or extended GPS reference receiver networks and individual stations that could potentially be used for operational water vapour estimation in Australia. To take advantage of these resources for meteorological research and applications there is need to develop internet-based techniques to network these GPS reference stations, and to collect the GPS data on an hourly basis. This is essentially an engineering problem. *The research will overcome these practical problems.*

1.3 The Objectives and Main Contributions of the Study

1.3.1 Major Research Objectives

This research aims to address *a number of critical scientific challenges in measuring atmospheric water vapour content using GPS techniques in near-real-time (NRT) in Australia.* The particular objectives include:

- Build a solid technical basis for ground-based GPS meteorology studies in Australia and demonstrate the technical capability of GPS precipitable water vapour (PWV) estimation with GPS data. This includes the methods of estimation of water vapour from GPS and radiosonde data, estimation of mean weighted temperature in Australia, GPS data processing software and strategies, experimental analysis of the data from the Australian Regional

GPS Network (ARGN) and Australia Upper Air Network (AUAN). With this basis, follow-up studies in this thesis can address the new challenges;

- Develop techniques to allow estimation of atmospheric water vapour from GPS data with the surface meteorological observations collected around the GPS sites. Ideally a dedicated meteorological sensor needs to be installed adjacent to the GPS antenna. However, there are no meteorological sensors at ARGN and GPSnet stations. To install a new meteorological sensor at each GPS station will involve an additional cost of the level of one-third or half of the geodetic GPS receiver cost. In this study, we use the hourly collected surface meteorological data from the Australian Automatic Weather Station (AWS) network operated by Bureau of Meteorology (BOM) to address this challenge;
- Study ocean tidal loading and its effects on GPS PWV estimates in Australia. As shown in Figure 1.4, most ARGN stations and IGS hourly sites in the region are located along the coast or on islands. The periodic motion of the Earth's surface due to "ocean loading" is one of the largest periodic motions in such areas. However, very little work has been done to quantify their effects on GPS-derived solutions at these sites. This research presents a theoretical analysis and experimental results from the ARGN network, focusing on the ocean loading and its effects on GPS-derived precipitable water vapour estimates;
- Development of techniques for estimating high-rate SWV values for future operational meteorological applications in Australia, including addressing such issues as slant-path delay recovery from post-fit double-difference residuals, and overcoming site multipath effects;
- Develop methods that can use the existing and anticipated continuously operating GPS reference stations in the Australian region to measure the atmospheric water vapour content in near-real-time (NRT) in order to address meteorological applications in Australia.

1.3.2 Contributions and Benefits of the Research

The significant contributions of this research can be surmised as follows:

- The research takes advantage of currently operating GPS reference stations in Australia and the neighbouring region, that were/are established for positioning and navigation applications, along with the hourly Automatic Weather Stations (AWS) that serves the atmospheric communities. This adds significant extra 'value' to these existing (and future) infrastructures. From the perspective of the network operators, this research may generate scientific and commercial benefits with modest additional infrastructure investment.
- For the first time in Australia, the research addresses the problems of implementing a demonstration network for ground-based GPS meteorological research and applications in Australia. This is the necessary first step to a possible 'next-generation' upper-air observing system that could significantly improve numerical weather and storm prediction, as well as address climate study applications. It is unlikely that substantial progress could be made in Australia without building a demonstration system. The number of receivers within the demonstration network will start with ARGN stations and Victoria GPSnet, but will have the capability to ramp-up to include all operating GPS stations in Australia and its neighbourhood, utilising internet-based communications.
- The research tackles the scientifically challenging of SWV estimation problem. It has developed SWV estimation algorithms, which include the mapping of multipath errors in phase measurements and station motions, and extraction of line-of-sight residuals from double-difference residuals.

1.3.3 The Scope and Limitation of the Research

The research is focused on the development of an operational water vapour (PWV and SWV) estimation system using current (and anticipated) Australian GPS receiver networks. As a by-product, ionospheric total electron content (TEC) maps over the network coverage area can also be generated on an hourly basis. But this is not the research focus of this thesis. The research effort will be limited to the evaluation and representation of GPS water vapour estimates, not on the assimilation of water vapour data to numerical weather prediction models. However, future research efforts beyond this study may be made to engage

meteorological scientists so that the PWV and SWV estimates can be incorporated into numerical weather prediction models.

1.4 Organisation of the Thesis

This thesis is organised as follows:

Chapter 1 introduces the concepts of GPS Meteorology and gives an overview of current developments of this new technology, and describes the objectives and contributions of the research.

Chapter 2 summarises the principles of the existing ground-based precipitable water vapour (PWV) estimation techniques. We first give a brief overview of the atmospheric delays induced in GPS signals. Next, the tropospheric delay modelling, mapping function, mean weighted temperature and the conversion of wet delay into precipitable water vapour are discussed in detail. This part of the work is drawn from the literature and provides a theoretical basis for GPS water vapour estimation.

Chapter 3 presents the experimental results of the analysis of observations from the Australian Regional GPS Network, which focus on GPS-PWV estimation, radiosonde-PWV estimation, and estimation of mean weighted temperature and PWV solution analysis.

Chapter 4 develops a methodology for GPS water vapour estimation using surface meteorological data from Australian Automatic Weather Stations. The accuracies of interpolated temperature and pressure, or derived Zenith Total Delay (ZTD), with meteorological observations from a local or regional ground AWS network are assessed. The GPS derived PWV using interpolated meteorological data are then compared to the radiosonde PWV to evaluate their consistency.

Chapter 5 investigates the impact of ocean loading on GPS PWV estimates. The GPS data over a three-month period collected from ARGN are processed,

indicating that ocean-loading modelling must be properly implemented when estimating PWV parameters from GPS data.

Chapter 6 discusses the technique for slant water vapour estimation, including addressing such issues as slant-path delay recovery from post-fit double-difference residuals, and overcoming site multipath effects. The experimental results are also presented and analysed.

Chapter 7 discusses the technical issues related to Near-Real-Time GPS PWV estimation, including the data requirements for meteorological and climate applications, near-real-time data processing, and quality control procedures for GPS orbits. The experimental GPS PWV results from near-real-time and post data processing are compared.

Finally, Chapter 8 summarizes the main findings of this study and makes suggestions for future research.

In addition to the above chapters, Appendix A provides some useful meteorological constants and equalities that have been used in the studies. Appendix B lists the ITRF 2000 coordinates for the ARGN stations. Appendix C gives the ocean loading tide coefficients for the ARGN stations.

Chapter 2

Principles of Water Vapour Estimation: Concepts, Models and Estimations

In this chapter, we first give a brief overview of the atmospheric delays induced in GPS signals. Next, the tropospheric delay modelling, mapping function, mean weighted temperature and the conversion of wet delay into precipitable water vapour are discussed in detail.

2.1 The Atmospheric Delay

The Earth is surrounded by the atmosphere, which is composed by distinct layers, as shown in Figure 2.1. When GPS signals travel through the Earth's atmosphere from GPS satellite to the receiver on or near the ground, their speed and direction are changed by the constituents of the atmosphere. This in turn causes a delay on the GPS measurements, which is normally referred to as the Atmospheric Delay. The atmospheric delay mainly occurs in the tropospheric and ionospheric regions, accordingly known as Tropospheric Delay and Ionospheric Delay. Other layers of the atmosphere also affect the propagation of GPS signals, but their effects are very small and are normally not taken into account.

2.1.1 Ionospheric Delay

The ionosphere is a layer or layers of ionized air surrounding the Earth extending from about 50 km above the Earth's surface to altitudes of 1000 km or more. The air is extremely thin at these altitudes. When the atmospheric particles are ionized by radiation (principally by solar ultraviolet radiation and x-rays emissions), they tend to remain ionized due to few collisions between free negatively charged electrons, positively charged atoms and molecules. These ionized particles (called ions) characterize the ionosphere. Among of them, the free electrons affect the propagation of radio waves, and thus the GPS signals.

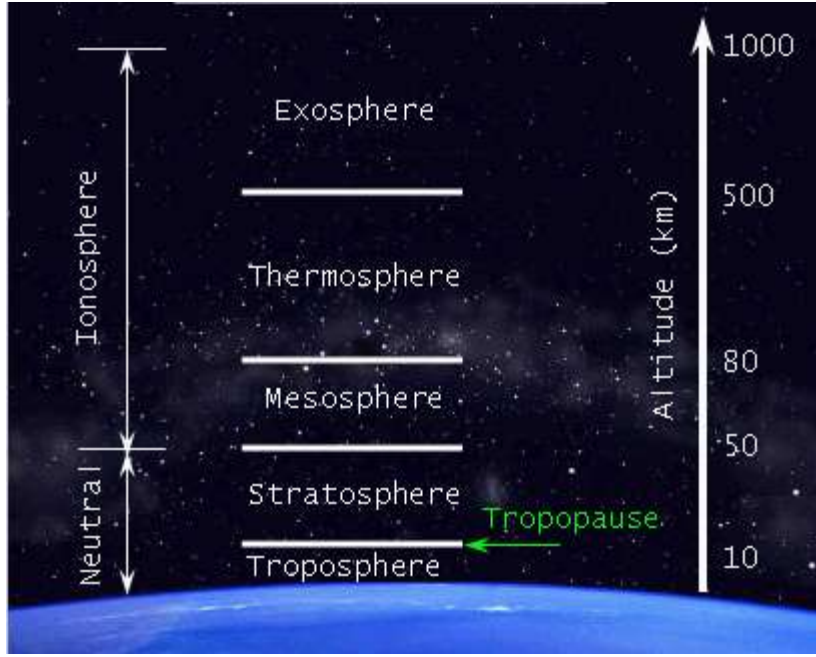


Figure 2.1 Layers of the Earth's Atmosphere. Note that the thermosphere ranges to a height of 500km or so and the ionosphere to more than 1,000km.

The ionosphere is a dispersive medium for radio waves, which means that the modulation on the carrier and carrier phases are affected differently, and this effect is a function of the carrier frequency. The ionospheric delay is therefore frequency dependent and can be determined and effectively eliminated by using dual-frequency GPS receivers. The ionosphere-free (IF) phase measurement Φ_{IF} can be formed through a linear combination of L1 phase Φ_{L1} and L2 phase Φ_{L2} measurements:

$$\Phi_{IF} = \frac{f_1^2}{f_1^2 - f_2^2} \Phi_{L1} - \frac{f_2^2}{f_1^2 - f_2^2} \Phi_{L2} \quad (2.1)$$

where Φ_{IF} is the ionosphere-free carrier phase, Φ_{L1} is the phase of the primary carrier (L1) with frequency f_1 , and Φ_{L2} is the phase of the secondary carrier (L2) with frequency f_2 .

It should be noted that the ionospheric delay can not be fully corrected via the ionosphere-free combination because there are some approximations involved. For instance, it is assumed that the L1 and L2 signals follow the same path through the ionosphere, but it is not quite true. The separation of the ray paths may reach up to 35m under severe ionospheric turbulence. The remaining ionospheric

effects can be further reduced by double-differencing of the combined observations. The IONEX files from IGS can also be used to estimate the ionospheric delay.

2.1.2 Tropospheric Delay

Below the ionosphere is the neutral atmosphere, including the stratosphere, tropopause, and troposphere. The troposphere is the bottom portion of the Earth's atmosphere, which is the layer of weather on the Earth. The thickness of the troposphere varies from less than 8km over the poles to in excess of 16km over the equator. The temperature decreases with an increase in altitude in the troposphere, by approximately $-6.5^{\circ}\text{C}/\text{km}$ [NOAA/NASA/USAF, 1976].

The troposphere contains about 75% of the atmosphere's mass and most of the water vapour in the atmosphere. Water cycling takes place in the troposphere as the exchange and movement of water between the Earth's surface and atmosphere. Solar energy causes water to evaporate, and wind circulates the moisture. Air rises, then expands and cools down condensing water vapour and thus developing clouds. Various types of precipitation happen depending upon size and temperature of water particles. Consequently, the troposphere is undergoing temporal and seasonal variations.

The stratosphere and tropopause are above the troposphere. The stratosphere, tropopause, and troposphere are the electrically neutral atmosphere, which is a non-dispersive medium for radio waves at frequency less than 15GHz. Thus, the propagation is frequency independent. Consequently, the effect of the neutral atmosphere due to non-ionised gases (e.g., carbon dioxide) and water vapour molecules on both the GPS carrier phases and code modulation, which is denoted as tropospheric delay², is identical and cannot be eliminated using dual-frequency observations. The tropospheric delay varies with temperature, pressure, and humidity as well as the physical location of the receiver, and reaches up to 2.5m in the zenith direction, and about 30m close to a horizon angle.

² This is slightly incorrect because it excludes the other two parts of the neutral atmosphere, which contribute as well. However, the dominant contribution of the troposphere justifies the notation.

2.2 Modelling of Tropospheric Delay

2.2.1 Tropospheric Delay Models Based on Atmospheric Refractivity Profiles

The troposphere affects GPS radio signals in two distinct ways. First, the signal bends in response to gradients in the index of refraction of the atmosphere, travelling a curved path in contrast with the straight line path the signal would travel in a region of constant refractivity. The difference between the lengths of these two paths is known as the Geometrical Delay. Second, the waves travel slower in a region of finite density than they would in a vacuum. The increase in the time required to cover a given distance can also be expressed in term of excess path length. The total delay, then, is the sum of these two components and can be written as [Rocken *et al.*, 1993]:

$$\Delta L = \int_L n(s)ds - G \quad (2.2)$$

where ΔL is the total tropospheric delay stated in terms of the equivalent increase in path length, $n(s)$ is the index of refraction which varies as a function of position along the curved ray path L , and G is the geometrical straight line path length through the atmosphere. Equivalently,

$$\Delta L = \int_L [n(s) - 1]ds - [S - G] \quad (2.3)$$

where S is the curved path length along L . In this form, the first term on the right is due to the slowing effect, and the second term is due to bending. The bending term $[S - G]$ is much smaller, about 1cm or less, for paths with elevations greater than about 15° . For rays oriented along the zenith, and in the absence of horizontal gradients in n , the ray path is a straight line and the bending term vanishes. Equation (2.3) becomes:

$$\Delta L^0 = \int_L [n(s) - 1]ds \quad (2.4)$$

where ΔL^0 is the total tropospheric delay in the zenith direction, which is normally referred to as Zenith Tropospheric Delay or Zenith Total Delay (ZTD). The integral is along the zenith path, and the delay is given in units of s.

Equations (2.3) and (2.4) are often formulated in terms of atmospheric refractivity N rather than the index of refraction, which is defined by:

$$N = 10^6 (n - 1) \quad (2.5)$$

The atmospheric refractivity N is central to all theories concerning radio wave propagation through the neutral atmosphere. The classic expression for the atmospheric refractivity is [Smith and Weintraub 1953]:

$$N = k_1 \frac{P_d}{T} + k_2 \frac{P_v}{T} + k_3 \frac{P_v}{T^2} + k_4 \frac{P_c}{T^2} \quad (2.6)$$

where P_d , P_v , and P_c are the partial pressures of the dry gases, water vapour, and carbon dioxide respectively, in mbar, and T is the absolute temperature in Kelvin. The refraction coefficients $k_1 - k_4$ were determined empirically using laboratory measurements and have the following values [Bean and Dutton, 1966, pp. 6-7]:

$$k_1 = (77.607 \pm 0.13) K mbar^{-1}$$

$$k_2 = (71.6 \pm 8.5) K mbar^{-1}$$

$$k_3 = (3.747 \pm 0.031) \cdot 10^5 K^2 mbar^{-1}$$

$$k_4 = (5/3) \cdot k_1$$

In Equation (2.6) the influence of the carbon dioxide of the atmosphere can be omitted since its partial pressure is a very small portion of the total pressure (approximately 0.03%) and has no significant effect on the final results.

A more accurate formula for refractivity is provided by Thayer [1974] by taking into account the non-ideal gaseous behaviour of the atmosphere:

$$N = k_1 \frac{P_d}{T} Z_d^{-1} + k_2 \frac{P_v}{T} Z_v^{-1} + k_3 \frac{P_v}{T^2} Z_v^{-1} \quad (2.7)$$

where Z_d^{-1} and Z_v^{-1} are the inverse compressibility factors (corrections for the small departures of the moist atmosphere from an ideal gas) for dry air and water vapour respectively. The expressions for the inverse compressibility factors are given by Owens [1967]:

$$Z_d^{-1} = 1 + P_d \cdot (57.97 \cdot 10^{-8} \cdot (1 + \frac{0.52}{T}) - 9.4611 \cdot 10^{-4} \cdot \frac{t}{T^2}) \quad (2.8)$$

$$Z_v^{-1} = 1 + 1650 \cdot \frac{P_v}{T^3} \cdot (1 - 0.01317 \cdot t + 1.75 \cdot 10^{-4} \cdot t^2 + 1.44 \cdot 10^{-6} \cdot t^3) \quad (2.9)$$

where T and t are the temperatures in Kelvin and Celsius respectively. The constants of Equation (2.7), discussed by Bevis *et al.* [1994], have the following

values:

$$k_1 = (77.6 \pm 0.05) K mbar^{-1}$$

$$k_2 = (70.4 \pm 2.2) K mbar^{-1}$$

$$k_3 = (3.739 \pm 0.012) \times 10^5 K^2 mbar^{-1}$$

More empirical values of the above atmospheric refractivity constants can be found in Appendix A.

The first term of the right hand side of the above equation for refractivity (Equation 2.7) is usually called dry refractivity N_d , while the last two form the so-called wet refractivity N_w . Thus:

$$N = N_d + N_w \quad (2.10)$$

Davis et al. [1985] presented a more compact form for the refractivity formula using the gas law:

$$P_i = Z_i \rho_i R_i T \quad (2.11)$$

where P_i is the partial pressure of an atmospheric constituent, ρ_i is the mass density, and R_i the specific gas constant for that constituent. This finally gives:

$$N = k_1 R_d \rho + k_2' \frac{P_v}{T} Z_v^{-1} + k_3 \frac{P_v}{T^2} Z_v^{-1} \quad (2.12)$$

where ρ is the total mass density of the air. The derived constant k_2' is given by *Bevis et al.* [1994] as:

$$k_2' = k_2 - k_1 \frac{M_w}{M_d} = (22.1 \pm 2.2) K mbar^{-1} \quad (2.13)$$

where M_w and M_d are the molar weight of wet air and dry air respectively.

The first term of the right hand side of Equation (2.12) is called the hydrostatic refractivity N_h , while the other two form the wet refractivity N_w . Thus:

$$N = N_h + N_w \quad (2.14)$$

It is important to remember the basic differences in the definition of the total refractivity as given by Equations (2.10) and (2.14), since in the second one, part of the water vapour influence has been absorbed into the hydrostatic part. In terms of these equations we can separate the atmospheric delay also into dry or hydrostatic delay and wet delay. The formulae in the thesis will be based on the

hydrostatic delay mainly, so we can write the zenith tropospheric delay (Equation 2.4) as:

$$\Delta L^0 = \int_L [n(s) - 1] ds = 10^{-6} \int_L N ds = 10^{-6} \int_L N_h ds + 10^{-6} \int_L N_w ds = \Delta L_h^0 + \Delta L_w^0 \quad (2.15)$$

where ΔL_h^0 is the zenith hydrostatic delay (ZHD) and ΔL_w^0 is the zenith wet delay (ZWD).

If the vertical refractivity profiles are available, for instance, from data collected by radiosonde or from numerical weather fields, the zenith delay components can be obtained by integration of the vertical refractivity profiles as:

$$ZHD = 10^{-6} \int_h N_h(h) dh = 10^{-6} \int_h (k_1 R_d \rho) dh \quad (2.16a)$$

$$ZWD = 10^{-6} \int_h N_w(h) dh = 10^{-6} \int_h (k_2' \frac{P_v}{T} Z_v^{-1} + k_3 \frac{P_v}{T^2} Z_v^{-1}) dh \quad (2.16b)$$

$$ZTD = ZHD + ZWD = 10^{-6} \int_h N(h) dh \quad (2.16c)$$

2.2.2 Empirical Models of Zenith Tropospheric Delay

The zenith delay components can be obtained by integration of the vertical refractivity profiles. The vertical refractivity profiles can be provided from radiosonde measurements. But this is a very costly approach. Instead, some empirical models have been developed to estimate the zenith tropospheric delay through surface meteorological data – temperature and pressure. In the following, we introduce some common empirical models for ZHD and ZWD calculations.

2.2.2.1 Zenith Hydrostatic Delay Models

The zenith hydrostatic delay can be calculated using an empirical model that makes use of surface meteorological measurements. The most popular models belong to Hopfield and Saastamoinen models. Several studies [Bevis and Businger, 1995; Gendt and Beutler, 1995; Dodson et al., 1996] have stated that these models are accurate to a few millimetres when using accurate surface pressure data.

Hopfield Hydrostatic Delay Model

The zenith hydrostatic delay of the Hopfield model can be written as [Hofmann-Wellenhof, 1997]:

$$ZHD = \Delta L_h^0 = \frac{10^{-6}}{5} \cdot [40136 + 148.72 \cdot (T_s - 273.16)] \cdot 77.64 \cdot \frac{P_s}{T_s} \quad (2.17)$$

where P_s is the surface pressure at the station in mbar, and T_s is the surface temperature in Kelvin.

Saastamoinen Hydrostatic Delay Model

The Saastamoinen model for zenith hydrostatic delay (ZHD), in metres, is expressed as:

$$ZHD = \Delta L_h^0 = (0.0022779 \pm 0.00024) \frac{P_s}{f(\varphi, H)} \quad (2.18)$$

where P_s is the surface pressure in mbar, and

$$f(\lambda, H) = (1 - 0.00266 \cos 2\varphi - 0.00028H) \quad (2.19)$$

accounts for the variation in gravitational acceleration with latitude λ (in radians), and the height H of the surface above the ellipsoid (in kilometres).

Comparison of Zenith Hydrostatic Models

To assess the accuracy of the above empirical ZHD models, 19-month radiosonde data at ARGN site ALIC from Jan 1999 to July 2000 was analysed and zenith hydrostatic delays were calculated from the integration of Equation (2.16a). With the help of the surface meteorological data over the same period, ZHD were also computed using the Saastamoinen and Hopfield models. The ZHD from radiosonde data was used as a reference to compare the ZHD computed from the models. There were a total of 500 comparisons. The results are summarized in Table 2.1. From Figure 2.2 we can clearly see that the Saastamoinen model is in good agreement with the Hopfield model, with the mean difference and standard deviation being less than 1mm. But compared to the results from radiosondes, there is a systematic offset between the result from the models and that from the

radiosondes. The offset reaches up to 3.76cm for the Saastamoinen model and 3.85cm for the Hopfield model. But the standard deviation is small, only about 0.5cm for both models. This means that the Saastamoinen and Hopfield ZHD models are approximately 5mm accurate compared with the radiosonde results after the systematic offset is removed. Thus they can be used for GPS-PWV estimation.

Table 2.1 Comparison of empirical ZHD models with the radiosonde derived ZHD.

	Max (cm)	Min (cm)	Mean (cm)	RMS (cm)	Std dev. (cm)
Saas–Radiosonde	5.56	2.04	3.76	3.79	0.49
Hopfield–Radiosonde	5.65	2.12	3.85	3.89	0.50
Hopfield -Saas	0.22	-0.04	0.09	0.12	0.07

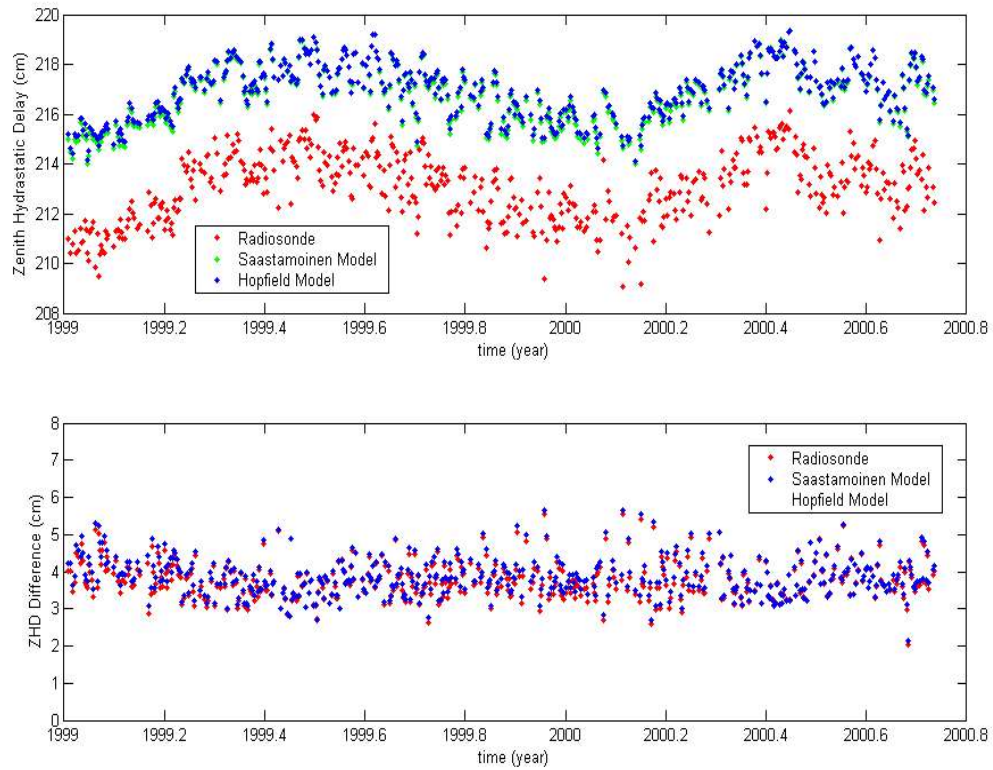


Figure 2.2 Comparison of empirical ZHD models with the radiosonde derived ZHD.

2.2.2.2 Zenith Wet Delay Models

Zenith wet delays are affected by the distribution of water vapour. It is very difficult to derive accurate models using only surface measurements for this component, but it is possible to estimate zenith wet delays as additional parameters during GPS data processing. This issue will be further discussed in

Section 3.2. Nevertheless, some approaches for the approximation of zenith wet delays are given here that may be used for centimetre-level positioning, or serve to predict wet delays in order to initialise the Kalman filter in high precision positioning and GPS meteorological applications.

Hopfield Wet Delay Model

The zenith wet delay of the Hopfield model can be written as:

$$ZWD = \frac{10^6}{5} \cdot (-12.96 \cdot T_s + 3.718 \cdot 10^5) \cdot 11000 \cdot \frac{P_v}{T_s^2} \quad (2.20)$$

where P_v is the partial water vapour pressure at the surface/antenna in mbar, and can be computed with knowledge of surface temperature and relative humidity. T_s is the surface temperature in Kelvin.

Ifadis Wet Delay Model

IFADIS [1986] proposed a model for the zenith wet delay as a function of the surface pressure P_s , partial water vapour pressure P_v and temperature T_s :

$$ZWD = 0.554 \cdot 10^{-2} - 0.880 \cdot 10^{-4} (P_s - 1000) + 0.272 \cdot 10^{-4} \cdot P_v + 2.771 \cdot \frac{P_v}{T_s} \quad (2.21)$$

Comparison of Wet Delay Models

The accuracy assessment for the wet delay models is once again based on the analysis of the radiosonde data described in Section 2.2.2.1. The wet delays in the zenith direction were derived by the integration of Equation (2.16b). Then the wet delay calculated from the above models with the help of surface meteorological data were compared to the radiosonde derived ZWD. The comparison results are listed in Table 2.2 and illustrated in Figure 2.3. It can also be seen that there is a systematic bias of about 4cm in the Hopfield model. After the bias is removed, it is in good agreement with the Ifadis model, with the standard deviation being 1.69cm. Compared to the results from radiosonde, these two models have a similar accuracy of about 4cm. It is much worse than the results from the ZHD

models listed in Table 2.1.

Table 2.2 Comparison of empirical ZWD models with the radiosonde derived ZWD.

	Max (cm)	Min (cm)	Mean (cm)	RMS (cm)	Std dev. (cm)
Hopfield-Radiosonde	3.64	-19.15	-4.03	5.83	4.22
Ifadis-Radiosonde	10.37	-12.39	0.08	3.74	3.75
Ifadis-Hopfield	10.38	1.75	4.11	4.45	1.69

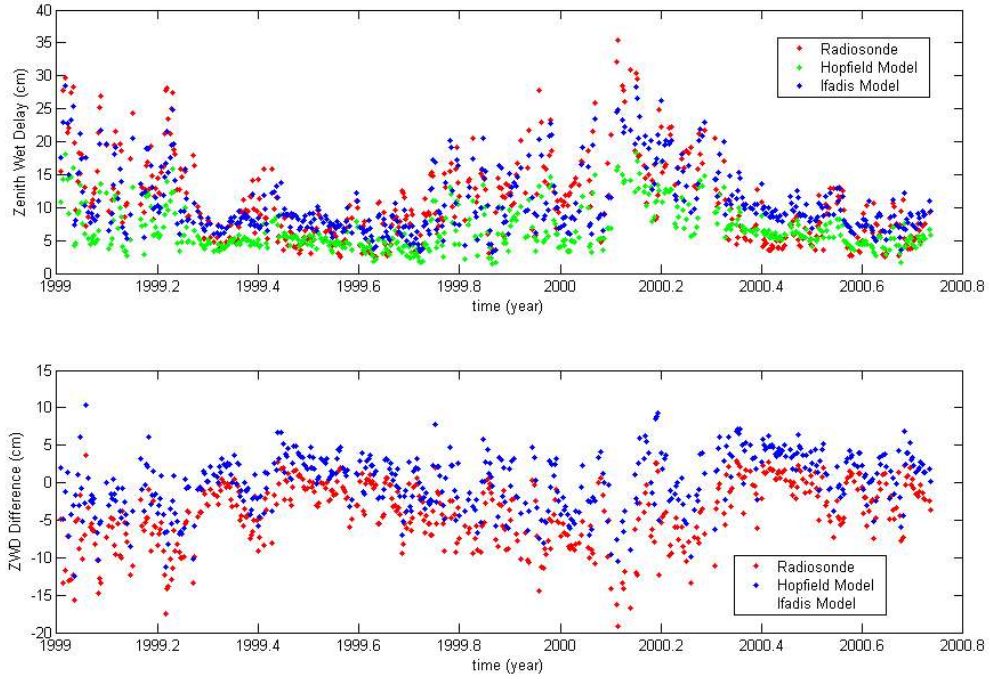


Figure 2.3 Comparison of empirical ZWD models with the radiosonde derived ZWD.

2.2.3 Conversion of Wet Delays into Precipitable Water Vapour

The integrated precipitable water vapour (IWV) is defined as:

$$IWV = \int \rho_v dz = \kappa \Delta L_w^0 \quad (2.22)$$

where ρ_v is the water vapour density profile in the atmosphere, ΔL_w^0 is the zenith wet delay, and the “constant” κ is given by:

$$\frac{1}{\kappa} = 10^{-6} \left(\frac{k_3}{T_m} + k_2' \right) R_v \quad (2.23)$$

where R_v is the specific gas constant for water vapour. Using the definition for mean weighted temperature of the atmosphere T_m :

$$T_m = \frac{\int (P_v / T) \cdot dz}{\int (P_v / T^2) \cdot dz} \quad (2.24)$$

The water vapour content of the atmosphere is sometimes stated as the height of an equivalent column of liquid water, which is referred to as the Precipitable Water Vapour (PWV). Numerically, the IWV is just the product of the density of liquid water ρ_w and PWV. Since PWV and ZWD both have units of length, their ratio

$$\frac{PWV}{ZWD} = \frac{PWV}{\Delta L_w^0} = \frac{\kappa}{\rho_w} \quad (2.25)$$

is a dimensionless quantity. So we can obtain PWV from ZWD using the following equation:

$$PWV = \Pi(T_m) \Delta L_w^0 \quad (2.26)$$

where

$$\Pi(T_m) = \frac{10^6}{\rho_w \left(\frac{k_3}{T_m} + k_2' \right) R_v} \quad (2.27)$$

Figure 2.4 shows the ratio of PWV/ZWD as a function of the mean weighted temperature T_m . Bevis's values for atmospheric refractivity constants k_2' and k_3 (see Appendix A for details) are used here. It can be seen from Figure 2.4 that the relationship between Π and T_m is very nearly linear.

It is possible to estimate the total zenith delay from GPS measurements. Then the estimates of the zenith hydrostatic delay derived from surface meteorological data can be subtracted, leaving the effect due to the zenith wet delay. The factor $\Pi(T_m)$ is then calculated given the information available for the temperature profile at the site. The precipitable water vapour is then calculated from the equation:

$$PWV = \Pi(T_m) (\Delta L^0 - \Delta L_h^0) \quad (2.28)$$

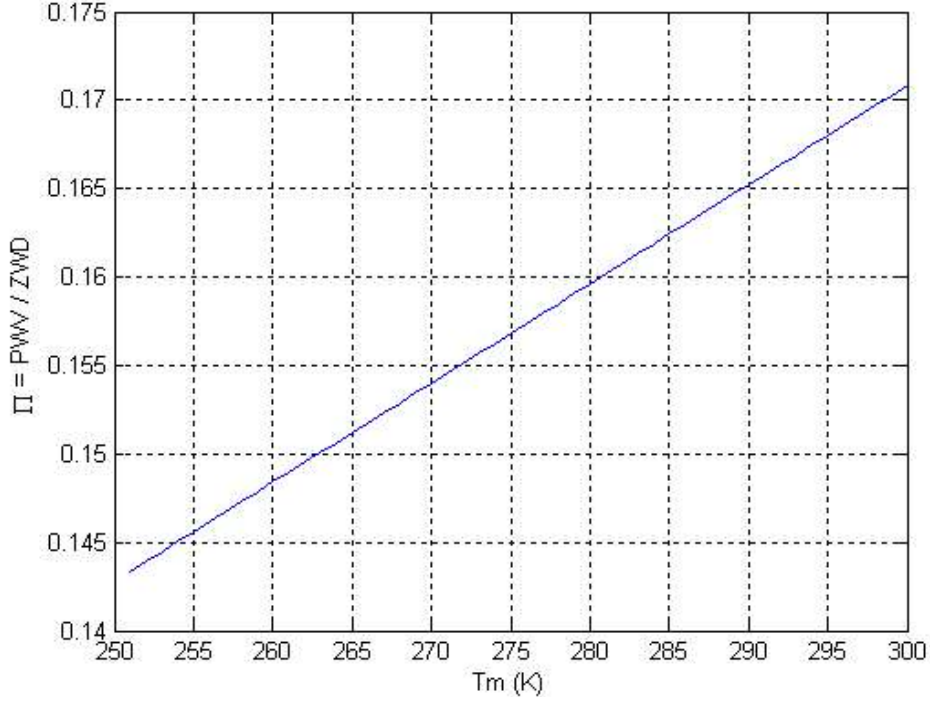


Figure 2.4 The ratio $\Pi = PWV / ZWD$ as a function of the mean weighted temperature T_m .

2.3 Mapping Functions

The GPS measurement is taken along the line-of-sight from the ground station to the satellite that is rarely in the zenith direction. Therefore a mapping function is needed to take into account the dependence on satellite elevation. This mapping is generally taken to be solely a function of elevation and not azimuth, as azimuthally symmetry is assumed. The total tropospheric delay ΔL for a path with an elevation angle ϵ is then modelled as [Bevis *et al.* 1994]:

$$\Delta L = \Delta L_h^0 M_h(\epsilon) + \Delta L_w^0 M_w(\epsilon) \quad (2.29)$$

where $M_h(\epsilon)$ is the Hydrostatic Mapping Function and $M_w(\epsilon)$ is the Wet Mapping Function.

Because of the atmospheric curvature, the mapping function does not just change as the cosecant of the elevation angle ϵ , which would be expected for a plane parallel refractive medium. The hydrostatic mapping function will change according to changes in the ratio of the atmospheric thickness to the Earth's radius, as a result of the changes in temperature [Niell, 1996]. Therefore, the temporal change of mapping function is associated with variability of temperature

at various atmospheric heights, which can be obtained from radiosonde profiles.

Various forms have been proposed for the hydrostatic and wet mapping functions. The most commonly used mapping function in GPS data processing will be presented in the following paragraphs. Moreover, some older - but also usable - types of mapping functions will be also mentioned.

It is emphasized that the choice of a suitable hydrostatic mapping function is much more important than the choice of the wet one, because the hydrostatic delay is about 10 to 20 times larger than the wet delay. Consequently, errors in the hydrostatic mapping function will scale into the slant path delay at much higher magnitude than for the wet delay. Although the hydrostatic delay can be modelled precisely in the zenith direction, care must be taken not to lose this advantage by inappropriate mapping function.

2.3.1 Marini Mapping Function

In 1972, J. W. Marini developed a tropospheric delay correction, which shows that the elevation angle ϵ dependence of any horizontally stratified atmosphere can be approximated by expanding in a continued fraction in term of $1/\sin(\epsilon)$. The general form of the Marini mapping function is written as [Marini, 1972]:

$$M(\epsilon) = \frac{1}{\sin \epsilon + \frac{a}{\sin \epsilon + \frac{b}{\sin \epsilon + \frac{c}{\sin \epsilon + \dots}}}} \quad (2.30)$$

where ϵ is the geometric (unrefracted) elevation angle and a, b, c, \dots are profile dependent coefficients. The Marini mapping function does not explicitly separate the hydrostatic and wet components of tropospheric delays.

2.3.2 Chao Mapping Function

In 1974, C. C. Chao derived a tropospheric mapping function to be used for radio tracking corrections of the 1971 Mariner Mars spacecraft. Chao treats the wet and dry components separately through empirical fitting to an average refractivity

profile derived from two years of radiosonde data [Chao, 1974]:

$$M_h(\epsilon) = \frac{1}{\sin \epsilon + \frac{a_h}{\tan \epsilon + b_h}} \quad (2.31)$$

$$M_w(\epsilon) = \frac{1}{\sin \epsilon + \frac{a_w}{\tan \epsilon + b_w}} \quad (2.32)$$

where $a_h=0.00143$, $b_h=0.0445$, $a_w=0.00035$ and $b_w=0.0170$. The mapping function coefficients are defined as global constants and the fractional expansion is discontinued after the second coefficient. It should be noted that the term $\tan \epsilon$ was used to ensure that both dry and wet mapping functions are 1 at the zenith. The accuracy of the Chao's dry mapping function is 1% down to 1° with respect to the ray trace of the average annual refractivity profiles. The error at this level is too large for accurate geodetic VLBI applications [Niell, 1996]. Due to spatial and temporal variability, Chao's wet mapping function was not sufficiently accurate for space geodetic measurements until the introduction of the Herring mapping function [Niell, 1996].

2.3.3 Davis Mapping Function

The mapping function developed by Davis is for the hydrostatic delay only, and also known as the *CfA 2.2 mapping function*. To increase accuracy at low elevation angles, and to better accommodate local and seasonal variations, Davis *et al.* [1985] modified the Chao's mapping function by adding the fraction of the sine term:

$$M_h(\epsilon) = \frac{1}{\sin \epsilon + \frac{a}{\tan \epsilon + \frac{b}{\sin \epsilon + c}}} \quad (2.33)$$

The mapping function coefficients are defined with help of surface meteorological data as well as other atmospheric properties like the temperature lapse rate and the height of the tropopause:

$$a = 0.001185[1 + 6.071 \cdot 10^{-5}(P_s - 1000) - 1.471 \cdot 10^{-4}P_v + 3.072 \cdot 10^{-3}(T_s - 20) + 0.01965(\beta + 6.5) - 0.005645(H_T - 11.231)]$$

$$\begin{aligned}
b &= 0.001144[1 + 1.164 \cdot 10^{-5}(P_s - 1000) - 2.795 \cdot 10^{-4}P_v + 3.109 \cdot 10^{-3}(T_s - 20) \\
&\quad + 0.03038(\beta + 6.5) - 0.001217(H_T - 11.231)] \\
c &= -0.0090
\end{aligned}$$

where P_s is the surface pressure in mbar, T_s is the surface temperature in Kelvin, P_v is the partial water vapour pressure in mbar, β is temperature lapse rate in Kelvin/km, and H_T is the tropopause height in km. If the temperature lapse rate or the tropopause height is not available, the approximations of *Mendes and Angley* [1998] can be used:

$$H_T = 7.508 + 2.421 \cdot \exp\left(-\frac{t_s}{22.90}\right) \quad (2.34)$$

$$\beta = -5.930 - 0.0359 \cdot t_s \quad (2.35)$$

where t_s is surface temperature in °C. If no surface temperature readings are available, the default values of $H_T = 11.3$ km and $\beta = -6.5^\circ\text{C}/\text{km}$ can be applied (or local mean values if known). The RMS agreement of this mapping function compared with ray tracing is less than 5 mm for all elevations above 5°.

2.3.4 Herring Mapping Function

In 1992, T. A. Herring applied the Marini mapping function, but this correction has been normalized to unity in the zenith direction [*Herring*, 1992]:

$$M(\epsilon) = \frac{1 + \frac{a}{1 + \frac{b}{1 + c}}}{\sin \epsilon + \frac{a}{\sin \epsilon + \frac{b}{\sin \epsilon + c}}} \quad (2.36)$$

Herring derived the coefficients a , b , and c by ray tracing of radiosonde data for 10 sites in Northern America. The surface temperature, site latitude and height above sea level are also introduced to obtain the 3 coefficients.

For the Herring hydrostatic mapping function, the coefficients are:

$$a = (1.2320 + 0.0139 \cdot \cos \phi - 0.0209 \cdot H_s + 0.00215 \cdot (t_s - 10)) \cdot 10^{-3}$$

$$b = (3.1612 - 0.1600 \cdot \cos \phi - 0.0331 \cdot H_s + 0.00206 \cdot (t_s - 10)) \cdot 10^{-3}$$

$$c = (171.244 - 4.2930 \cdot \cos\varphi - 0.1490 \cdot H_s - 0.00210 \cdot (t_s - 10) \cdot 10^{-3}$$

where t_s is the temperature at site in °C, φ is the latitude of the site in radians, and H_s is the height of the site above sea level in km.

The coefficients for the Herring wet mapping function are:

$$a = (0.583 - 0.011 \cdot \cos\varphi - 0.052 \cdot H_s + 0.0014 \cdot (t_s - 10) \cdot 10^{-3}$$

$$b = (1.402 - 0.102 \cdot \cos\varphi - 0.101 \cdot H_s + 0.0020 \cdot (t_s - 10) \cdot 10^{-3}$$

$$c = (45.85 - 1.91 \cdot \cos\varphi - 1.29 \cdot H_s + 0.015 \cdot (t_s - 10) \cdot 10^{-3}$$

2.3.5 Niell Mapping Function

Niell [1996] also uses Herring's continued fraction (Equation 2.36) as the mapping function. But the coefficients are based on temporal changes and geographic location rather than on surface meteorological parameters. For the Niell hydrostatic mapping function, the coefficients are given by the mean and the seasonally varying values:

$$\alpha(\varphi, DOY) = \alpha(\varphi)_{average} - \alpha(\varphi)_{amplitude} \cdot \cos(2\pi \cdot \frac{DOY - DOY_w}{365.25}) \quad (2.37)$$

where α is the mapping function coefficients, either a, b or c in Equation (2.36), separated into average value and amplitude. φ is the site latitude in radians, DOY is day of year. DOY_w is day of year for "maximum winter", 28 for the northern hemisphere and 211 for the southern hemisphere.

The mean value $\alpha(\varphi)_{average}$ and the amplitude of seasonal variations $\alpha(\varphi)_{amplitude}$ are latitude dependent and can be interpolated from the nearest values listed in Table 2.3 and Table 2.4.

Height correction associated with the Niell hydrostatic mapping function is:

$$\Delta M(\epsilon) = \frac{dm(\epsilon)}{dh} H_s \quad (2.38a)$$

$$\frac{dm(\epsilon)}{dh} = \frac{1}{\sin(\epsilon)} - f(\epsilon, a_{ht}, b_{ht}, c_{ht}) \quad (2.38b)$$

where H_s is the station height above sea level in km, and $f(\epsilon, a_{ht}, b_{ht}, c_{ht})$ is a

three-term continued fraction (Equation 2.30). The parameters a_{ht}, b_{ht}, c_{ht} are given in Table 2.5. This correction is added to the value of Equation (2.36).

Table 2.3 Coefficients of the Niell hydrostatic mapping function (average values).

Coefficient	$\varphi = 15^\circ$	$\varphi = 30^\circ$	$\varphi = 45^\circ$	$\varphi = 60^\circ$	$\varphi = 75^\circ$
a	$1.2769934 \cdot 10^{-3}$	$1.2683230 \cdot 10^{-3}$	$1.2465397 \cdot 10^{-3}$	$1.2196049 \cdot 10^{-3}$	$1.2045996 \cdot 10^{-3}$
b	$2.9153695 \cdot 10^{-3}$	$2.9152299 \cdot 10^{-3}$	$2.9288445 \cdot 10^{-3}$	$2.9022565 \cdot 10^{-3}$	$2.9024912 \cdot 10^{-3}$
c	$62.610505 \cdot 10^{-3}$	$62.837393 \cdot 10^{-3}$	$63.721774 \cdot 10^{-3}$	$63.824265 \cdot 10^{-3}$	$64.258455 \cdot 10^{-3}$

Table 2.4 Seasonal variations/amplitudes of the Niell hydrostatic mapping function.

Coefficient	$\varphi = 15^\circ$	$\varphi = 30^\circ$	$\varphi = 45^\circ$	$\varphi = 60^\circ$	$\varphi = 75^\circ$
a	0.0	$1.2709626 \cdot 10^{-5}$	$2.6523662 \cdot 10^{-5}$	$3.4000452 \cdot 10^{-5}$	$4.1202191 \cdot 10^{-5}$
b	0.0	$2.1414979 \cdot 10^{-5}$	$3.0160779 \cdot 10^{-5}$	$7.2562722 \cdot 10^{-5}$	$11.723375 \cdot 10^{-5}$
c	0.0	$9.0128400 \cdot 10^{-5}$	$4.3497037 \cdot 10^{-5}$	$84.795348 \cdot 10^{-5}$	$170.37206 \cdot 10^{-5}$

Table 2.5 Coefficients of the Niell hydrostatic mapping function (height correction).

Coefficient	$\varphi = 30^\circ$
a_{ht}	$2.53 \cdot 10^{-5}$
b_{ht}	$5.49 \cdot 10^{-3}$
c_{ht}	$1.14 \cdot 10^{-3}$

The coefficients for the Niell wet mapping function are listed in Table 2.6. Seasonal variations are not taken into account in the Niell wet mapping function, nor a height correction. Therefore, only an interpolation in latitude for the average value of each coefficient is required.

Table 2.6 Coefficients of the Niell wet mapping function. This table contains average values in dependency of latitude. Seasonal variations are not modelled for the wet component.

Coefficient	$\varphi = 15^\circ$	$\varphi = 30^\circ$	$\varphi = 45^\circ$	$\varphi = 60^\circ$	$\varphi = 75^\circ$
a	$5.8021897 \cdot 10^{-4}$	$5.6794847 \cdot 10^{-4}$	$5.8118019 \cdot 10^{-4}$	$5.9727542 \cdot 10^{-4}$	$6.1641693 \cdot 10^{-4}$
b	$1.4275268 \cdot 10^{-3}$	$1.5138625 \cdot 10^{-3}$	$1.4572752 \cdot 10^{-3}$	$1.5007428 \cdot 10^{-3}$	$1.7599082 \cdot 10^{-3}$
c	$4.3472961 \cdot 10^{-2}$	$4.6729510 \cdot 10^{-2}$	$4.3908931 \cdot 10^{-2}$	$4.4626982 \cdot 10^{-2}$	$5.4736038 \cdot 10^{-2}$

2.3.6 Comparison of Mapping Functions

Mendes [1998] has analysed the mapping functions by comparing them against radiosonde profiles from 50 stations distributed worldwide (32,467 benchmark

values). The models that meet the high standards of modern space geodetic data analysis are the Ifadis, Lanyi, Herring, and Niell mapping functions. He found that for elevation angle above 15 degrees, the Lanyi, Herring, and Niell mapping functions yield identical mean biases and the best total error performance. At lower elevation angles, the Ifadis and Niell mapping functions are superior.

2.4 Mean Weighted Temperature of the Atmosphere

Section 2.2.3 has introduced the methods of obtaining the precipitable water vapour (PWV) from GPS data. The total precipitable water vapour is directly proportional to the zenith wet delay (ZWD) derived from ground-based GPS measurements. The water vapour weighted vertically averaged temperature of the atmosphere, T_m , is an important parameter in the relation between PWV and ZWD because the accuracy of GPS estimates of PWV is directly related to the accuracy of T_m . Thus the estimation of T_m is an important part of the estimation of the precipitable water vapour.

From Equations (2.24) and (2.26), if the vertical profiles of temperature and water vapour partial pressure were known exactly, then the calculation of T_m and PWV would also be exact. The vertical profiles of temperature and water vapour partial pressure can be obtained from radiosonde data. However, radiosonde sites are currently very sparsely distributed over the world, and the radiosonde balloon is launched only once or twice a day. Such vertical profiles are rarely available. The use of radiosondes is economically inefficient in the long run. The best solution would be a fully-featured, independent way to estimate T_m . In this section we introduce some methods for estimating T_m . The particular method of estimation chosen will depend on the availability of input data (for example, numerical weather prediction model data or the observed surface temperature) and the desired accuracy.

2.4.1 Linear Regression Method

A widely adopted approach used to estimate T_m is the linear regression method. If the Earth's atmosphere were isothermal, then T_m would be constant and equal to the surface temperature. However, since the atmosphere usually has a negative temperature gradient up to the tropopause, T_m will be the average temperature of atmosphere weighted by the pressure of water vapour, as indicated by Equation (2.24). As most water vapour is in the lower 2-3 km of the atmosphere, we should expect that T_m would be correlated with surface temperature T_s . So we can model the T_m as a function of the surface temperature:

$$T_m = a + b \cdot T_s \quad (2.39)$$

The correlation coefficients a and b can be determined by comparison of T_m from Equation (2.24) using radiosonde profiles of P_v and T , and the values of surface temperature reported at the time of launch. *Bevis et al.*, [1994] investigated this correlation by analysing a large quantity of radiosonde data from 13 sites in the United States over a 2-year period. A strong linear correlation between T_m and T_s was found:

$$T_m = 70.2 + 0.72 \cdot T_s \quad (2.40)$$

with RMS scattering about 4.7 K. *Mendes et al.* [2000] presented slightly different coefficients:

$$T_m = 50.4 + 0.789 \cdot T_s \quad (2.41)$$

derived from 50 radiosonde stations and a period of one year.

We have also analysed the radiosonde data and surface temperature data at the ARGN sites for the period from 1999 to 2000 to determine T_m as function of T_s . First the radiosonde profiles were integrated to retrieve the weighted mean temperature T_m using Equation (2.24). Then the coefficients a and b of Equation (2.39) were determined by a least square fit of the 2493 data pairs. We found the relationship between T_m and T_s for the ARGN sites is:

$$T_m = 70.03 + 0.726 \cdot T_s \quad (2.42)$$

with a RMS scattering of about 3.16K. It is almost the same as the Bevis' result (Equation 2.40), which implies that the Bevis' formula is also suitable for the ARGN sites, although it was determined using the data only from the United

States. Figure 2.5 shows T_m versus T_s as well as the regression results. The deviation from the linear regression line is obvious, and a larger spread around the regression line is also noticed.

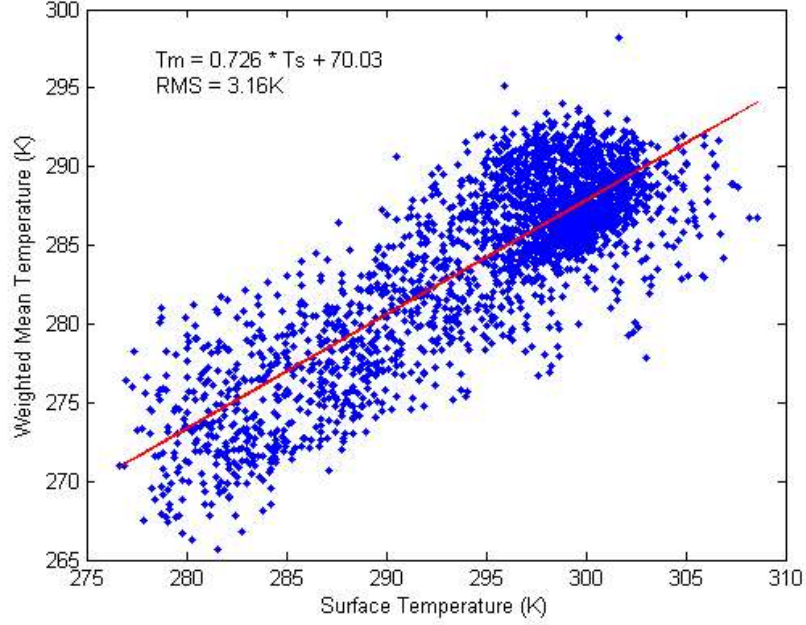


Figure 2.5 Weighted mean temperature T_m as function of surface temperature T_s .

The read solid line is the regression line for the whole data set.

2.4.2 Extended Linear Regression Method

Since T_m depends on the vertical profiles of both temperature and water vapour, it should vary from site to site as well as seasonally. A suitable method to account for the seasonal variations would be to combine the above linear model with a first order harmonic function, which yields the mixed periodic/surface temperature model, so that T_m at the requested day of year (DOY) becomes:

$$T_m = a + b \cdot T_s + c \cdot \cos\left[2 \cdot \pi \cdot \frac{DOY - DOY_w}{365.25}\right] \quad (2.43)$$

where DOY_w is the day of year for "maximum winter", 28 for the northern hemisphere and 211 for the southern hemisphere. The conversion coefficients a , b , c for the ARGN sites are listed in Table 2.7, which are derived by Torben Shueler based on a global-scale analysis of T170L42 GDAS (Global Data Assimilation System) numerical weather fields of the National Centre for Environment Prediction (NCEP, NOAA) from July 1999 to July 2000. The

standard deviation of least square fit (sig), statistical degrees of freedom (f) and minimum, maximum and average surface temperature within the analysis run are also listed in Table 2.7. Applying the function to surface temperatures below or above the defined temperature ranges means that an extrapolation will be performed that may decrease accuracy.

Table 2.7 Conversion coefficients for the mixed mean temperature model for ARGN sites.

Site (mean)	a (M/A)	c [°C]	b [/]	sig [°C]	f	Ts (min)	Ts (max)	Ts
ALIC 021.7	000.8	-1.5	00.357	2.6	17483	003.1	40.8	
CAS1 0-9.5	-12.2	-0.1	00.702	1.8	17483	-33.4	05.1	
COCO 027.7	025.1	00.2	-0.378	1.6	17483	026.2	29.3	
DARW 026.6	007.8	00.1	00.250	2.1	17483	012.2	46.1	
DAV1 -10.8	-13.7	-1.0	00.639	2.0	17483	-35.8	02.6	
HOB2 011.5	0-4.4	-1.1	00.560	2.3	17483	001.6	30.6	
KARR 026.1	009.0	-2.1	00.184	2.5	17483	010.7	41.4	
MAC1 005.6	-12.4	00.6	01.251	2.6	17483	0-4.0	13.2	
MAW1 -13.4	-14.2	-1.0	00.655	2.3	17483	-37.4	02.9	

2.4.3 The Meteorology Models

A more powerful approach to estimating T_m is to use operational meteorology models to predict the actual value of T_m . An advantage of this method is that simultaneous meteorological observations are not needed. *Bevis et al.* [1996] used the output from the United States National Meteorological Center's Nested Grid Model (NGM) to determine T_m . This numerical weather model is run daily using standard surface and upper air observation collected at 00:00 and 12:00 UTC. Radiosonde profiles are the most important part of these observations. Once the initial conditions are established, the NGM is produced by a numerical solution

incorporating grided fields of vapour pressure, temperature and height at nine pressure levels, with a horizontal resolution of $1.25^\circ \times 2.5^\circ$. The forecasts are provided for 6, 12, 18, and 24 hours after initialisation. The model output is resampled and distributed in near-real-time using commercial communication systems.

The water vapour pressure and temperature profiles can be derived anywhere within the NGM by bilinear interpolation. Thus, the weighted mean temperature T_m for any ground station can be estimated by numerical integration of Equation (2.24). However, these forecasts are not free to users. Also the forecast is not continuous, and only provided every six hours. No information on the accuracy is available.

2.5 Estimation of Precipitable Water Vapour from Radiosonde Data

To evaluate the accuracy of the water vapour estimated by GPS, the radiosonde data that were collected locally in the same period were used to calculate the precipitable water vapour. The radiosonde data includes pressure, temperature and relative humidity profiles above the radiosonde station. The Integrated Water Vapour (IWV) along the path of the sounding balloon can be calculated by:

$$IWV = \int \rho_v \cdot dh \quad (2.44)$$

where ρ_v is the density of water vapour. Then the IWV can be mapped into PWV using:

$$PWV = \frac{IWV}{\rho_w} \quad (2.45)$$

where ρ_w is the density of liquid water. According to the gas state equation, the water vapour density ρ_v can be calculated from:

$$\rho_v = \frac{P_v}{R_v \cdot T} \quad (2.46)$$

where $R_v = 461.495 J \cdot K^{-1} \cdot kg^{-1}$ is the specific gas constant for water vapour, and P_v is the partial pressure of water vapour which can be obtained from relative humidity using the following formula recommended by the World Meteorological

Organization (Technical Note No. 8):

$$P_v = RH \cdot \exp(-37.2465 + 0.213166 \cdot T - 2.56908 \cdot 10^{-4} \cdot T^2) \quad (2.47)$$

where RH is relative humidity as a percentage, and T is the absolute temperature in Kelvin.

The observation profiles derived from radiosonde data are discrete series of temperature and relative humidity observations at difference heights. This separates the atmosphere into many layers. Taking P_v and T at each layer in Equation (2.46), we can easily obtain the corresponding water vapour density. If we assume linear water vapour density variation in each layer, Equation (2.45) can be approximated by:

$$PWV = \frac{1}{\rho_w} \sum (h_{j+1} - h_j) \cdot (\rho_v^{j+1} + \rho_v^j) / 2 \quad (2.48)$$

In the above expression, the subscript $j+1$ and j denote the top and bottom of each layer for height and water vapour density.

Chapter 3

Estimating Atmospheric Water Vapour from GPS Observations

GPS signal will suffer from an additional delay when it passes through the troposphere. This delay is eliminated as a nuisance in geodesy and other positioning applications, but it is valuable information for GPS Meteorology. This chapter first outlines the methodology of GPS positioning and extracting the tropospheric delays from GPS observations, and then presents the experimental results derived from data of the Australian Regional GPS Network (ARGN). The background of GPS data processing knowledge is given in brief, since the materials have been covered in detail in a variety of sources such as *Hoffmann-Wellenhof et al.* [1997], *Leick* [2004], *Teunissen* [1998] and *Rizos et al* [1999].

3.1 GPS Observations

GPS observations mainly comprise pseudo-range (or code range) and carrier phase measurements. Phase measurements have a noise level of a few millimetres and are very precise in comparison to code ranges that are only accurate to a few metres or some decimetres at their best. For this reason carrier phases are the primary and most important type of observation for high precision GPS positioning and GPS meteorology, while the pseudo-ranges are treated as ancillary observations and primarily used for synchronizing receiver clocks, resolving ambiguities and repairing cycle slips during the pre-processing stages of advanced GPS analysis.

For high precision positioning, the basic form of the carrier phase observation, normally denoted as the one-way carrier phase observation or zero-difference (ZD) observation, may be written in units of length as:

$$ZD = L = R - \lambda N - \Delta_{ion} + \Delta_{trop} + \Delta_{clk} + \Delta_{hw} + \Delta_{syn} + \Delta_{orien} + \Delta_{pcv} + \Delta_{rel} + e \quad (3.1)$$

where R is the geometrical distance from satellite to receiver, λ is the wavelength of the carrier signal, N is the ambiguity, Δ_{ion} is the ionospheric

delay, $\Delta trop$ is the tropospheric delay, Δclk is the combined receiver and satellite clock errors, Δhw is the hardware bias of the receiver and the transmitter (includes inter-channel and inter-frequency biases), Δsyn is synchronization error, $\Delta orien$ is receiver/transmitter antenna orientation correction, Δpcv is the antenna phase centre offset, Δrel is the relativistic effect and e denotes the residual errors.

The one-way carrier phase observation is seldom used in high precision GPS data processing because these measurements are corrupted by receiver and satellite clock errors. Instead, double-differences are constructed. Firstly, single-differences are formed by differencing the simultaneous one-way measurements from the same satellite to two ground receivers, which eliminates the effect of the error in the satellite clock. If the receivers are closely spaced this measurement also reduces the effects of tropospheric and ionospheric refraction effects. Secondly, the difference between two single-differences is computed to yield the double-difference, which eliminates the two receiver clock errors. It should be noted although receiver clock error can be effectively cancelled in doubly differenced observations, rigorous receiver clock error elimination will only take place if all measurements strictly refer to the same measurement epoch. This means that a synchronization correction may be necessary. However, the pseudo-range measurements, together with reasonable apriori knowledge of the antenna coordinates and satellite position, can be used to determine the offset of the station clock to within a microsecond, adequate to keep clock-related errors in the doubly-differenced phase observations to below 1mm.

Let L_A^1 and L_A^2 be observations of satellites 1 and 2 by receiver A, and L_B^1 and L_B^2 be observations by receiver B. These observations can then be combined into single-differences SD_{AB}^1 and SD_{AB}^2 as:

$$SD_{AB}^1 = ZD_B^1 - ZD_A^1 = L_B^1 - L_A^1 \quad (3.2a)$$

$$SD_{AB}^2 = ZD_B^2 - ZD_A^2 = L_B^2 - L_A^2 \quad (3.2b)$$

and the double-difference can then be expressed as:

$$DD_{AB}^{12} = SD_{AB}^2 - SD_{AB}^1 = (ZD_B^2 - ZD_A^2) - (ZD_B^1 - ZD_A^1) \quad (3.3)$$

For precise positioning with long baselines, dual-frequency GPS receivers are used, which provide dual-band carrier phase measurements. Certain linear combinations of two phase measurements can be formed for specific purposes. Generally speaking, a combined phase measurement can be written as:

$$L_{12} = a_1 \cdot L_1 + a_2 \cdot L_2 \quad (3.4)$$

where a_1 and a_2 are the combination factors for the original L_1 and L_2 carrier phases.

Assuming that the L_1 and L_2 observations are independent and their standard deviation $\sigma_1 = \sigma_2 = \sigma$, according to the law of error propagation, the standard deviation σ_{12} (or "noise level") of the combined phase observation is:

$$\sigma_{12} = \sqrt{(a_1 \cdot \sigma_1)^2 + (a_2 \cdot \sigma_2)^2} = \sigma \sqrt{a_1^2 + a_2^2} = F_\sigma \cdot \sigma \quad (3.5)$$

where F_σ is the factor for noise level of the combined phase observation. If there are systematic errors δL_1 and δL_2 in the original L_1 and L_2 carrier phases, the systematic error in the combined observation would be:

$$\delta L_{12} = a_1 \cdot \delta L_1 + a_2 \cdot \delta L_2 \quad (3.6)$$

Due to the ionospheric refraction being dispersive, we have $\delta L_2 = \frac{f_1^2}{f_2^2} \cdot \delta L_1$, and

Equation (3.6) then becomes [Leinen, 1997]:

$$\delta L_{12} = (a_1 + \frac{f_1^2}{f_2^2} \cdot a_2) \cdot \delta L_1 = F_{ion} \cdot \delta L_1 \quad (3.7)$$

where F_{ion} describes the impact of the first-order ionospheric effect on the linear combination. Specific choices for the values of a_1 and a_2 permit the reduction or elimination of the ionospheric effect.

The most important linear combinations together with their characteristics are summarized in Table 3.1. The ionosphere-free combination L_C can effectively eliminate the effect of the first-order ionospheric propagation delay, and is widely used in GPS data processing for networks of extent from tens to hundreds of kilometres, for distances over which the ionospheric errors are assumed uncorrelated at the two receivers. However, forming L_C also magnifies the effect of other error sources. So on short baselines where the ionospheric errors can be

assumed to have been cancelled in single-differencing, it is preferable to treat L_1 and L_2 as independent observations rather than form the linear combination. In the L_G phase measurements, all geometrical and tropospheric delays are cancelled, so that we have a direct measure of the ionospheric variation. The wide lane and narrow lane can be used to fix cycle slips in one-way data [Blewitt, 1990] or to simplify the L_C ambiguity fixing in GPS data processing.

Table 3.1 Linear Combinations of the L_1 and L_2 observations.

Carrier	a_1	a_2	λ (mm)	F_{ion}	F_σ	Description
L_1	1	0	190	1	1	original L1 signal
L_2	0	1	244	$\frac{f_1^2}{f_2^2}$ 1.65	1	original L2 signal
L_C	$\frac{f_1^2}{f_1^2 - f_2^2}$ 2.25	$-\frac{f_2^2}{f_1^2 - f_2^2}$ -1.55	190	0	2.98	ionosphere-free
L_G	1	-1	∞	-0.65	1.41	geometry-free
L_W	$\frac{f_1}{f_1 - f_2}$ 4.53	$-\frac{f_2}{f_1 - f_2}$ -3.53	862	-1.28	5.74	wide lane
L_N	$\frac{f_1}{f_1 + f_2}$ 0.56	$\frac{f_2}{f_1 + f_2}$ 0.44	107	1.28	.071	narrow lane

3.2 Modelling Tropospheric Delays in GPS Data Processing

As we mentioned earlier, the ionospheric refraction is dispersive and is usually corrected using the ionosphere-free linear combination, which is a standard observable for geodetic applications. The refraction in the neutral atmosphere is not dispersive and its value cannot be derived directly from the measurements. It can only be derived by estimation techniques along with other parameters during GPS data processing.

Doubly-differenced carrier phase observations are free of clock errors but have carrier phase ambiguities. The ambiguities have two important properties. While the GPS receiver maintains signal lock, the cycle ambiguities remain constant and they are integer multiples of the GPS carrier wavelength. The carrier phase

ambiguities and tropospheric delay can be distinguished because the former remains constant while the latter changes roughly as $1/\sin(\text{satellite elevation angle})$. Thus, ambiguities and tropospheric delay can be estimated simultaneously.

There are several ways to model tropospheric delays in GPS data processing. One may choose to predict the zenith hydrostatic delay (ZHD) from surface meteorology measurements and model only the zenith wet delay (ZWD). In this case the ZWD model will tend to absorb residual errors in ZHD. Another approach is to measure the wet delay, e.g. using a water vapour radiometer (WVR), and to model only the residual wet delay due to the instrumental and calibration errors of the WVR. In some situations it is reasonable to model the zenith total delay (ZTD) as a single entity. The following discussion assumes that the ZWD is being modelled, but keep in mind that further generalization is possible.

The simplest estimation approach is to assume that the ZWD is constant for a given time interval and to estimate its value as part of the overall least-square process. Typically the ZWD is assumed to be a constant over an interval ranging from 30 minutes to several hours, depending on the length of the observation span. This may mean that up to 49 tropospheric parameters are estimated at each station for a 24-hour data period. This deterministic approach usually involves placing some constraints on the value of the ZWD, and perhaps on its rate of change, to keep it within reasonable bounds.

A more sophisticated approach considering the temporal variation of the ZWD has exploitable statistical properties. The ZWD is unlikely to change by a large amount over a short period of time (such as 15min). In fact, the ZWD can be viewed as a stochastic process, and the process parameters can be estimated using a Kalman filter or a related class of optimal filters based on the state-space, time domain formulation [Gelb, 1974]. Some GPS processing software model clock errors as a stochastic process whose parameters are estimated along with the tropospheric parameters [Herring *et al.*, 1990]. In order to estimate the ZWD, or an alternative tropospheric quantity, via a stochastic filter, it is necessary to choose a specific class of stochastic process to represent fluctuations in this

tropospheric parameter. Ideally this choice would be based on insight into the underlying physical processes. In practice, the class of stochastic process is usually selected on the basis of the observed power spectrum of the system being modelled. Most researchers assume that the ZWD can be modelled as a *random walk process* or as a *first-order Gauss-Markov process* [Herring et al., 1990]. The stochastic process noise typically is chosen so as to constrain the variation of the ZWD to between 1 and 20mm per hour, depending on location and time of year.

For GPS networks with receiver spacing of less than several hundred kilometres, a significant problem is encountered in estimating zenith total delay or zenith wet delay. The ZTD or ZWD estimates contain unusually large but highly correlated errors. The problem arises because receivers at each end of a short baseline observe the satellite at almost identical elevation angles, which leads to the partial derivative of phase or pseudo-range with respect to the zenith delay parameter (which is simply the mapping function and approximately equal to the cosecant of the elevation angle) being nearly equal, producing high correlations among the estimated zenith delays. Although the uncertainties in all of the zenith-delay parameters will be large, the relative values of the estimates themselves can be accepted. Accordingly a GPS network of limited spatial extent can estimate the relative values of the ZWD and thus PWV more accurately than it can estimate the absolute values of these quantities. This problem can be solved by using global tracking stations to augment a small regional network, thereby introducing large inter-station spacing and de-correlating the ZWD estimates.

3.3 Least Squares Parameters Estimation

Linearization of the observation Equation (3.3) around the apriori parameters and observations X_0 , results, in matrix form:

$$V = A \cdot \delta X + W \quad (3.8)$$

where A is the design matrix, δX is the vector of corrections to the unknown parameters X , $W = f(X_0)$ is the misclosure vector, and V is the vector of residuals.

The partial derivatives of the observation equations with respect to X , consisting of five types of parameters: station positions, satellite orbits parameters (initial

conditions, radiation parameters and phase centre offsets), Earth orientation parameters (EOP), atmospheric delay parameters (time dependent zenith delays and gradients) and carrier phase ambiguities, form the design matrix A .

The least squares solution with apriori weighted constraints P_x to the parameters is given by:

$$\delta X = -(P_{X_0} + A^T P_x A)^{-1} A^T P_x W \quad (3.9)$$

so that the estimated parameters are:

$$\hat{X} = X_0 + \delta X \quad (3.10)$$

with covariance matrix:

$$C_{\hat{X}} = P_{\hat{X}}^{-1} = (P_{X_0} + A^T P_x A)^{-1} \quad (3.11)$$

Since the functional (mathematical) model (Equation 3.3) relating the observations and parameters is non-linear, the least-square fit for each session may need to be iterated until convergence, i.e., until the corrections to the estimated station coordinates and other parameters are negligible.

3.4 GPS Data Processing Scheme and Software

3.4.1 GPS Data Processing Scheme

Generally, GPS data processing involves the following steps:

- (a) Data collection
 - Collect GPS orbits from data centres of the International GPS Services (IGS);
 - Collect GPS data from local, regional or global GPS networks; and
 - Collect surface meteorological data and radiosonde data (if available) from local meteorology agencies.
- (b) Estimating tropospheric delay (ZTD or ZWD) and other geodetic parameters, such as site coordinates using GPS processing software package.
- (c) Retrieving IWV or PWV from tropospheric delay estimates.
- (d) Validation with radiosonde data, or assimilation into numerical weather prediction models, or for other meteorological applications.

The data processing scheme in the case of the GAMIT software is summarized in Figure 3.1.

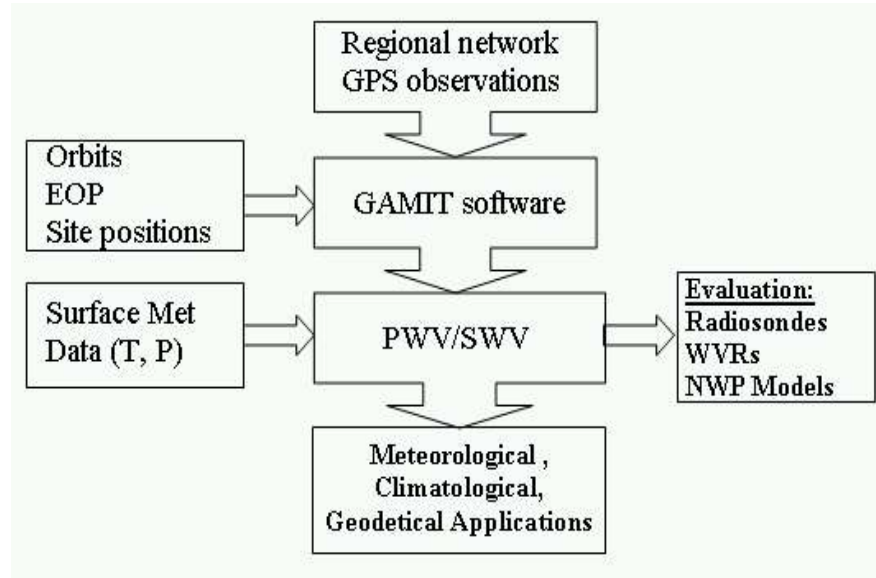


Figure 3.1 GPS data processing scheme.

3.4.2 GPS Data Processing Software

There are three principal developed software packages used for GPS Meteorology data processing. They are the *GAMIT* package developed by Massachusetts Institute of Technology (MIT) and Scripps Institution of Oceanography (SIO), the *GIPSY* package developed at the Jet Propulsion Laboratory (JPL), and the *BERNESE* package developed at the University of Berne. These software packages were originally developed for geodetic positioning and GPS satellite orbit determination. But they have been adopted for estimating the tropospheric delay parameters to meet the needs of GPS Meteorology.

In 1999, the CRCSS was granted a full licence for the use of the *GAMIT* package by MIT to conduct the GPS Meteorology research in Australia. It has been used to process the GPS data in this study.

Although there are several software packages that can be used for GPS

Meteorology applications, the data processing is still a rather complicated professional task because of the large number of unknowns that must be estimated in addition to the water vapour parameters. These include the orbital parameters of the GPS satellites, long period variations in the rotational parameters of the Earth, and the precise positions of the receivers. It requires the user to have a high level of understanding of these tools.

3.5 Experimental Studies

3.5.1 Experimental Description

The purposes of the experimental study using an Australian network are threefold: first, to establish GPS-PWV estimation capability and demonstrate the feasibility of operational GPS water vapour estimation in an Australian network; second, to test PWV estimation algorithms from GPS zenith tropospheric delay (ZTD) measurements and radiosonde measurements; and third, to assess the performance of GPS derived PWV by comparing GPS-PWV with Rad-PWV solutions.

The experimental studies are based on the GPS data collected by the Australian Regional GPS Network (ARGN), operated by Geoscience Australia (formerly the Australian Land Information Group, AUSLIG, see Figure 3.2). ARGN currently consists of 156 permanent continuously operated stations with geodetic quality GPS receivers on geologically stable marks, providing the geodetic framework for the spatial data infrastructure in Australia and its territories. Nine of these stations are located closely to the radiosonde sites of the Australian Upper Air Network (AUAN, Figure 3.3), which consists of a total of 52 sites in Australia, including two sites in Macquarie and Cocos Islands, and three sites in Antarctica (Davis, Casey and Mawson). The GPS tracking data were collected at a rate of 30 seconds. The data for 92 days (from 1 July to 30 September 2000) were retrieved and analysed for this study. This network operates primarily for geodetic and geodynamic purposes, and does not provide surface meteorological data. The radiosonde data for the same period were provided by the Australian Bureau of Meteorology (BOM). Radiosondes are released once or twice daily at about UTC 23:00 or 00:30 from these 9 collocated sites. Surface meteorological data were

collected every 30 minutes at Alice Springs, Cocos Island, Darwin, Hobart and Townsville. The sites in Macquarie Island and Antarctica record the meteorological data every 3 hours. We estimated GPS zenith tropospheric delays using the GAMIT software every 30 minutes to match the radiosonde release times and the 30 minutes meteorological data interval. In principle, we can interpolate the 3-hourly meteorological observations to the radiosonde release times. This however may introduce additional uncertainty when comparing the two solutions. In the following discussion the analysis focuses on the results from the first five sites.

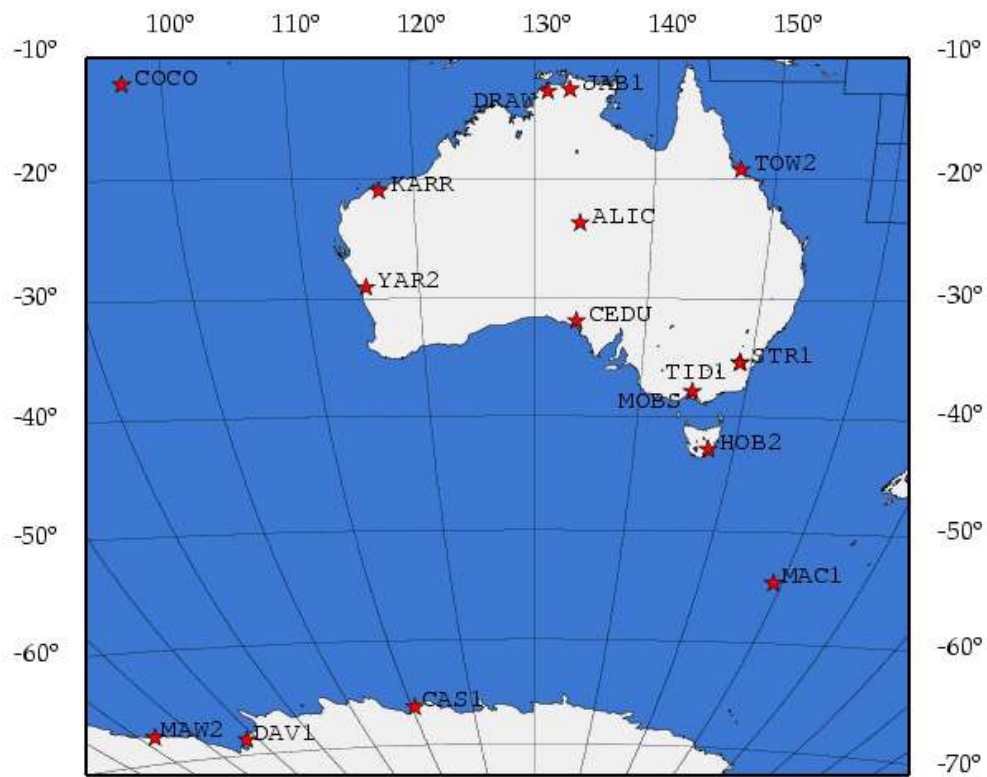


Figure 3.2 Australian Regional GPS Network (ARGN).

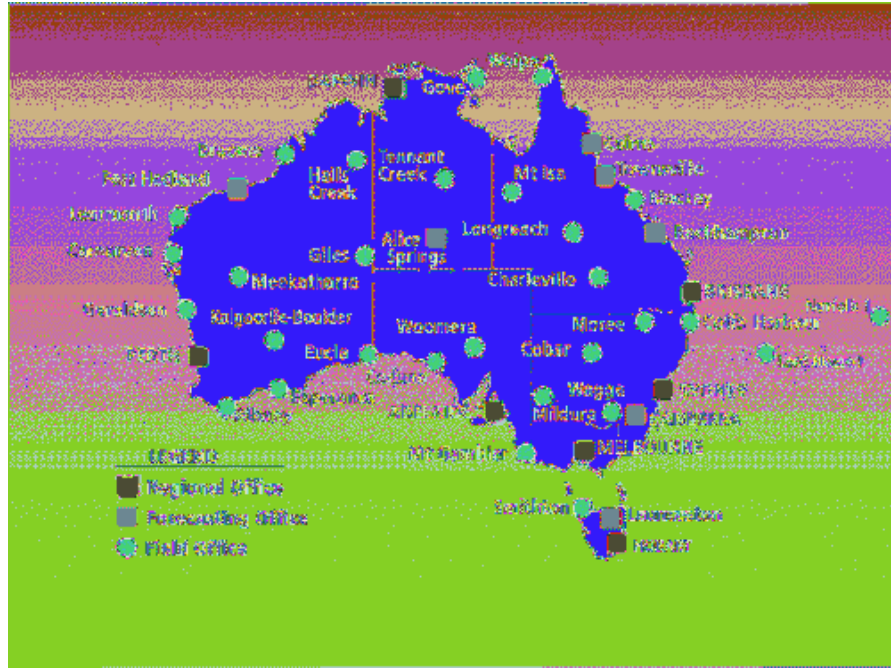


Figure 3.3 Locations of some Australian Upper Air Network (AUAN) stations.

3.5.2 Daily GPS Data Processing

GPS data were processed using the GAMIT software v10.07 [King, *et al*, 2001] with conventional 24-hour sessions, although the software is capable of handling a variable session length starting at an arbitrary time. The zenith tropospheric delays for each site were estimated every 30 minutes within each 24-hour session. In order to obtain high quality absolute ZTD estimates, the GPS data processing parameters were carefully configured. The main characteristics of GPS data processing are listed in Table 3.2. It is very important that tight enough constraints should be put on those parameters, such as orbits, EOP, and site positions, to the maximum extent of known confidence so that the zenith delays could be estimated reliably, since the tropospheric delay is strongly correlated with the site vertical component, which is in turn correlated with the GPS orbits, while the orbits are correlated with the EOP.

3.5.3 Computing PWV from GPS ZTD and Surface Meteorological Data

The GPS-PWV solutions are derived from GPS ZTD solutions and the zenith hydrostatic delays, which are computed from the surface meteorological data as

given by Equation (2.18). Ideally, the GPS antenna and surface meteorological sensor are placed in the same location, perhaps a few metres apart, so that the GPS-PWV measurements are physically referred to the vertical column water directly above the site. Again, to compare GPS-PWV solutions and radiosonde solutions, the GPS sites should be collocated with the radiosonde sites. However, in this experiment there are lateral and vertical separations between the GPS sites and radiosonde sites. As shown in Table 3.3, the GPS site at Darwin is located 53km away from the nearest radiosonde site.

Table 3.2 The main characteristics of GPS data processing.

Sampling rate	30 sec
Elevation angle	10 deg
Observable	Double differences
Phase centre correction	IGS model applied
Orbit, pole and UT	IGS
Station coordinates	Tightly constrained to the ITRF 2000
Ocean loading	Applied
Mapping function	Niell
Zenith delay a priori constraints	0.5m
Zenith delay model	0.5m
Zenith delay variation	0.01m/sqrt(hour) and 100 hours
ZTD estimation interval	30min

Table 3.3 Separation between ARGN GPS sites and AUAN Radiosonde sites.

Site	ΔN (km)	ΔE (km)	ΔH (m)	ΔS (km)
ALIC	-13.747	0.351	-41.506	14
COCO	-0.214	-0.071	-1.499	0.2
DARW	46.113	-26.762	-44.302	53
HOB2	-9.469	-9.025	5.691	13
TOW2	2.36	-29.987	-22.823	30
DAV1	0.013	-0.005	-10.314	10
MAC1	-0.018	1.045	-7.743	8
CAS1	0.457	0.703	1.908	2
MAW1	0.370	0.100	-21.055	21

Figure 3.4 illustrates the separation of the GPS site and the radiosonde site. Computation of GPS-PWV requires the temperature and pressure measurements at the GPS station level. However, the temperature and pressures provided by BOM are referred to the radiosonde station level and quasi-non-hydrostatic (QNH) level, respectively. The calculation to derive QNH pressure has been performed using the station level barometric pressure P_{QFE} . The station height

above mean sea level (H_{stn}) was also required.

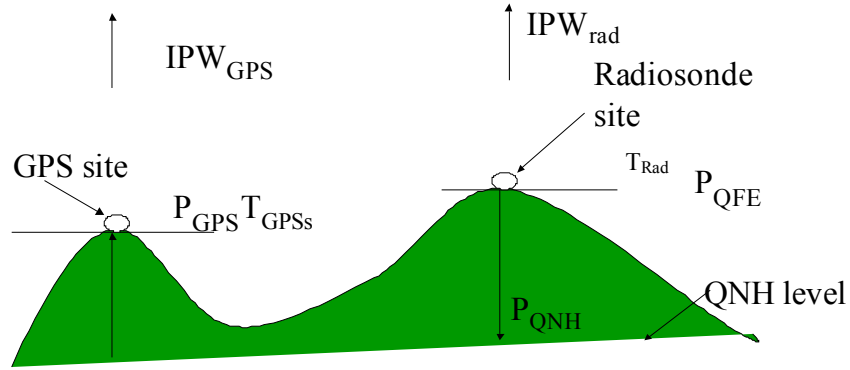


Figure 3.4 Reduction of T_{rad} and P_{QNH} to T_{GPS} and P_{GPS} , which is highly sensitive to the height difference between GPS and radiosonde sites.

The following equation from Bureau of Meteorology Specification A2669 Version 4.0 (Page 100) was applied:

$$P_{QNH} = P_0 \{ (P_{QFE} / P_0)^{Ru/g} + H_{stn} u / T_0 \}^{g/Ru} \quad (3.12)$$

where P_{QNH} is the QNH pressure in mbar, and P_0 is the standard pressure at mean sea level $P_0=1013.25$ mbar. P_{QFE} is the QFE pressure in mbar, $R = 287.04$ $m^2 / ^\circ C sec^2$, $u = 0.0065$ m / sec^2 , $g = 9.80655$ m / sec^2 , H_{stn} = station height in metres and $T_0 = 288.16^\circ K$.

We now need to reduce the temperature T_{rad} and QNH pressure P_{QNH} to the station level of GPS site: T_{GPS} and P_{GPS} .

Although theoretically we should consider the effects of both lateral separation and vertical difference on the temperature and pressure parameters, only the height difference is sensitive to temperature and pressure changes. The difference between T_{rad} and T_{gps} is approximated by the following equation:

$$\Delta T = \beta \cdot \Delta H \quad (3.13)$$

where $\beta = -6.5^\circ C/km$ is the temperature lapse rate. For the maximum height difference $\Delta H = -44.30m$ at the Darwin station, we can calculate ΔT to be about 0.29K, which has little contribution to the PWV solution errors. Therefore, the

temperature changes due to the height difference were not considered in this study. In other words, the temperature T_{rad} was substituted for T_{gps} in the data analysis.

The inverse of Equation (3.12) is:

$$P_{QFE} = P_0 \{ (P_{QNH} / P_0)^{R_u / g} - H_{stn} u / T_0 \}^{g / R_u} \quad (3.14)$$

To compute the P_{QFE} for the GPS site, we simply substitute H_{stn} with the height above mean sea level for the GPS site. For instance, given $P_{QNH}=1017.9$ mbar, $H_{stn}=650$ m at the radiosonde site and $H_{stn}=606$ m at the GPS site, we obtain: $P_{QFE}=941.93$ mbar and $P_{GPS}=946.92$ mbar respectively.

According to Equation (2.18), ZHD is more sensitive to pressure than to temperature. Reduction of P_{QFE} to P_{GPS} was carried out as an essential step in this analysis.

3.5.4 Experimental Results and Discussion

We estimated ZTD/PWV every 30 minutes using GPS tracking data of 24 hours duration from each GPS/Radiosonde collocated site. Figure 3.5 shows the RMS values of the PWV estimates over the 24-hour period. The RMS values reflect the ZTD/PWV estimation accuracy using the GAMIT software. We clearly observe that the “session” boundary affects the solutions: the ZTD/PWV estimates at two boundaries have the largest uncertainty. To demonstrate the accuracy of the PWV solutions, we can compare the two PWV solutions for the common data points at UTC 0h, which are derived from two different GPS data sets. Figure 3.6 shows the differences of the GPS-PWV estimates at the data point of UTC 0h for all five ARGN stations. We find that the standard deviation of these differences is 1.37mm. This implies that each estimate at UTC 0h would have an uncertainty of about 0.97mm. Taking the session boundary effect into account, we believe that the GPS-PWV estimate at UTC 2300h would have an accuracy of 1mm or better. This does not include the contributions to uncertainty due to the surface meteorological data.

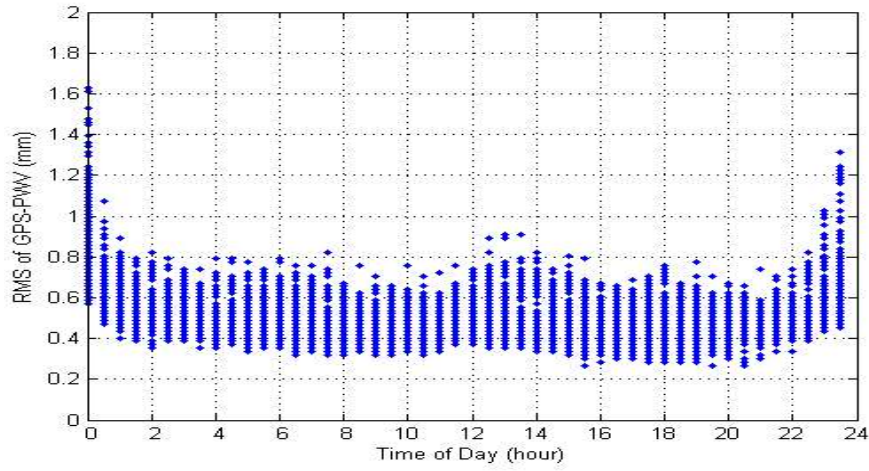


Figure 3.5 RMS of GPS-PWV estimates for 24 hours.

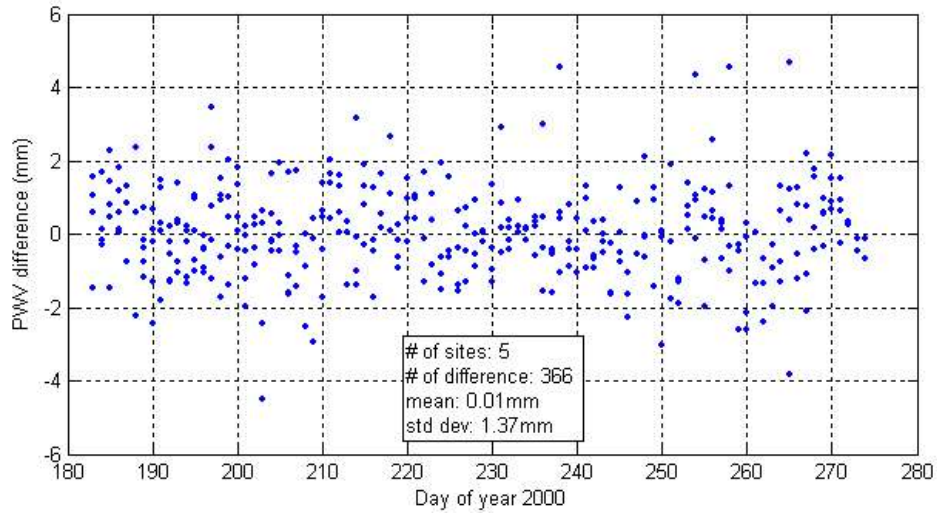


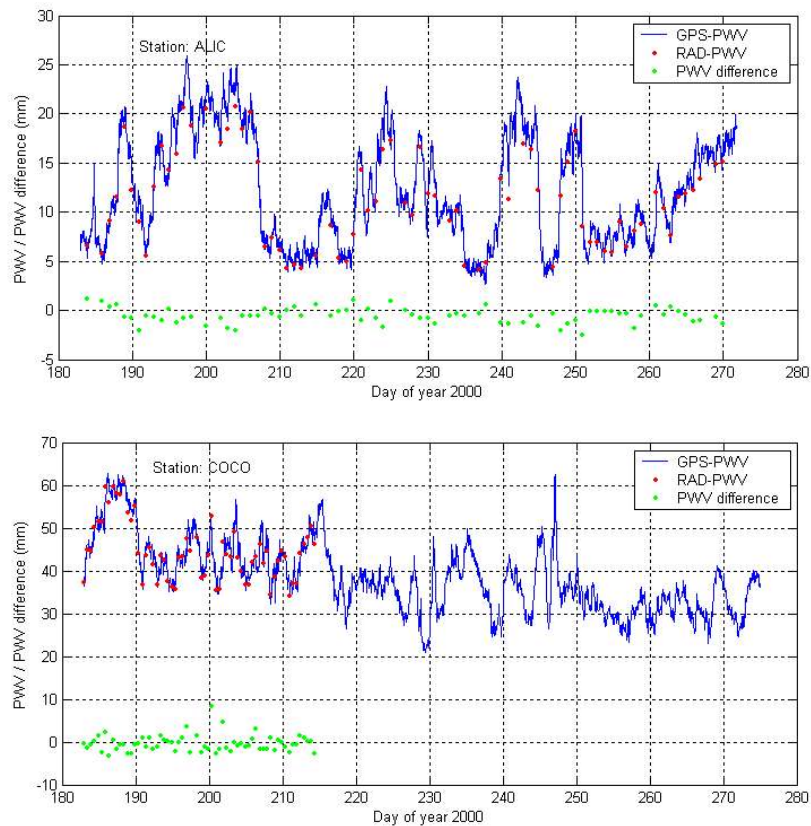
Figure 3.6 The differences of GPS-PWV estimates at UTC 0h for five ARGN stations.

We can also estimate PWV from radiosonde data that contains pressure, temperature and relative humidity profiles of all the atmospheric layers up to 30km above the site. As mentioned by other researchers, the accuracy of the radiosonde PWV observation is estimated of about 1.2mm [Liu, 2000]. This does not account for the precision of the numerical integration based on Equation (2.48). Theoretically, the denser the radiosonde samples along the path and the higher the balloon rises above the site, the more accurate the PWV approximation. In practice, the vertical distribution of water vapour varies from time to time, and from location to location. Denser radiosonde sampling may not provide accurate PWV estimates. Table 3.4 gives the average number of samples for each radiosonde site involved in this experimental study.

Table 3.4 Average number of radiosonde samples

site	ALIC	COCO	HOB2	TOW2	DARW
# of samples	74.3	111.6	72.5	101.2	90.3

We judge the performance of GPS-PWV estimates by comparison with the radiosonde PWV solutions. Figure 3.7 shows the GPS-PWV estimates (blue solid line) and Rad-PWV estimates (red dot), and their differences (green dot), for a 3-month period at the five ARGN sites. We have noticed that the GPS-PWV and Rad-PWV estimates agree well with each other. The half-hourly GPS PWV observations clearly resolve the many changes during periods of a few hours to 24 hours. Figure 3.8 demonstrates the agreement using a scatter-plot for all five sites, comparing the GPS-PWV solutions against the radiosonde estimates. The number of comparisons, the maximum, minimum and mean PWV differences and their standard deviation and RMS for the five stations, together with statistics of all 556 comparisons, are summarized in Table 3.5.



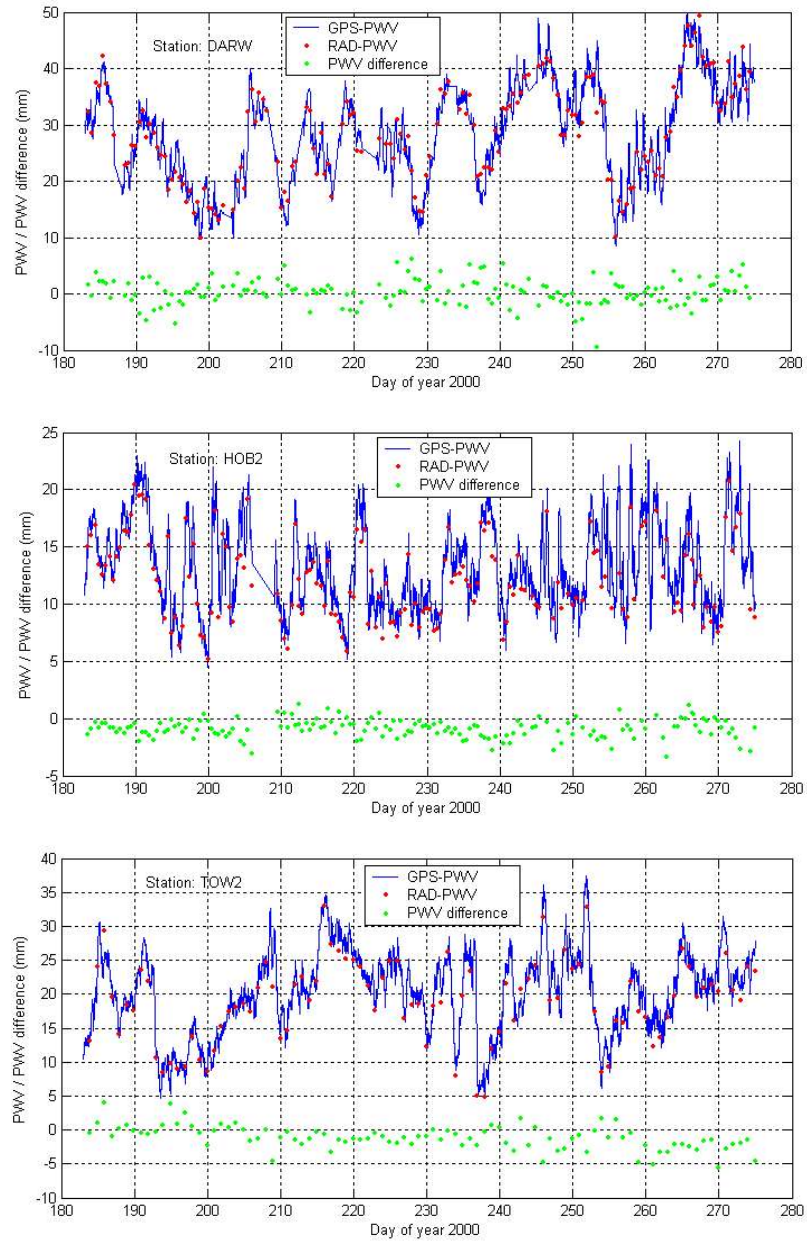


Figure 3.7 Comparison of GPS-PWV estimates (blue solid line) and Rad-PWV estimates (red dot) and their differences (green dot) for a 3-month period at the five ARGN sites: ALIC, COCO, DARW, HOB2 and TOW2.

Table 3.5 Comparison of GPS PWV estimate with radiosonde PWV estimates during a 3-month period at five ARGN sites: ALIC, COCO, DARW, HOB2 and TOW2.

	All	ALIC	COCO	DARW	HOB2	TOW2
# of Comparisons	556	74	63	163	164	92
Max (Rad-GPS)	8.34	1.14	8.34	6.20	1.27	3.96
Min (Rad-GPS)	-9.58	-2.47	-3.22	-9.58	-3.35	-5.62
Mean (Rad-GPS)	-0.51	-0.56	-0.39	0.23	-0.91	-1.15
Stddev (Rad-GPS)	1.76	0.78	1.95	2.36	0.81	1.74
RMS (Rad-GPS)	1.83	0.96	1.97	2.36	1.22	2.08

While the standard deviation values in Figure 3.8 and Table 3.5 are computed

relative to the mean of the difference between GPS-PWV and radiosonde PWV to show the dispersive errors of all the sites, the RMS values are computed relative to zero without bias removal, thus giving a total level of agreement. It can be seen that the GPS-PWV data agrees with radiosonde data for all five stations to within 1.83 mm. Better agreement is seen at ALIC and HOB2, while the worse agreement is at COCO, DARW and TOW2. In addition, there are negative biases for most of the stations. The largest bias is at TOW2, where the radiosonde PWV reports on average 1.15mm less than GPS-PWV. The source of these biases is uncertain, although the biases themselves are very small.

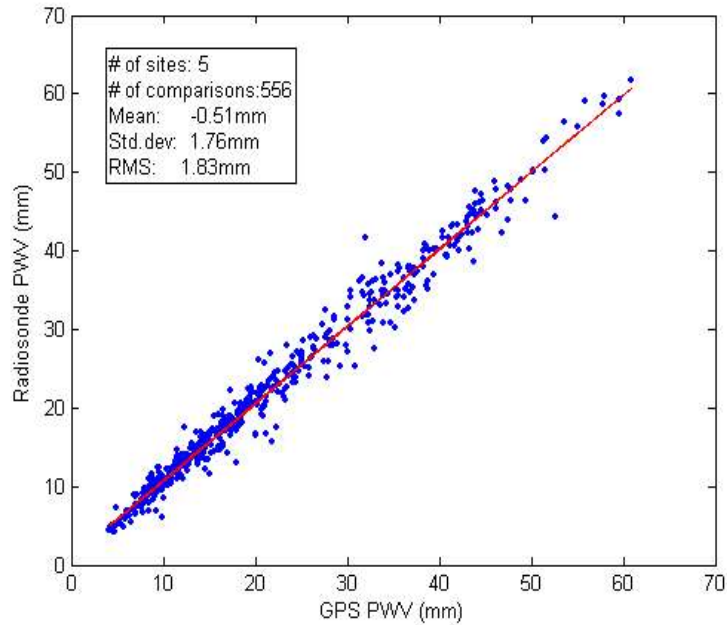


Figure 3.8 A scatter-plot for all the five sites comparing GPS-PWV estimates against the radiosonde PWV estimates.

3.5.5 Improving the Agreement

The GPW-PWV results based on the final IGS orbits theoretically would agree with the radiosonde to zero biases and standard deviation (std dev) to:

$$\sigma_{\Delta pwv} = \sqrt{\sigma_{GPS-PWV}^2 + \sigma_{Rad-PWV}^2} = \sqrt{1.0^2 + 1.2^2} = 1.56mm \quad (3.15)$$

The actual results in this experiment agree to within a mean of -0.51mm and a std dev of 1.76 mm, or a RMS of 1.83mm. This implies that the errors remaining in the GPS-PWV and/or the Rad-PWV results contribute a bias of the order of 0.5mm and an uncertainty of 1.76mm. Therefore we wish to explore the possible

sources of errors in order to improve the agreement or the accuracy of GPS-PWV solutions.

Firstly, we may question whether GPS-PWV estimates at the GPS sites can represent the GPS-PWV solutions at the radiosonde site because of the lateral separations of tens of kilometres, and height difference of tens of metres between the two sites. Water vapour measured in Alice Springs may be spatially less variable than Darwin, thus indicating a better RMS agreement for the PWV estimates. In other words, there could be a different disagreement in these stations in a different season, or at different locations. An opposite example is the Cocos Island site, where the GPS site and radiosonde site are about 200 metres apart, but the PWV estimate agrees only at the 1.97mm RMS level. Therefore, the separation is only one of the factors responsible for the lack of agreement between the results.

Secondly, we may argue that the weight mean temperature T_m used to derive PWV from ZTD in Equation (2.26) is in error. A recent water vapour study for the Hong Kong region has shown a significant effect of the T_m error on the PWV solutions [Liu, 2000]. Table 3.6 lists the average PWV estimate errors as a function of T_m errors of 3K and 5K for the five stations. We tested the T_m effect by comparing the GPS-PWV estimates with the T_m derived from a linear regression model (Equation 2.42), and from radiosonde data using Equation (2.24). Figure 3.9 shows T_m estimates from radiosondes against the T_m from the linear regression model (upper), and their difference (lower), for the experiment period. The error in T_m derived from the linear regression model is about 3.1K compared to the results from radiosondes, which may cause a 0.1-0.6mm error in the GPS derived PWV at the ARGN sites (according to Table 3.6). However, the improvement of the PWV results with radiosonde- T_m is not as significant as expected from the theory. The mean, maximum and minimum PWV differences between GPS-PWV and Rad-PWV for the five stations for all 556 comparisons, together with the standard deviation and RMS, are summarized in Table 3.7. The results using T_m from radiosonde data are almost the same as the previous one, which uses the T_m from the linear regression model. The standard deviation is only improved by 0.03mm.

Table 3.6 Average PWV estimate errors as a function of T_m errors of 3K and 5K for the five stations.

T_m error	Q Error	ALIC	HOB2	COCO	TOWN	DARW	Average
3 K	0.0022	0.16	0.18	0.57	0.29	0.39	0.29
5 K	0.0032	0.24	0.26	0.82	0.42	0.56	0.46

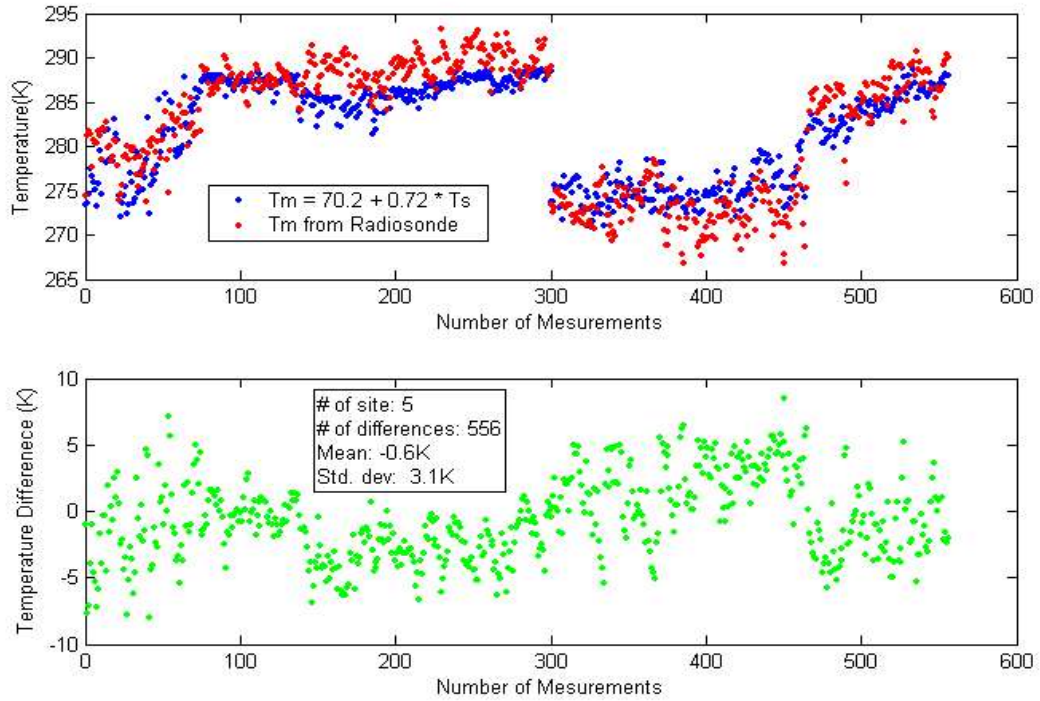


Figure 3.9 T_m estimates (upper) and their difference (lower) from radiosonde data and linear regression models.

Table 3.7 Comparison of GPS PWV estimates with radiosonde PWV estimates during a 3-month period, where one GPS-PWV estimate uses T_m from Linear Regression Model and the other uses T_m from Radiosonde data. A total of 556 comparisons are included in the mean, standard deviation, root mean squares (mm).

	RMS	Std dev	Mean	Max	Min
$T_m = 70.2 + 0.72 T_s$	1.8323	1.7615	-0.5098	8.3394	-9.5777
T_m from Radiosonde	1.8214	1.7336	-0.5633	8.4514	-9.6795

Thirdly, we could take into account the quality of the surface meteorological data themselves and the possible loss of accuracy when the surface temperature and QNH pressure for the radiosonde site were reduced to the GPS station level. The error in pressure measurements can be related to the PWV estimate error:

$$\sigma_{PWV} \approx 0.4 \cdot \sigma_p \quad (3.16)$$

where σ_{PWV} is the error in PWV in units of mm, and σ_p is the pressure error in

mbar. Thus to keep the contribution of the pressure error below 0.1mm PWV, the total pressure error should be less than 0.25mbar. According to a research report by the Bureau of Meteorological Research Centre, we can conclude that the typical RMS error of pressure falls in a range of less than 0.5mbar. Therefore, the total pressure error should be less than 0.2mm for PWV.

Finally, the PWV estimation errors may also contain errors contributed from the Saastamoinen ZHD model, and the effects of ground station coordinates. Further investigation into these possible sources of errors should be conducted.

3.5.6 Summary

The research efforts on GPS water vapour estimation using data from the ARGN network has led to the establishment of the technical capability of GPS-PWV estimation on a daily basis. GPS data from the ARGN network were collected and processed daily, and GPS-PWV solutions were produced when surface meteorological data were also available. We have developed a package of software tools and scripts for the computation of GPS-PWV estimation, Rad-PWV estimation, weighted mean temperature estimation and PWV solution analysis, etc. We have used the data from the ARGN sites and five collocated radiosonde sites during a 3-month period for these experimental studies. The results have shown that:

- GPS-PWV estimation accuracy of 1mm was achieved
- GPS-PWV estimates agree with the Rad-PWV solutions with a mean difference of -0.51 mm and a RMS of 1.83mm.

The agreement perhaps is slightly worse than the theoretical 1.56mm RMS. However, because the quoted results were obtained under circumstances where the GPS and Radiosonde/surface meteorological data sites were located tens of kilometres apart, this level of agreement is considered reasonable. The experimental study has also shown a possible way to develop GPS Meteorology and applications with the existing meteorological data network, instead of requiring new meteorological sensors. This could save significant costs in installation of GPS-Met sensors. This issue will be further addressed in Chapter 4.

Chapter 4

GPS Water Vapour Estimation Using Interpolated Surface Meteorological Data from Australian Automatic Weather Stations

4.1 Introduction

To estimate atmospheric water vapour from GPS data, surface meteorological observations collected at the GPS sites are required. Ideally a dedicated meteorological sensor is installed adjacent to the GPS antenna. However, this involves additional cost of the order of one-third or half of the cost of a geodetic GPS receiver. To take advantage of existing GPS tracking networks and individual stations which are established and operated primarily for surveying, geodesy and navigation applications, it is necessary to seek alternative solutions, which either obviate the need for surface meteorological data, or use surface meteorological data from other sources instead.

In the region of Australia, there are currently over 30 permanent GPS reference stations providing hourly data from the tracking networks operated by Geoscience Australia (ARGN) and Land Victoria (GPSnet), which can be used to generate hourly GPS zenith total delay (ZTD) parameters. But hourly estimation of precipitable water vapour (PWV) also requires surface meteorological measurements. This research effort is focused on taking advantage of surface temperature and pressure data from the Australian Automatic Weather Station (AWS) network operated by the Bureau of Meteorology (BOM). The AWS network currently consists of over 1600 land sites all over Australia, of which about 400 sites provide hourly temperature and pressure observations (<http://www.bom.gov.au>).

While some of the GPS sites are collocated with the AWS stations and radiosonde stations of the Australian Upper-Air Network, many others are located within the proximity of a number of weather stations. To be able to make use of the hourly

surface meteorological data from the AWS network to determine GPS-PWV, we first need to assess the accuracy of interpolated temperature and pressure or derived zenith total delay (ZTD) with meteorological observations from a local or regional AWS network. Secondly, we should verify these GPS-PWV measurements against radiosonde PWV results for some stations in order to investigate the consistency between the GPS-PWV solutions and the external PWV solutions, such as radiosonde PWV solutions. In this chapter, we present a case study using 36 AWS sites in Victoria and New South Wales to investigate the first problem, and compare the GPS and radiosonde PWV results for Alice Spring, Darwin, Hobart and Townsville stations to demonstrate a solution to the second problem. The chapter is concluded with a summary of the research findings.

4.2 Accuracy Requirements for Surface Meteorological Data

As discussed in the previous chapters, the zenith total delay (ZTD) estimate consists of the zenith wet delay (ZWD) and the zenith hydrostatic (dry) delay (ZHD):

$$ZTD = ZWD + ZHD \quad (4.1)$$

ZHD can be calculated easily from surface meteorological observations using empirical models that have been developed for this purpose. Here we consider three common models: Saastamoinen (SAAS) [Saastamoinen, 1973], Hopfield [Hopfield, 1971] and Black [Black, 1978], which have been described in Chapter 2:

$$d_s^z = 0.2277 \cdot \frac{P}{F(\varphi, H)} \quad (4.2)$$

$$F(\varphi, H) \equiv 1 - 0.0026 \cdot \cos(2\varphi) - 0.00028 \cdot H$$

$$d_h^z = 1.552 \cdot (h - H) \cdot \frac{P}{T} \quad (4.3)$$

$$h \equiv 40.082 + 0.14898 \cdot (T - 273.16)$$

$$d_b^z = 0.2343 \cdot (T - 4.12) \cdot \frac{P}{T} \quad (4.4)$$

where φ is the latitude of the station in radians, H is the station height above mean sea level in km, P is the surface air pressure in mbar, T is the absolute temperature in Kelvin, and h is the height of the tropopause in km. The subscripts

S, H and B denote the ZHD computed with the SAAS, Hopfield, and Black models respectively.

After ZHD is obtained, subtracting ZHD from ZTD, we have:

$$ZWD = ZTD - ZHD \quad (4.5)$$

ZWD can then be converted to PWV using:

$$PWV = \Pi(T_m)ZWD \quad (4.6)$$

where $\Pi(T_m)$ is a dimensionless quantity given by the mean weighted temperature of the atmosphere.

Equations (4.2) to (4.4) show that all the above ZHD models require surface meteorological measurements, including air pressure and temperature. Hence errors in surface meteorological data affect the ZHD estimates, and ultimately the ZWD and PWV estimates. In order to ensure millimetre accuracy for the PWV, we first consider the admissible error in the surface meteorological measurements.

4.2.1 Influence of Pressure Error

Assuming that T is accurately known in Equations (4.2) to (4.4), then the impact of the uncertainty in the pressure measurement P on the ZHD can be evaluated using the law of error propagation for all the above models[Liu, 2000]:

$$\sigma_{d_s} = \frac{0.2277}{F(\phi, H)} \cdot \sigma_P \quad (4.7)$$

$$\sigma_{d_H} = (0.2312 - \frac{0.9520 + 1.552 \cdot H}{T}) \cdot \sigma_P \quad (4.8)$$

$$\sigma_{d_B} = (0.2343 - \frac{0.9653}{T}) \cdot \sigma_P \quad (4.9)$$

In the above relationships, a large error in pressure produces a large effect on the ZHD. This will be the case when ϕ is minimum and H is maximum in Equation (4.7), H is minimum and T is maximum in Equation (4.8), and T is maximum in Equation (4.9). Now, if we use $\phi=0^\circ$ and H=5km in Equation (4.7), and H=0km and T=333.16K in Equation (4.8) and (4.9), we obtain:

$$\sigma_{d_s} = 0.2286 \cdot \sigma_P \quad (4.10)$$

$$\sigma_{d_H} = 0.2283 \cdot \sigma_P \quad (4.11)$$

$$\sigma_{d_B} = 0.2314 \cdot \sigma_P \quad (4.12)$$

where σ_d is in cm and σ_P is in mbar.

In order to ensure millimetre-level accuracy for the PWV, the contribution of pressure error to ZHD estimates should be small enough to be neglected (compared to other error sources). Table 4.1 shows the influence of pressure error on the GPS-PWV estimate, whose standard accuracy is 1mm. Assuming that the ZHD error to be 1mm, it leads to a PWV estimate error of 0.15mm. This contribution is not significant compared to the total GPS-PWV estimate accuracy of 1mm. From Table 4.1 we see that if the pressure measurement is accurate to 0.4mbar or better, the contribution to the PWV error increase is about 1%, which is negligible. To keep the pressure error contribution within 5% and 10%, the pressure error must be less than 0.80mbar and 1.20mbar respectively.

Table 4.1 Influence of pressure error on PWV estimate.

Pressure Error (mbar)	ZHD Error (mm)	PWV error (mm)	Total PWV error (mm)
0.40	0.92	0.15	1.01
0.80	1.84	0.30	1.04
1.20	2.76	0.45	1.10
2.00	4.60	0.75	1.25
3.00	6.90	1.125	1.51

4.2.2 Influence of the Temperature Error

Assuming that pressure P is accurately known, the effects of the uncertainty in temperature measurement on the calculated ZHD for the above models is given by:

$$\sigma_{d_s} = 0 \quad (4.13)$$

$$\sigma_{d_H} = (1.552 \cdot H + 0.9520) \cdot \frac{P}{T^2} \cdot \sigma_T \quad (4.14)$$

$$\sigma_{d_B} = \frac{0.9653 \cdot P}{T^2} \cdot \sigma_T \quad (4.15)$$

Obviously the ZHD is independent of temperature for the SAAS model. As before, we fix H, P and T to their extreme values to see the maximum effect of the temperature error on the ZHD. Again for T=223.16K, P=1200mbar and H=5km

we obtain:

$$\sigma_{d_H} = 0.2099 \cdot \sigma_T \quad (4.16)$$

$$\sigma_{d_B} = 0.0233 \cdot \sigma_T \quad (4.17)$$

Because the temperature is not a variable in the SAAS model, its error will not affect the computed ZHD, but the Hopfield and Black models are influenced by this error. Once again, in order to ensure millimetre-level accuracy in the derived ZHD estimates, we should have the temperature precision better than 0.5K in the Hopfield model and 5K in the Black model.

4.3 Description of Surface Meteorological Data and Interpolation Procedures

As indicated in Figure 1.4, there are currently more than 30 continuously operating GPS stations providing hourly data files for GPS Meteorology research in Australia, which includes 14 stations of the ARGN, and 22 stations (15 operating sites and 7 proposed sites) in the Victorian GPSnet. Figure 4.12 shows the distribution of about 400 hourly updated weather observation stations all over Australia (left), including about 60 sites in Victoria (as shown in the right side of the figure). From these two figures, it can be seen that whilst many GPS sites in GPSnet are located close the AWS sites; others are located within close proximity of a number of weather stations. Therefore we can either use the meteorological data collected hourly at the closest site for PWV estimation, or use interpolated measurements instead. A method is needed to interpolate the temperature and pressure at the GPS site from the measurements made at the surrounding AWS sites. Because the vertical variability of pressure is dependent on the altitude of the station, the pressure and temperature measurements at different altitudes have to be converted to a common reference level, which is often the Mean Sea Level. As a result, the interpolated parameters at any point refer to this reference level. These parameters must then be converted to the station level of the GPS station in order to generate the PWV measurements for that station. In the following discussion, we first establish the relationships between the meteorological parameters at different levels.

geodetic texts and references. *Jarvis and Stuart* [2001] suggest the Ordinary Kriging (OK), also known as Punctual Kriging [*Dorsel and LaBreche*, 1997]. Our analysis has shown that the OK method provides optimal interpolation results for surface meteorological measurements [*Bai, et al*, 2002].

OK gives each sample point a weight (w). The weights are calculated using a variogram. Several variograms were suggested by *Wackernagel* [1998]. Three types of variograms were tested in this research effort:

- Linear variogram
- Exponential variogram
- Spherical variogram

All variograms are based on spherical distances d_{ij} between points i and j . This distance can be calculated using the geodetic coordinates of the points.

Linear variogram

The linear variogram only depends on the distance between points. If the distance increases, the covariance increases. A maximum range a can be used to set a limit to the distance that vanishes the covariance [*Wackernagel*, 1998]. The values γ_{ij} are calculated as follows:

$$\gamma_{ij} = \begin{cases} \frac{d_{ij}}{a} & , \text{ for } a \leq d_{ij} \\ 1 & , \text{ for } a > d_{ij} \end{cases} \quad (4.20)$$

Exponential variogram

The exponential variogram model falls off exponentially with increasing distance according to the relation:

$$\gamma_{ij} = 1 - e^{-\frac{d_{ij}}{a}} \quad (4.21)$$

where the parameter $a(\neq 0)$ determines how quickly the covariance falls off.

Spherical variogram

The spherical variogram is a commonly used model [Wackernagel, 1998]. As for the linear method, the spherical method also uses a range a to constrain the increase of the variogram values. The variogram is calculated as follows:

$$\gamma_{ij} = \begin{cases} 1 - \frac{3}{2} \frac{d_{ij}}{a} + \frac{1}{2} \frac{d_{ij}^3}{a^3} & , \text{ for } a \leq d_{ij} \\ 1 & , \text{ for } a > d_{ij} \end{cases} \quad (4.22)$$

Figure 4.2 show the above variograms, with $a=1000$ and $a=1500$. When the variogram is calculated, the weights can be calculated for the sample points:

$$w = A^{-1}B ; A = \begin{pmatrix} \gamma_{11} & \gamma_{21} & \cdots & \gamma_{1n} & 1 \\ \gamma_{12} & \gamma_{22} & \cdots & \gamma_{2n} & 1 \\ \vdots & \vdots & \ddots & \vdots & 1 \\ \gamma_{1n} & \gamma_{2n} & \cdots & \gamma_{nn} & 1 \\ 1 & 1 & \cdots & 1 & 0 \end{pmatrix}, B = \begin{pmatrix} \gamma_{1i} \\ \gamma_{2i} \\ \vdots \\ \gamma_{ni} \\ 1 \end{pmatrix} \quad (4.23)$$

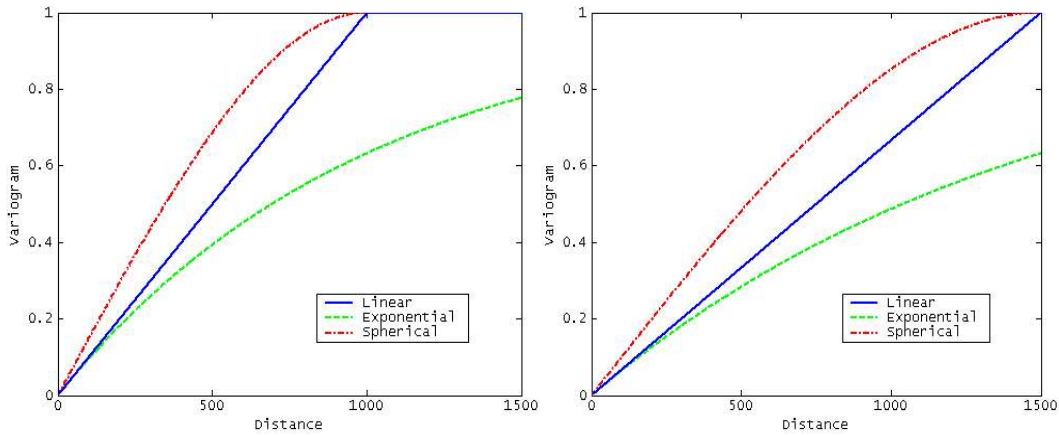


Figure 4.2 Different variograms for the Ordinary Kriging method. The maximum range a is set to 1000km (left) and 1500km (right) respectively.

With the weights determined, the value at a point i can be calculated from the known values (K) at the sample points:

$$V_i = wK \quad (4.24)$$

4.4 Interpolation Results with a Local AWS Network

Figure 4.3 shows the network of 36 hourly updated AWS sites, covering the area between 33°S and 38°S and between 140°E and 150°E in Australia. For each station the data file contains the station name, latitude and longitude in degrees,

day and time of recording data, temperature in °C, relative humidity in %, MSL or QNH pressure in mbar etc. The observations are updated every hour and acquired for use without being quality controlled. A total of 45 hourly data points were collected for this experimental study.

To evaluate the interpolation results, we compare the interpolated pressure and temperature for each point using all other data points in the network, against the observed ones. Experimental results have shown that interpolation using linear variograms provides the optimal interpolation results in terms of overall standard deviation and RMS values. These values are computed from the differences between interpolated and observed pressure and temperature. Figure 4.4 shows the overall standard deviation (STD) and mean errors over the 33 data points against time, excluding the three outlying data points.

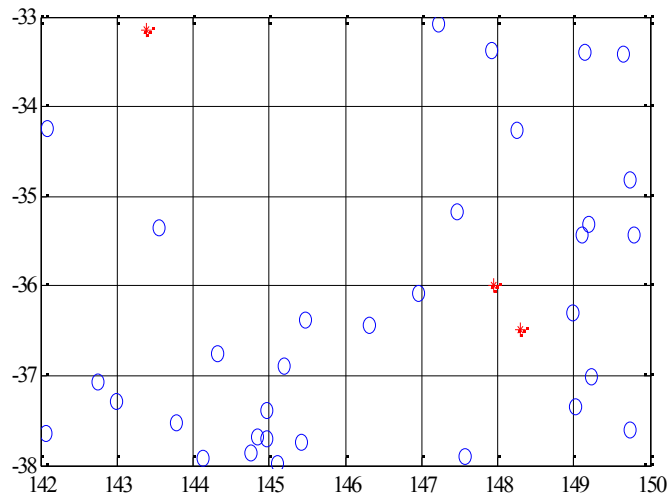


Figure 4.3 The network of 36 hourly updated AWS sites, covering the area between 33°S and 38° S and between 140°E and 150°E in Australia. Asterisks indicate outlying points.

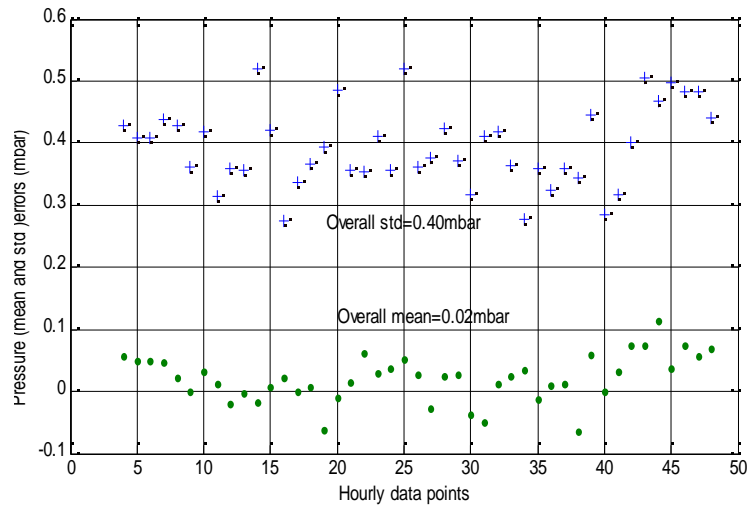


Figure 4.4 Interpolated pressures standard deviation (STD) and mean values over the 33 data points against time, excluding three outlying data points.

Table 4.2 summarizes the statistics of these errors and lists the predicted ZHD and PWV errors, resulting from interpolated pressure errors. It is observed that for this particular AWS network, the overall interpolated pressure accuracy is about 0.40mbar, which leads to a PWV estimation accuracy of 0.15mm. This contribution is not significant, compared to the total GPS-PWV estimated accuracy of 1.0mm. In conclusion, the hourly surface meteorological measurements can be used for GPS meteorological applications, if the quality control issues can be addressed.

Table 4.2 Summary of interpolated pressure errors and predicted ZHD and PWV errors.

	Interpolated pressure errors (mbar)	Predicted ZHD error (mm)	Predicted PWV error (mm)
Min	-1.35	-3.2	-0.49
Max	1.96	4.5	0.69
Mean	0.02	0.05	0.01
Std	0.40	0.92	0.15
RMS	0.40	0.92	0.15

4.5. GPS Water Vapour Experiments and Results

4.5.1 Experimental Description

The objective of presenting GPS water vapour experimental results from an Australian network is to assess the overall consistency of GPS-PWV compared to radiosonde PWV solutions for closely located stations where surface meteorological measurements for GPS sites can be interpolated from the surrounding AWS sites.

We collected GPS tracking data on a daily basis from the fifteen ARGN stations operated by Geosciences Australia. The GPS tracking data were collected at a rate of 30 seconds. This network operates primarily for geodetic and geodynamic purposes, and does not provide surface meteorological data. The 45 days of data (from 13 May to 30 June 2002) were processed. The radiosonde data at Alice Springs, Darwin, Townsville and Hobart were collected for the same period from the Australian BOM. Radiosondes were released once or twice daily at about UTC 23:00 or 15:00 from the four sites. For each of the GPS/radiosonde sites, surrounding AWS sites recording temperature (T) and pressure (P) hourly were used to interpolate the T and P for the GPS site. We only estimated GPS zenith tropospheric delays with GAMIT software every 30min to match the radiosonde release times and the 60min meteorological data interval. The separations between the GPS and radiosonde sites are given in Table 3.3. The GPS data was processed using the same strategies described in Section 3.5.2.

As we have discussed previously, there is a need to interpolate the T and P at mean sea level, and then compute the T and P at the station level of the GPS sites.

4.5.2 Experimental Results and Discussion

We estimated ZTD every 30min using tracking data of 24-hour session length from all the GPS sites. Then we used two sets of meteorological measurements to compute ZHD. One set is extracted from the closest AWS site. The other set is the interpolated result from the surrounding AWS sites. We also estimated PWV from radiosonde data (pressure, temperature and relative humidity profiles of all the layers above the site). Figure 4.5 shows the GPS-PWV estimates against Rad-PWV estimates at the Alice Springs, Darwin, Hobart and Townsville sites. Figure 4.6 shows the scatter-plot for all four sites. The maximum, minimum, difference

between GPS-PWV and Rad-PWV, and their standard deviation and RMS values, for all four stations are summarized in Table 4.3. We have noticed that all 195 comparisons between GPS-PWV and Rad-PWV estimates are bounded in the range of $\pm 6\text{mm}$, with a RMS of 1.74mm . We therefore are confident that the GPS-PWV and Rad-PWV estimates agree with each other very well.

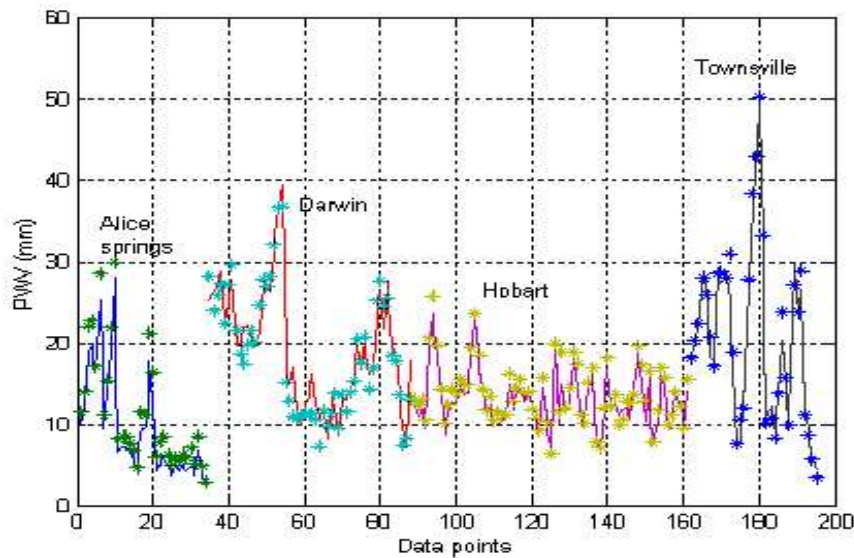


Figure 4.5 GPS-PWV estimates against Rad-PWV estimates at Alice Springs, Darwin, Hobart and Townsville stations.

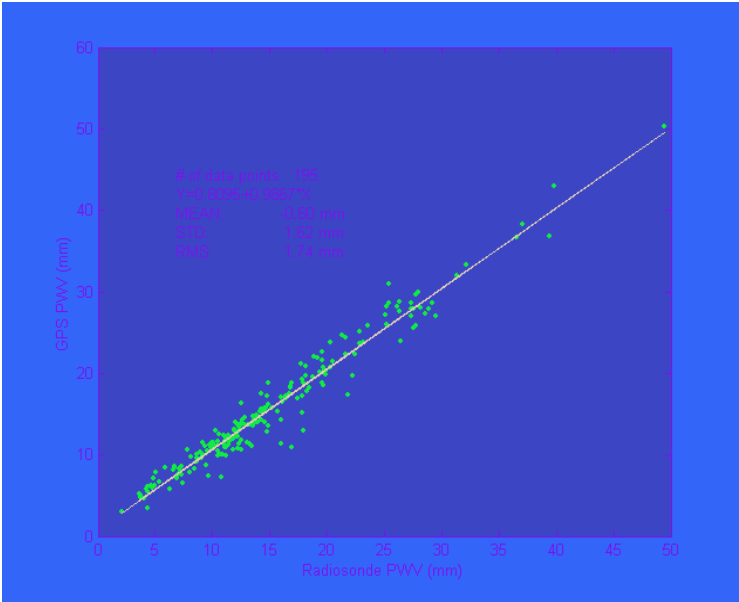


Figure 4.6 A scatter-plot for all four sites comparing GPS-PWV solutions against the radiosonde estimates, with interpolated T and P.

Table 4.3 Overall consistency of GPS PWV with interpolated T and P and Radiosonde PWV.

	Ordinary Kriging Interpolated T &P(mm)
Max (GPS- Rad)	5.60
Min (GPS- Rad)	-5.93
Mean (Rad-GPS)	-0.60
Std. dev (Rad-GPS)	1.65
RMS (Rad-GPS)	1.74

4.6. Summary

This chapter has experimentally demonstrated the feasibility of using hourly surface temperature and pressure observations from the Australian Automatic Weather Stations (AWS) network for GPS water vapour estimation. Data analysis with 36 data points from the Victorian region has demonstrated that the Ordinary Kriging method with linear variograms can be used for pressure interpolation, resulting in an overall standard deviation of 0.40mbar in pressure, or 0.15mm in PWV estimation.

We have used the data from four GPS sites and collocated radiosonde sites during the period from 13 May to 30 June 2002 for the studies. The results have shown that GPS-PWV estimates agree with the Rad-PWV solutions at an average mean difference of 0.604mm and RMS of 1.74mm. The agreement is perhaps slightly worse than the theoretical RMS of 1.56mm. However, the quoted results were obtained under circumstances where the radiosonde and AWS data sites were located tens of kilometres apart, and the quality of the pressure measurement was unknown. The experimental results indicate a possible way to develop GPS Meteorology and applications using the existing meteorological data network. This could save significant costs associated with the installation of meteorological sensors.

Chapter 5

Measuring Ocean Loading and Its Effects on GPS Derived Precipitable Water Vapour

5.1. Introduction

The periodic motion of the Earth's surface due to the forcing from ocean tides, referred to as ocean loading, is the second largest periodic motion of the Earth's crust after the solid Earth tides in areas with energetic ocean tides, such as the Australia coast and islands. Their frequency content is dominated by semi-diurnal (M2, S2, N2 and K2) and diurnal (O1, K1, P1 and Q1) constituents. The amplitude of the Earth's surface motion due to ocean loading can reach several centimetres in the vertical component and one-tenth to one-third of this in the horizontal component in coastal regions. Such displacements are normally not taken into account when the accuracy of the application is of the order of several tens of centimetres. But for applications which require centimetre or millimetre level accuracy, such as precise geodetic positioning and GPS Meteorology, it is important to estimate the ocean loading effects and apply an ocean loading correction to the GPS measurements, especially in coastal areas.

As shown in Figure 3.2, most of the Australian Regional GPS Network (ARGN) sites are located along the coast and on islands. However, very little effort has been made to quantify the effects of ocean loading on GPS-derived solutions at these ARGN sites. This chapter presents the GPS experimental results using data from the ARGN network, focusing on the ocean loading and its effects on GPS-derived precipitable water vapour estimates.

5.2 Ocean Loading Models and Effects on Australian ARGN Sites

Ocean loading is usually described by the convolution of a surface load derived from a barotropic ocean tide model, using the Green function describing the elastic response of the Earth's crust to that load (see e.g. *Farrell, 1972*;

Scherneck, 1991; *Agnew*, 1997). Ocean load tide L is given by a global integral (assumed spherical):

$$L(\varphi', \lambda') = \rho \int_0^{2\pi} \int_0^\pi H(\varphi, \lambda) G(\theta, A) R^2 \sin \varphi d\lambda d\varphi \quad (5.1)$$

where ρ is the ocean water density, H is the ocean tidal height in complex value for a given tidal constituent, (φ', λ') and (φ, λ) are the spherical coordinates of the estimation point and the loading point respectively; A is the azimuthal angle from the former to the latter; θ is the angular distance which can be obtained from the trigonometric formula $\cos \theta = \sin \varphi \sin \varphi' + \cos \varphi \cos \varphi' \cos(\lambda - \lambda')$; R is the radius of the spherical Earth model and $G(\theta, A)$ is the mass-loading Green's function of interest (displacements, gravity, tilt, strain, and deflection of the vertical).

There are two commonly used Green's functions, one is given by *Farrell* [1972] based on the Gutenberg-Bullen A Earth model, and the other is given by *Endo and Okubo* [*Matsumoto, et al*, 2001] based on the 1066A Earth model. The Green's functions for ocean loading displacement on the Earth's surface in the radial and horizontal directions have the following expressions:

$$G_{rad} = \frac{R}{M_e} \sum_{n=0}^{\infty} h'_n P_n(\cos \theta) \quad (5.2a)$$

$$G_{hor} = \frac{R}{M_e} \sum_{n=1}^{\infty} l'_n \frac{\partial P_n(\cos \theta)}{\partial \theta} \quad (5.2b)$$

where M_e and R are the mass and radius of the spherical Earth model, h'_n and l'_n are the loading Love numbers of order n (whose values may be found from the model of Earth's internal structure) and P_n is the Legendre function of degree n .

To calculate ocean loading displacements, an accurate ocean tide model is required. Examples of global ocean tidal models include the Schwiderski model [*Schwiderski*, 1980], the CSR 3.0 model [*Eanes*, 1994], the TPXO.2 model [*Egbert et al*, 1994], and the FES95.2 model [*Le Provost et al*, 1994, 1995]. A brief description of the available ocean tide models are listed as follows:

- (a) The *Schwiderski* model is the oldest [*Schwiderski* 1980] model and has been used as a standard ocean tide model until the mid of 1990's. It is a hydrodynamic model, defined by a 1 by 1 degree grid, and uses an

interpolation scheme to derive values of the tide gauges.

- (b) NAO.99b [*Matsumoto et al.*, 2000] is based on the same hydrodynamics as the Schwiderski model but has TOPEX/Poseidon satellite data assimilated into it, and is defined by a 0.5 by 0.5 degree grid.
- (c) FES94.1 is a purely hydrodynamic tide model tuned to fit tide gauge data globally. It has been calculated on a finite element grid with very fine resolution near the coast, and defined by a 0.5 by 0.5 degree grid. In FES95.2, the tides in the Arctic were improved and TOPEX/Poseidon satellite data has been used to adjust the long wavelength behaviour of FES94.1. FES98 is again a purely hydrodynamic model that has assimilated a set of about 700 carefully selected tide gauge data into it. Another improvement is the fact that it has been computed on a global grid (instead of computing the ocean tides in a few ocean basins separately and then gluing the solutions together). FES99 is an update of FES98 and has TOPEX/Poseidon satellite data assimilated into it. Both FES98 and FES99 are defined by a 0.25 by 0.25 degree grid.
- (d) CSR3.0 and CSR4.0 are long wavelength adjustments of FES94.1 using TOPEX/Poseidon satellite data and are defined by a 0.5 by 0.5 degree grid. For the tidal values below and above the 66S and 66N latitude bands (the limits of the TOPEX/Poseidon satellite), these models become equivalent to FES94.1.
- (e) GOT99.2b and GOT00.2 are also long wavelength adjustments of the FES94.1 model using TOPEX/Poseidon satellite data and are defined by a 0.5 by 0.5 degree grid. GOT99.2b also becomes equivalent to FES94.1 outside the 66 degree latitude bands. GOT00.2 is different from FES94.1 in the polar region because ERS1/2 data is used in the assimilation process.
- (f) TPXO.5 has been computed using inverse theory, using tide gauge and TOPEX/Poseidon satellite data. It finds the optimum balance between observations and hydrodynamics. It is also defined by a 0.5 by 0.5 degree grid.

These ocean tide models agree well with each other and with observations over most of the open oceans (see e.g. *Shum et al.*, 1997). For the Australian region, we

have compared the Schwiderski model, the CSR 4.0 model, the GOT99.2b model and the NAO.99b model. We computed the eight principal diurnal and semi-diurnal constituents (K1, O1, P1, Q1, M2, S2, N2, and K2) for all the ARGN stations (see Appendix C for details). The standard deviation (std), maximum (max) and mean difference (mean) of the amplitude and phase of the eight ocean tide constituents are listed in Table 5.1. The amplitudes agree well, with the difference being about 0.2mm, while the phase difference reaches about 8 degrees. Figure 5.1 shows the vertical displacement on June 1, 2000 at ARGN site COCO, which has the largest ocean loading effects. The CSR 4.0 model, the GOT99.2b model and the NAO.99b model agree better than the Schwiderski model, but the maximum difference of the vertical displacements between the above four models is still less than 1mm, so any one of these models can be used in the Australian region.

Table 5.1 Differences between the ocean tide models.

	Amplitude (mm)			Phase (degree)		
	Std.	Max	Mean	Std.	Max	Mean
OSO – CSR	0.23	3.31	-0.028	8.86	60.20	-0.48
GOT – CSR	0.17	2.33	0.034	8.26	102.60	-0.95
NAO - CSR	0.19	1.49	0.036	6.06	62.30	-0.26

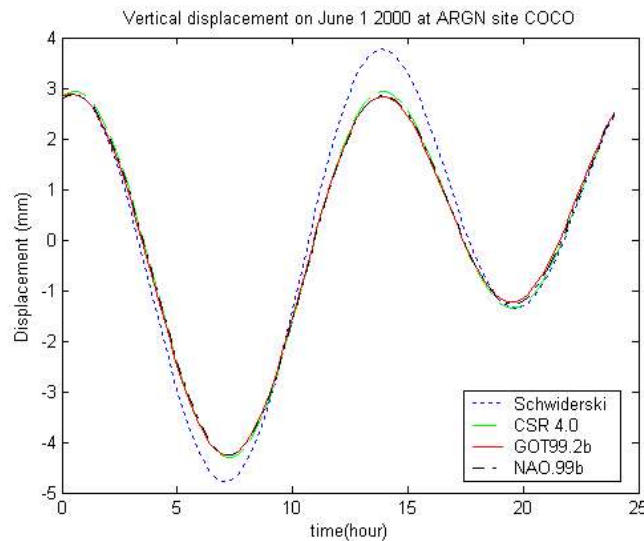


Figure 5.1 Vertical displacements on June 1 2000 at ARGN site COCO.

Figures 5.2a and 5.2b show the predicted displacements on June 1, 2000 using the CSR4.0 ocean tide model with eight principal diurnal and semi-diurnal constituents (K1, O1, P1, Q1, M2, S2, N2, K2) at the ARGN sites ALIC and

COCO, which have the smallest and largest crustal motion respectively. Figure 5.3 shows the predicted displacement time series at COCO over a 30-day period. The horizontal motions are not significant, with predicted peak-to-peak amplitude of 9mm in South-North and 25mm in East-West. The vertical motion is much more significant, reaching 10 cm peak-to-peak. This vertical motion cannot be neglected for high precision GPS applications. Hence the ocean loading correction must be applied in order to ensure accurate troposphere delay estimates, which meet the accuracy requirements of the GPS meteorological applications.

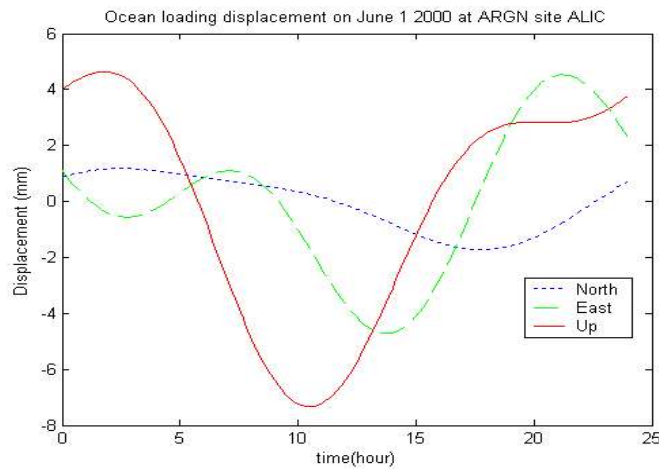


Figure 5.2a Ocean loading displacements on June 1 2000 at ARGN site ALIC.

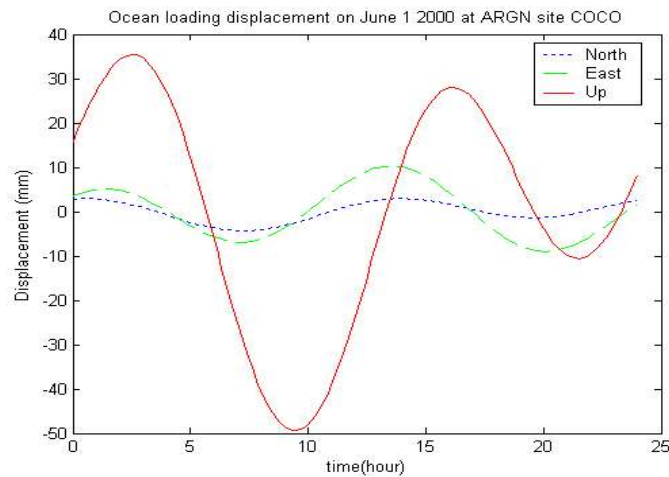


Figure 5.2b Ocean loading displacements on June 1 2000 at ARGN site COCO.

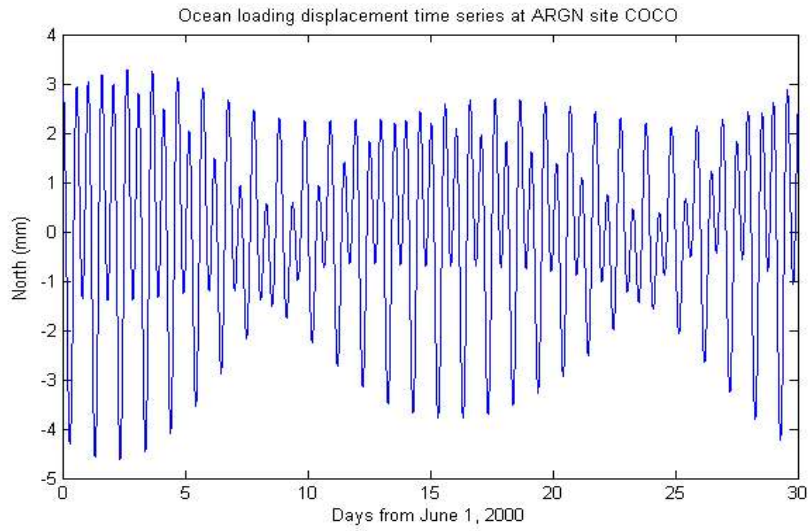


Figure 5.3a Ocean loading displacement time series at ARGN site COCO (North).

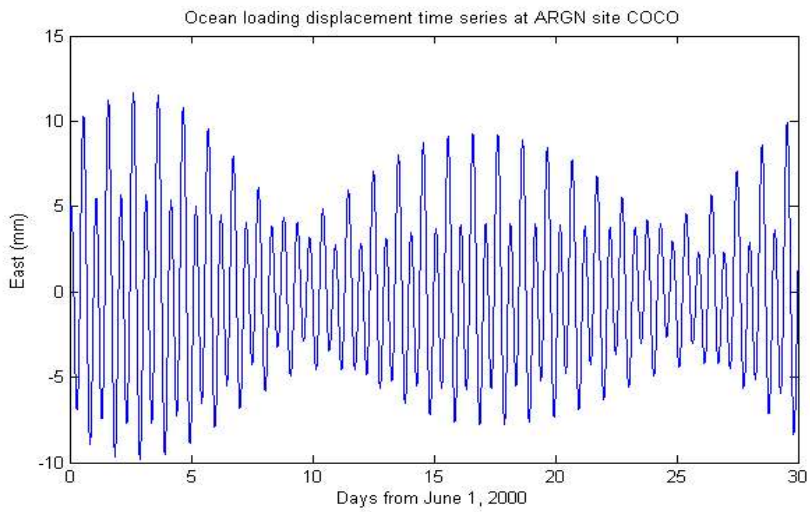


Figure 5.3b Ocean loading displacement time series at ARGN site COCO (East).

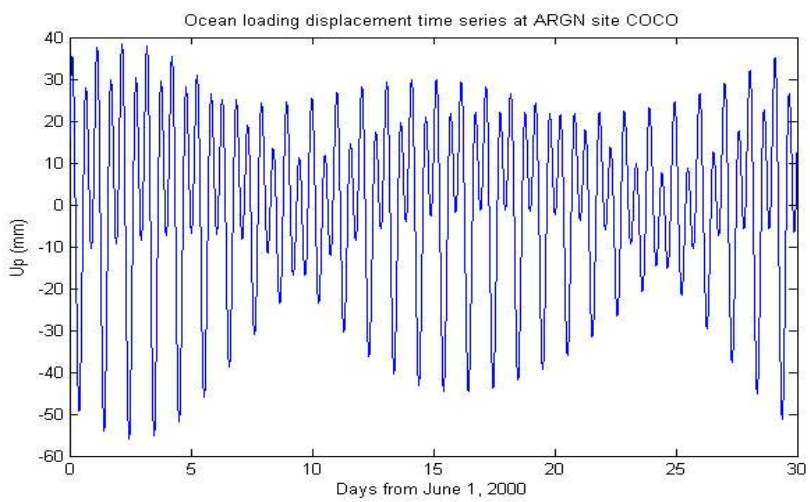


Figure 5.3c Ocean loading displacement time series at ARGN site COCO (Up).

5.3 GPS Measurements and Data Analysis

In order to detect periodic ground motion due to ocean loading, a 3-day period of GPS data (June 1-3, 2000) at ARGN sites sampled at 30 seconds interval was downloaded from ftp.auglis.gov.au and processed using the GAMIT software, release 10.7 [King and Bock, 1999]. The ITRF2000 was chosen to be the reference system. The IGS final orbits and IERS (International Earth Rotation Service) Earth orientation parameters were used. We used a 10 cut-off angle and elevation-dependent antenna phase centre models (using the tables recommended by the IGS). We applied solid Earth and polar tide corrections following the IERS standards [IERS, 1996], however ocean loading corrections were not applied. The Saastamoinen model and standard meteorological data were utilized, and the Niell model was selected for the mapping function for the dry and wet delay components.

It is well known that the accuracy of GPS measurements deteriorates with decreasing session length, mostly because of multipath and satellite constellation geometry effects (that can be averaged out over 24-hour periods). In addition, the ratio of the number of parameters to observations decreases and it becomes difficult to simultaneously solve for integer ambiguities, together with the position and tropospheric delay parameters. We have tested various processing strategies and found that the best results were obtained with 3-hour sessions, a 10 cut-off angle and only 1 tropospheric delay parameters per site per session. The 3-hour solutions are a compromise between shorter but noisier sessions, and longer sessions that could detect the ocean loading signals.

An important aspect of our data processing strategy is that we do not fix any of the station positions to their apriori values. Instead, we use apriori constraints of 10cm for the horizontal components and 20cm for the vertical component for each station. Fixing these positions together with the orbits and Earth orientation parameters would result in propagating errors into other estimated parameters. We chose the apriori constraints to be 50% higher than the maximum predicted ocean loading effect at COCO at the time of the experiment.

Figure 5.4 plots the vertical displacement time series over the 3-day period (June 1-3, 2000) derived from the GPS measurements without ocean loading corrections, against the predicted values from the CSR 4.0 ocean tide model. The results show a good overall agreement between the GPS measurements and the model. The vertical displacements derived from GPS measurements are well correlated in phase and amplitude with the ocean-loading model. That implies that if we don't take the ocean loading into account, the results from GPS measurements will be strongly affected by ocean loading effects. Hence for precise geodetic positioning and GPS meteorological applications, it is important to estimate the ocean loading effects and apply an ocean loading correction to the GPS measurements, especially in coastal regions

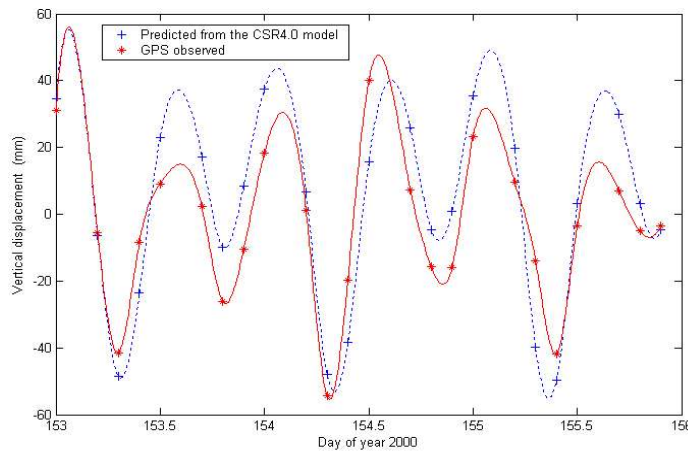


Figure 5.4 Vertical displacement time series over 3 days derived from GPS measurements versus ocean loading predictions at ARGN site COCO.

5.4 Impact of Ocean Loading on ZTD Estimates

In order to analyse the impact of ocean loading corrections on ZTD estimates, two months of continuous data from ARGN that included the above 3-day experiment period (Jun 1-30, 2000) were processed. The ARGN sites are separated by over 1000 km from each other, which can decorrelate the tropospheric delays and permit the estimation of absolute values [Tregoning *et al.*, 1998]. The data was processed on a daily basis using the GAMIT software, which parameterizes ZTD as a stochastic variation from the Saastamoinen model with piecewise linear interpolation. The variation is constrained to be a Gauss–Markov process with an apriori power density of $2\text{cm}/\sqrt{h}$. ZTD parameters were estimated at each station

every 30 minutes. We computed two sets of ZTD estimates: one with ocean loading correction applied, the other without. The other processing parameter settings were the same as in Section 5.3.

In the GAMIT 10.07 software, the file (station.oct) for the ocean tide correction of the station displacement contains the 11 tidal wave amplitudes and phases for more than 400 stations. While the ocean tide correction is calculated, first the program will search the file for a point within 10 km of the station. If such a point is found in the file, then the amplitude and phase of the ocean tide at this point will be assigned to the station. Otherwise, a linear interpolation on the global grid-table is made. In our experiment the amplitude and phase values of the 15 ARGN stations were first calculated from the CSR4.0 model, and then they were entered into the file station.oct.

We then differenced the ZTD times series obtained with ocean loading corrections applied from the ones obtained without ocean loading corrections applied. At a given site, this operation removes the signal of non-tidal origin common to the two solutions, leaving a residual that corresponds to the effect of ocean loading on the ZTD estimates. As expected, the resulting ZTD difference time series at COCO, for instance (Figure 5.5a), exhibits a periodic signature with a frequency similar to the predicted ocean loading effect on the vertical component of the station position (Figure 5.5b).

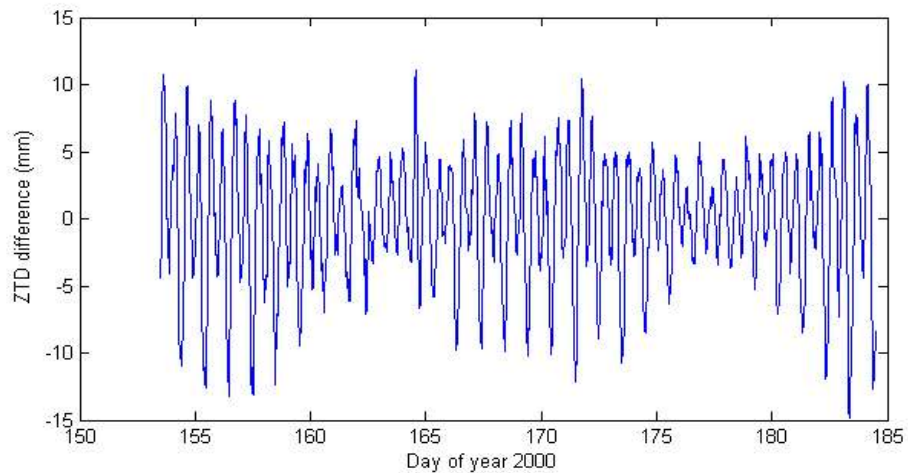


Figure 5.5a Time series of the ZTD differences for the ARGN site COCO, between the solution with ocean loading corrections and the solution without ocean loading corrections.

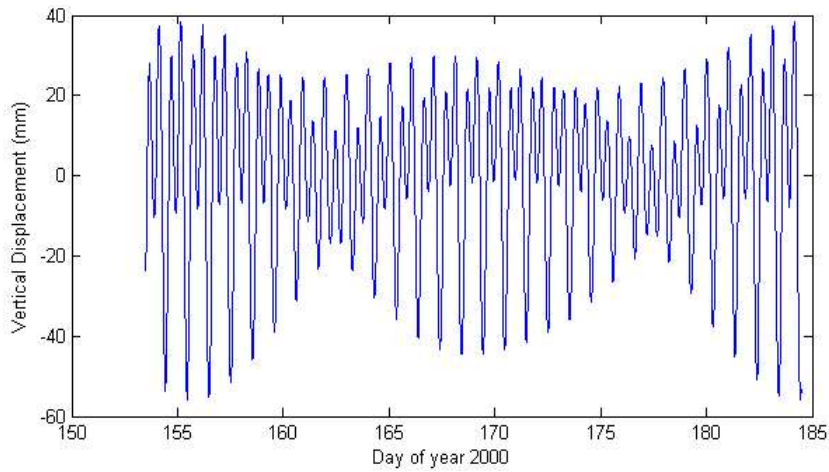


Figure 5.5b Time series of the modelled vertical position variations due to ocean loading at ARGN site COCO.

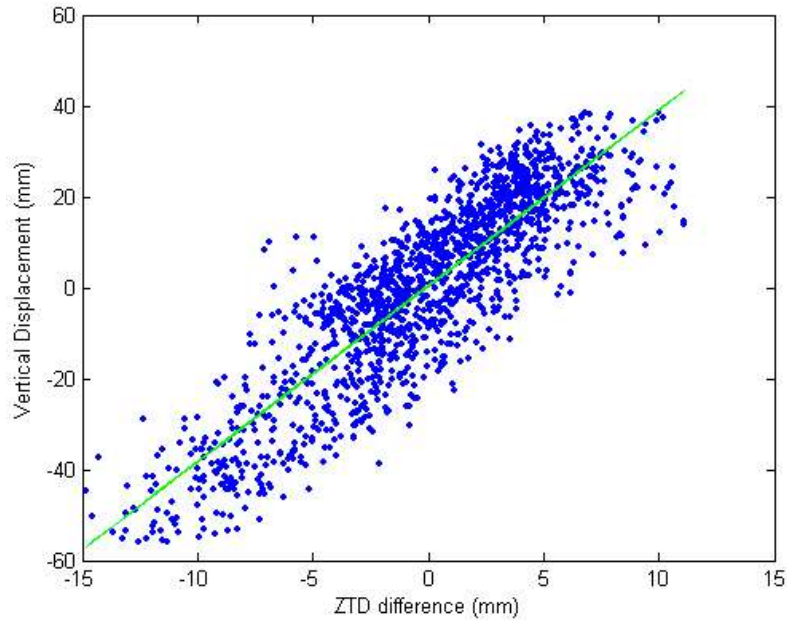


Figure 5.6 Illustration of ZTD difference between a solution with ocean loading correction and a solution without ocean loading correction, as a function of the vertical component of the predicted site position computed using the CSR4.0 ocean tide model.

Figure 5.6 shows the quasi-linear relation between the ZTD difference and the predicted height of the site, with a slope of 3.9. The relation between ZTD and vertical position implies that a 3.9cm station height error maps into a 1cm ZTD error. *Beutler et al.* [1988] first showed that this scaling factor, dependent on the elevation cut-off angle α used in the GPS data processing, can be approximated by $1/\cos(\alpha)$. Using a $\alpha = 10^\circ$ gives a scaling factor of 5.8, *Santerre* [1991]

refined this analysis by taking into account the satellite sky distribution and found a scaling factor of 4.1 at mid latitudes and for $\alpha = 10^\circ$. More recently, *Dach and Dietrich* [2000], using a GPS data set collected in Antarctica, found a scaling factor of 4.8 for $\alpha = 10^\circ$. The value of 3.9 found here is consistent with these previously published ones. However, the shape of the correlation on Figure 5.6 suggests that the relation between ZTD and height may not be linear, but that the scale factor is greater for larger ZTD values and lower for smaller ones.

Figure 5.7 also shows the time series of the ZTD difference and the vertical displacements at ARGN site COCO. But the ZTD differences were scaled by a factor of 3.9 to match the vertical displacements. Only one week out of one month's results are plotted in Figure 5.7. As expected, we observe a good correlation between the ZTD differences and the vertical displacement time series.

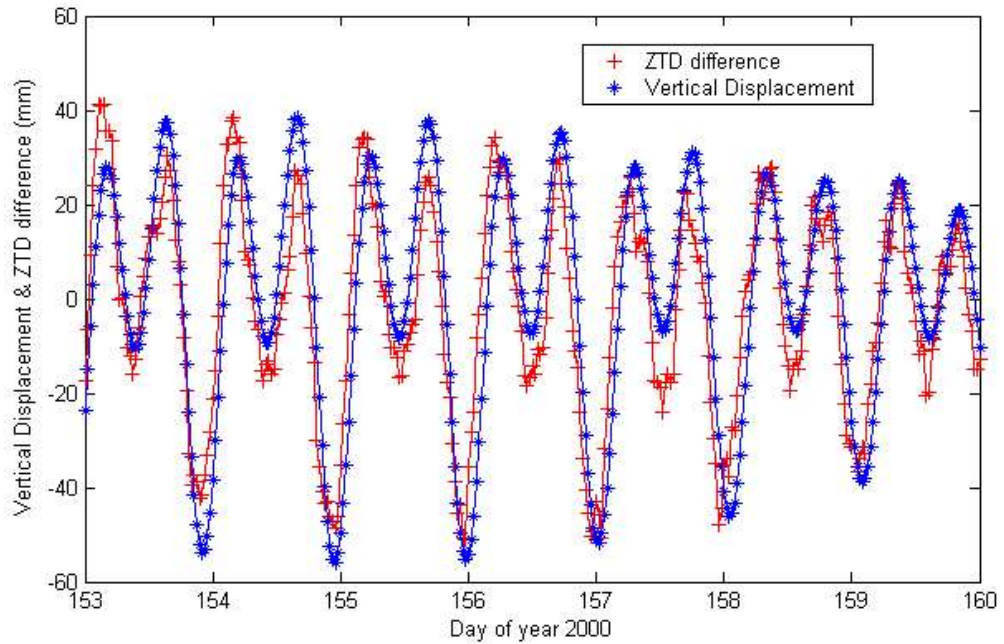


Figure 5.7 Time series of ZTD difference and the vertical displacement predicted using the CSR4.0 ocean tide model. The ZTD difference was multiplied by 3.9 in order to match the vertical displacement.

Figure 5.8 shows the power spectrum of the ZTD difference time series using 1 month of continuous data sampled at 30 min intervals. It can be clearly seen that there are two main peaks at semi-diurnal and diurnal frequencies. This further illustrates the effect of ocean loading on ZTD estimates.

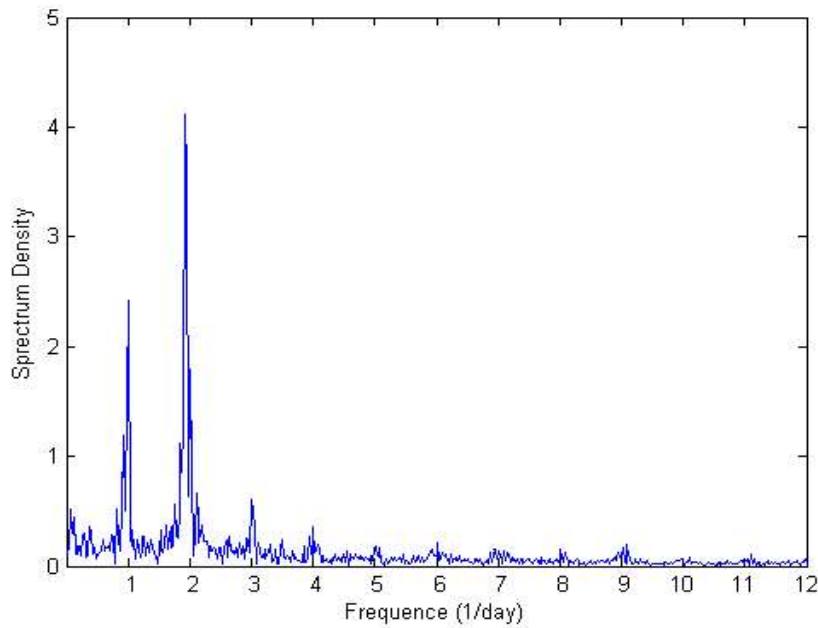


Figure 5.8 Power spectrum of the ZTD difference time series at ARGN site COCO, based on 1 month of continuous data sampled at 30 min intervals.

5.5 Impact of Ocean Loading on PWV Estimates

The results presented above demonstrate that ZTD estimates derived from GPS measurements can be significantly biased if ocean loading effects are not properly accounted for. For instance, an unmodelled 9cm peak-to-peak ocean loading effect on the vertical position component at COCO will result in a ZTD error of more than 2cm, which translates into about 3 mm (or kg/m²) error in precipitable water vapour (PWV), assuming a scale factor of 0.15 between the zenith delay and PWV [Bevis *et al.*, 1992]. Meteorological applications require that PWV parameters must be determined with an accuracy of 1mm or better, meaning that the accuracy of ZTD estimates should be better than 6.7mm. The ability to provide ZTD estimates with this level of accuracy requires that the modelling of ocean loading must be accurate to 2.6cm or better.

Figure 5.9 shows two sets of PWV differences between GPS-PWV estimates and radiosonde PWV estimates from day of year 180 to 280 in 2000 at ARGN site COCO, one with ocean loading correction applied and the other without. Table 5.2 and 5.3 list the statistics of the two sets of PWV differences for five GPS

stations at which radiosonde data is available. A total of 699 comparisons are included in the mean, standard deviation, root mean square values. From Figure 5.9 and Tables 5.2 and 5.3, it can be seen the GPS-PWV estimates with ocean loading corrections applied are only slightly improved compared to radiosonde PWV estimates. This is because the effects of ocean loading on the ZTD solutions may have been mostly averaged out using 24 hours of data. If we use a data arc of shorter than 24 hours the effects of ocean loading on the PWV result would be more distinct. Unfortunately, short data sessions can not generate accurate ZTD estimates for a widely spaced network such as the ARGN (>5000km). We have processed the GPS data with a 8h data session, and the ZTD RMS is 8mm compared to the results with 24h data session. This resulted in the GPS-PWV estimates are not accurate enough to be compared with the radiosonde results. Thus the results from 8h data periods are not given here.

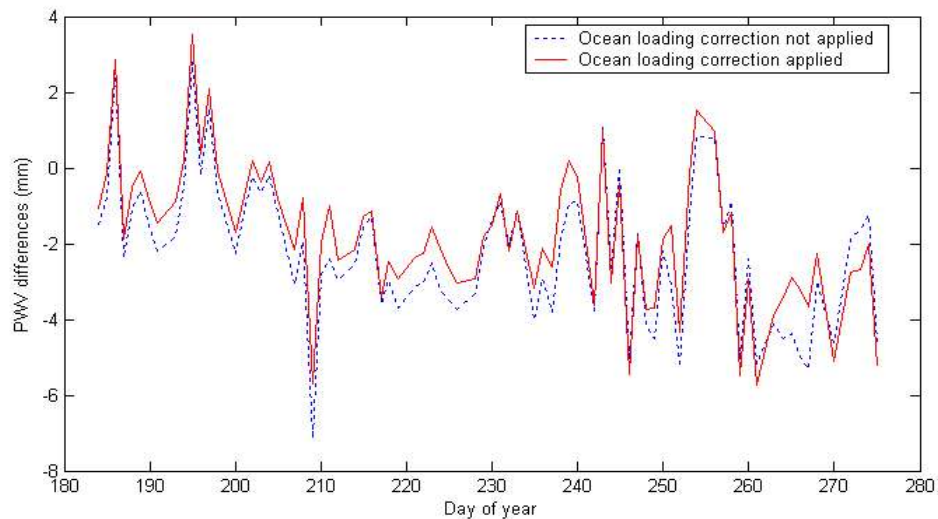


Figure 5.9 PWV differences between GPS-PWV estimates and radiosonde PWV estimates from day of year 180 to 280 in 2000 at ARGN station COCO.

Table 5.2 Comparison of GPS IPW estimates with radiosonde IPW estimates during a 3-month period (ocean loading correction not applied).

	All	ALIC	COCO	DARW	HOB2	TOW2
Number	699	104	159	195	159	82
Max of Rad-GPS	17.00	3.60	17.00	10.56	8.94	10.76
Mean (Rad-GPS)	-1.21	-1.12	-1.06	-0.45	-1.78	-2.35
RMS (Rad-GPS)	1.99	0.74	2.24	2.29	1.09	2.07
STD (Rad-GPS)	2.00	0.99	2.28	2.30	1.13	2.07

Table 5.3 Comparison of GPS IPW estimates with radiosonde IPW estimates during a 3-month

period (ocean loading correction applied).

	All	ALIC	COCO	DARW	HOB2	TOW2
Number	699	104	159	195	159	82
Max of Rad-GPS	16.23	3.40	16.23	10.46	9.12	10.19
Mean (Rad-GPS)	-1.18	-0.97	-1.40	-0.31	-1.78	-1.90
RMS (Rad-GPS)	1.95	0.73	2.06	2.33	1.05	2.05
STD (Rad-GPS)	1.95	0.96	2.09	2.35	1.09	2.06

5.6 Conclusion

We have shown that GPS measurements can be used to estimate the corresponding ocean loading effect. We measured peak-to-peak displacements of 9cm in the vertical component and 3cm in the horizontal component at ARGN site COCO using 3-day GPS data set. The vertical and horizontal displacements due to ocean tidal loading are calculated from both a global ocean tide model and GPS data, and the two displacement time series agree well. The GPS measurements are usually in good agreement with ocean loading model predictions in phase, whereas the agreement in amplitude is fair but typically not as good as that in frequency. The amplitude misfit is mostly caused by unmodelled tropospheric heterogeneities.

We have shown that unmodelled ocean loading effects translate into significant errors in ZTD estimates, with a scaling factor of 3.9 between ZTD and height for a 10° elevation cut-off angle. This effect increases approximately as the cosine of the elevation cut-off angle, as shown by *Beutler et al.* [1988]. It is therefore important that ocean loading modelling is properly implemented when estimating ZTD parameters from GPS measurements for meteorological applications. These applications require an accuracy of 1mm in PWV, which implies that ocean loading effects must be modelled with an accuracy of 2.6cm or better. This level of accuracy can be reached by most ocean loading models.

To investigate the impact of ocean loading on GPS derived precipitable water vapour, the GPS data over a three-month period collected from the ARGN are processed. Precipitable water vapour solutions were retrieved from GPS data with and without ocean loading corrections applied and compared with PWV results

derived from radiosonde data. The results show that the accuracy of GPS derived PWV are improved by applying ocean loading corrections. Consequently, ocean loading modelling must be properly implemented when estimating PWV parameters from GPS data for meteorological applications.

Chapter 6

GPS Sensing of Slant Water Vapour

Compared to traditional water vapour observing systems such as radiosondes, the GPS water vapour technique has many advantages, such as relative low cost for infrastructure, system operation and maintenance, high temporal resolution, high measurement accuracy, all weather operability and long-term measurement stability. However, taking full advantage of this technology does not come without cost. Firstly, operational water vapour estimation in a large GPS network must be completed in near-real-time in order to support near-term/short-range weather forecasting applications. Near-real-time (hourly or half-hourly) GPS water vapour estimation requires considerable amount of additional research and development effort, e.g. to improve the data flow efficiency and GPS data processing strategies. Secondly, the current PWV techniques provide only one integral water vapour measurement vertically above each station every 30 minutes. No direct water vapour information in the lateral directions is provided by the PWV technique. It is possible to deploy a very dense GPS network to increase the spatial resolution. This, however, would increase the equipment cost significantly. The Slant Water Vapour (SWV) technique can address this deficiency. Researchers are investigating the new ways to use GPS-PWV as a "proxy quantity" for moisture profiles in weather forecasting. In this Chapter, we will address the challenge of slant-path water vapour estimation. The challenge of near-real-time data processing will be discussed in the next Chapter.

6.1 Definition

Slant Water Vapour (SWV) is defined as the integrated amount of precipitable water vapour along each ray path from an individual satellite to a GPS receiver [Ware et al., 1996]. GPS PWV measurements are essentially averages over all SWV measurements that are mapped to the equivalent zenith value, and averaged over a period of time typically ranging from between 5 and 30 minutes. The advantage of averaging is the noise reduction associated with longer time series and azimuthal asymmetry. But some useful information is also lost. For a single

site, recording measurements every 30 seconds from 5 - 12 satellites, there are between 300 and 720 observations averaged in a 30-minute estimate of PWV. PWV estimates only give information of water vapour in the zenith direction, and they contain no information on the spatial distribution of water vapour at a site. However SWV estimates do. The problem is that SWV parameters are more difficult to estimate than PWV because they do not benefit from averaging, and are thus strongly affected by noise due to instabilities in the GPS receiver and transmitter oscillators, satellite orbit error, site multipath, and antenna effects.

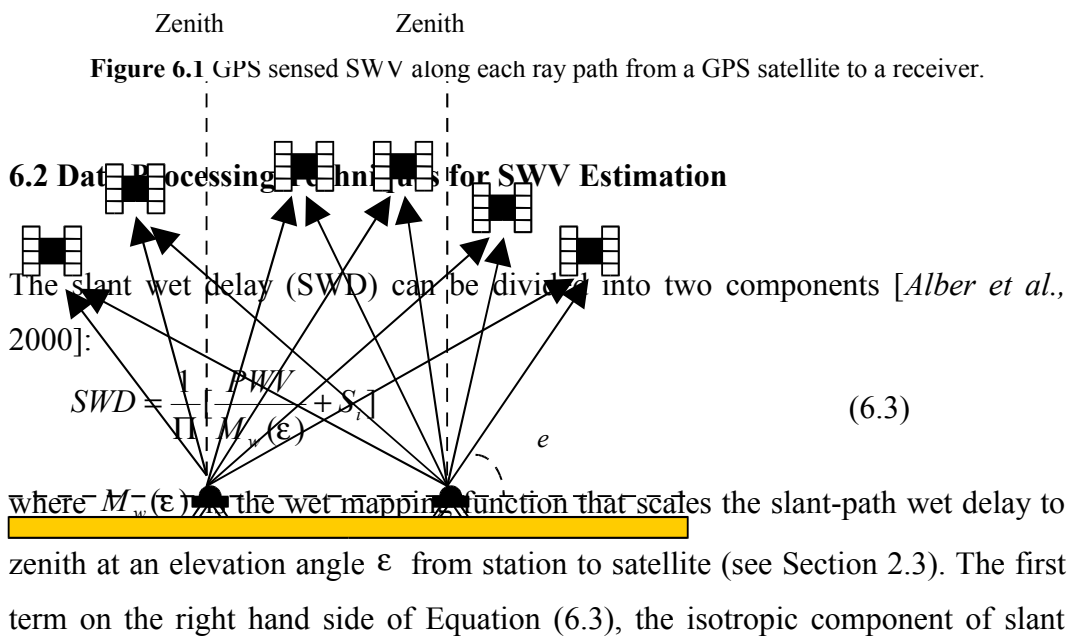
Similar to the definition of ZWD, Slant Wet Delay (SWD) is defined as the integral of atmospheric refractivity due to water vapour N_w along the ray path ds from the transmitting GPS satellite to the receiving antenna [Alber, et al., 2000]:

$$SWD = 10^{-6} \int N_w ds \quad (6.1)$$

where N_w is the second term in Equation (2.14). SWD and ds have units of length along the ray path. The relation between SWD and SWV is similar to that between ZWD and PWV:

$$SWV = \Pi(T_m) \cdot SWD \quad (6.2)$$

where $\Pi(T_m)$ is the dimensionless conversion factor, as in Equation (2.26). GPS sensed SWV along each ray path is illustrated in Figure 6.1.



water vapour, can be computed from the PWV measurements. The second term S_i represents the non-isotropic component of the slant water vapour. The term is zero when the atmosphere is perfectly isotropic, negative when the GPS signal passes through a region of low water vapour content relative to the PWV estimate, and positive when it passes through a region of high water vapour content relative to the PWV estimate. Typically, the magnitude of the second term is less than 20% of the PWV term (see for example *Rocken and et al.*, 1993, and *Jarlemark et al.*, 1995). S_i can be obtained by accurately modelling and correcting for the clock delays, geometric delays, hydrostatic delay, ionospheric delay, and the isotropic part of the wet delay. After these components of the GPS measurements are correctly removed, the residual (observation minus model) is the delay caused by the non-isotropic component of the *SWV*, or S_i .

Modelling of the GPS observations can be done with either the precise point positioning (PPP) [*Zumberge et al.*, 1997] or with double-difference processing (DDP) [*Beutler et al.*, 1999]. The PPP technique has the advantage that the line-of-sight observations from the receiving antenna to each transmitting satellite are individually modelled. The resulting residuals are then the non-isotropic component of the wet delay. The disadvantage of PPP analysis is that accurate receiver and satellite clock values are needed. Typically, satellite clock values are computed from a large, often global, GPS tracking network in the same processing step that the orbits are computed. These satellite clock values are then distributed in the same IGS file as the orbits. The receiver clock is included in the estimation process as a random walk parameter when PWV is estimated. In addition to the receiver clock estimate, it is not possible to resolve the integer carrier phase ambiguities in PPP. The DDP technique removes the GPS satellite and receiver clock errors and permits ambiguity resolution by differencing simultaneous observations from two sites and two satellites. The disadvantage is that the resulting residual is a combination of four observations instead of one. Because DDP eliminates clock estimation and allows for ambiguity resolution, it is more sensitive to small variations in S_i than the PPP technique. This is especially important for meteorological applications because the non-isotropic component of *SWV* can be small, and results must be available in close to real-time, but

accurate clock estimates are generally not available in real-time.

The GPS data processing methodology can be summarised as follows: First, compute PWV estimates for each station at half hour intervals using the techniques described in Chapter 3. Then invert the post-fit double-difference residuals into the line-of-sight SWD residuals. Finally, convert these SWD residuals into SWV residuals S_i using a Π value computed from the mean weighted temperature. The first step has been discussed in previous chapters. The following Section will discuss the next two steps.

6.3 Obtaining One-Way Phase Delay Residuals from Double-Differenced Residuals

Alber [2000] describes a method for obtaining one-way phase delay residuals (which can then be converted into non-isotropic slant water observations) for an individual ray path between a transmitting satellite to a receiving antenna from double-differenced residuals. From Equation (3.3), a double-difference for site pair A and B and satellite 1 and 2 can be expressed as:

$$DD_{AB}^{12} = SD_{AB}^2 - SD_{AB}^1 = (ZD_B^2 - ZD_A^2) - (ZD_B^1 - ZD_A^1) \quad (6.4)$$

where SD represents single-difference and ZD represents a zero-difference (one-way carrier phase observation). To convert double-differences to single-differences, all the double-differences for an individual baseline AB are written as the product of a matrix M_{AB} and a vector of single-differences SD_{AB} :

$$DD_{AB} = M_{AB} \cdot SD_{AB} \quad (6.5)$$

If there are n single-differences for a baseline AB, only n-1 double-differences are linearly independent, and M_{AB} cannot be inverted, an additional independent constraint is then introduced to make M_{AB} invertible. As shown in Equation (6.6), the additional constraint is expressed at the upper right as a weighted sum of the single-differences between sites A and B at one observation epoch. The satellite-dependent weighting for the site pair AB and satellite i is w_{AB}^i . The value of $\sum w_{AB}^i SD_{AB}^i$ can be estimated using model parameters from the GPS analysis, or by using a pointed water vapour radiometer (WVR) with a barometer or model for

total delay estimation.

$$\begin{bmatrix} w_{AB}^1 & w_{AB}^2 & w_{AB}^3 & \cdots & w_{AB}^n \\ -1 & 1 & 0 & \cdots & 0 \\ -1 & 0 & 1 & \cdots & 0 \\ \vdots & \vdots & \vdots & \vdots & \vdots \\ -1 & 0 & 0 & \cdots & 1 \end{bmatrix} \begin{bmatrix} SD_{AB}^1 \\ SD_{AB}^2 \\ SD_{AB}^3 \\ \vdots \\ SD_{AB}^n \end{bmatrix} = \begin{bmatrix} w_{AB}^1 SD_{AB}^1 + \cdots + w_{AB}^n SD_{AB}^n \\ SD_{AB}^2 - SD_{AB}^1 \\ SD_{AB}^3 - SD_{AB}^1 \\ \vdots \\ SD_{AB}^n - SD_{AB}^1 \end{bmatrix} = \begin{bmatrix} \sum_{i=1}^n w_{AB}^i SD_{AB}^i \\ DD_{AB}^{12} \\ DD_{AB}^{13} \\ \vdots \\ DD_{AB}^{1n} \end{bmatrix} \quad (6.6)$$

If all the GPS observation effects are well modelled and the post-fit double-

differenced residuals are used in Equation (6.6), then setting $\sum_{i=1}^n w_{AB}^i SD_{AB}^i$ equal to

zero (the "zero mean" assumption) produces an inverse where the single-differences retain the unmodelled part of the double differences. Included in these single-differences are effects such as multipath or tropospheric inhomogeneities. The constraint can be improved by downweighting the single-differences at low elevation angles.

The same procedure can be applied to obtain zero-differences using all single-differences to a given satellite from all linearly independent site pairs in the GPS network. Starting with Equation (6.7):

$$SD^i = M^i \cdot ZD^i \quad (6.7)$$

where M^i is a matrix operating on a vector of zero-differences ZD^i for the i 'th satellite to produce the vector of single-differences SD^i . We obtain a form for M^i including an additional constraint (upper right) on the zero-differences:

$$\begin{bmatrix} w_A^i & w_B^i & w_C^i & \cdots & w_N^i \\ -1 & 1 & 0 & \cdots & 0 \\ -1 & 0 & 1 & \cdots & 0 \\ \vdots & \vdots & \vdots & \vdots & \vdots \\ -1 & 0 & 0 & \cdots & 1 \end{bmatrix} \begin{bmatrix} ZD_A^i \\ ZD_B^i \\ ZD_C^i \\ \vdots \\ ZD_N^i \end{bmatrix} = \begin{bmatrix} w_A^i ZD_A^i + \cdots + w_N^i ZD_N^i \\ ZD_B^i - ZD_A^i \\ ZD_C^i - ZD_A^i \\ \vdots \\ ZD_N^i - ZD_A^i \end{bmatrix} = \begin{bmatrix} \sum_{I=1}^N w_I^i ZD_I^i \\ SD_{AB}^i \\ SD_{AC}^i \\ \vdots \\ SD_{AN}^i \end{bmatrix} \quad (6.8)$$

The weighting for the i 'th satellite at the I 'th site is w_I^i and $\sum_{I=1}^N w_I^i ZD_I^i$ includes

single path effects to the i 'th satellite from each site. As before, we can downweight the zero-differences used in the constraint at low elevation angles. If

$\sum_{I=1}^N w_I^j ZD_I^j$ is assumed to be zero, zero differences can be obtained, which represent the slant delay fluctuations about the model used to obtain the double- and single- differences.

In brief, the technique depends on two assumptions. First, the sum of the single-differenced residuals to all satellites visible at each observation epoch for a pair of stations in a baseline must be equal to zero. This implies that the observations must be sufficiently well modelled so that for every baseline in the solution, the sum of the unmodelled component of the single-differenced observations is equal to zero. Errors in this assumption arise when station biases are left in the solution. This can occur when the mean atmospheric delay (caused by PWV) is not removed, or when incorrectly resolving carrier phase ambiguities. The second assumption requires that the sum of the unmodelled portion of the observations from all the stations in the network to a single satellite is zero. Errors in the assumptions, and their effects on the individual line-of-sight residuals, are reduced by increasing the number of stations processed in the network and by increasing the baseline length to avoid common mode errors. The resulting line-of-sight residuals contain unmodelled atmospheric delay, antenna phase centre variations, and station multipath. In order to retrieve accurate atmospheric signals from the line-of-sight residuals, the antenna phase centre variations need to be accurately modelled and the multipath errors must be kept to a minimum. After the residuals have been corrected for these station specific errors, they can be multiplied by $\Pi(T_m)$ to become the S_i observations.

In both inversions, any error in the zero-mean assumption is divided equally over all stations in the network. For example, for a 10 site network, if a 10mm delay is present in one ZD, the mean residual will have a 1mm error. The ZDs are relative to the ensemble mean of the network. This implies that large networks can be used with careful modelling to minimize biases. Station coordinates should be held fixed to known long-term averages to avoid correlation with slant delays.

For tropospheric slant delays, the zero-mean assumption implies that the residual

delay in the direction of one GPS satellite at each epoch, averaged over the entire GPS network, is equal to zero. For a GPS network that is distributed over a large area, this assumption is generally valid because the distribution of water vapour at the sites can be considered random and the mean zenith delay can be estimated and removed. For a small network, if all stations observe a satellite through the same volume of atmosphere, the delay will have common mode elements that cannot be resolved. One method to compute absolute slant delays for a small network uses a collocated pointed radiometer and barometer (or modelled pressure fields) at one site. Absolute slant delay calculated from the wet and dry delay measurements at the collocated site can be used to lever absolute slant delays at the other sites. Another method is to analyse the small network within a larger network in order to minimize common mode error.

6.4 Construction of Stacking Multipath Map

The post-fit one-way phase residuals contain unmodelled atmospheric delay, antenna phase centre variations, station multipath, satellite orbit errors and other unmodelled phase errors that are not considered in GPS analysis. Normally, the site coordinates, carrier phase ambiguities, GPS orbits, antenna phase centre variations and mean atmospheric delay can be accurately modelled for meteorological applications, so that the post-fit one-way phase residuals are only dominated by the unmodelled atmospheric slant delay and ground scattered multipath. If the multipath can be removed from the post-fit phase residuals, the remaining residual can be multiplied by $\Pi(T_m)$ to become the S_i observations.

An effective way to remove multipath from post-fit phase residuals is using the stacking multipath map. Unmodelled atmospheric delay varies on a daily basis, but the multipath tends to repeat in sidereal time. So the daily post-fit phase residuals can be averaged for several days (stacking) to produce a multipath map. Multipath effects can be corrected by either directly subtracting the stacked multipath map from the residuals or incorporating the map into the modelled observations during data processing. Actually, the multipath maps not only contains the intrinsic site multipath itself, but also any stationary noise sources

which repeat at a given elevation and azimuth from day to day, such as unmodelled phase centre variation.

6.5 Experiment Description and Analysis

Data from the ARGN were analysed to retrieve the slant water vapour for the 10-day period from June 9-18, 2000. All GPS data were processed using the GAMIT software (v10.07). Final orbits from the International GPS Service (IGS) were used. The station coordinates were tightly constrained to the ITRF2000 reference frame. Data were collected at 30-second intervals and the mask angle of 10 degrees was used. The vertical coordinate repeatability for the experimental period of solutions was 2-3mm. As we discussed in Chapter 5, the vertical position errors and PWV errors are correlated. For example, a 3mm vertical error introduces a 0.1mm error in PWV when analysing data with a 10 degree elevation cut-off angle. While coordinate errors cause errors in PWV, they will not affect the non-isotropic component of SWV as defined in Equation 6.3. Surface pressure measurements were used with the Saastamoinen model to remove the dry delay. PWV estimates for each station were computed using all observations collected during a half hour interval, and the wet Niell mapping function [Niell, 1996]. The double-differenced residuals were inverted into line-of-sight residuals using a separate program, and the technique given in Section 6.3. They were then converted into non-isotropic SWV observations (S_i) using a Π computed from observed surface temperature. The calculation of Π was discussed in Chapter 2.

The retrieved S_i observations can contain, in addition to the atmospheric signal, noise from ground reflections near the GPS antenna and from direction dependent variations in the phase response of the GPS antenna. These noise sources, to the first order, are a function of the elevation and azimuth angle of the incoming GPS signal and repeat on a daily basis according to the direction of the incident ray path. To minimize these errors, the line-of-sight residuals were averaged for the ten days to produce a multipath map. This map was then incorporated into the modelled observations during processing. The use of this map was modestly successful and the results are discussed in the following paragraphs.

Figures 6.2 and 6.3 show the LC one-way residuals for ARGN sites ALIC and DARW respectively, for three days (DOY 161-163, 2000). The day-to-day repeatability of the LC one-way residual fluctuation can be clearly seen in these figures, which was grouped into the effects of site multipath.

To characterize the multipath signals, the line-of-sight residuals were averaged for the 10 days to produce a multipath map. Figure 6.4 shows the slant path delay (SPD) residuals with respect to satellite elevation and azimuthal angles using the sky plot at ARGN sites ALIC (left) and DARW (right) on day 161, 2000. The upper panel is the original post-fit SPD residuals, and the middle panel is the multipath constructed from the 10 days of SPD residuals. The lower panel is the corrected SPD residuals obtained by subtracting the multipath map from the observed SPD residuals. The reduction of multipath error, particularly at low elevation angles, is evident in the corrected plot. Residual RMS variations are reduced from 6.21mm to 3.41mm at ALIC and from 7.21mm to 4.75mm at DARW, over all angles. Stacking of residuals allows for the separation of multipath and unmodelled atmospheric slant delay.

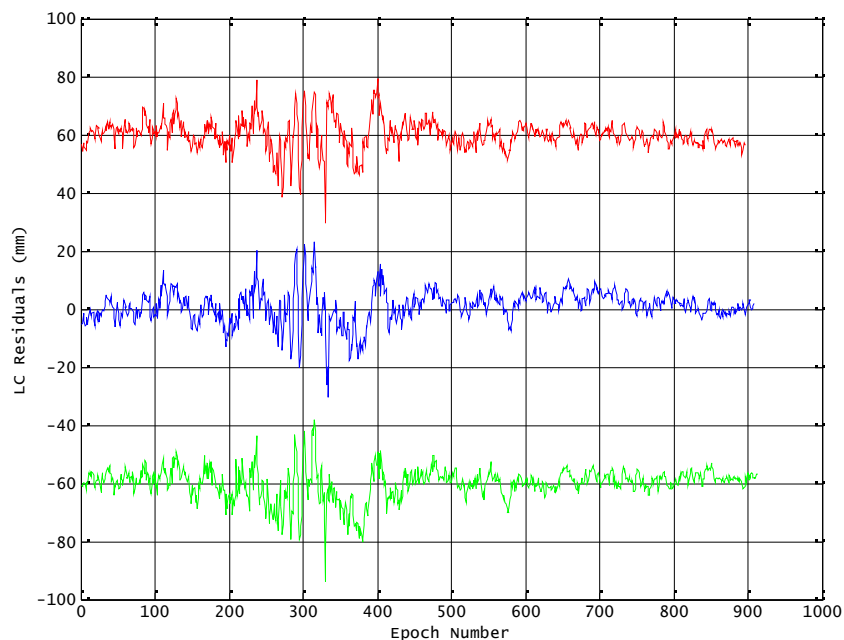


Figure 6.2 Day-to-day repeatability of LC one-way residuals. Curves show one-way errors for the ARGN site ALIC, satellite PRN 01, for three days. For clarity in comparison, the data from day 161 have been offset in amplitude by +60 mm and in time by 8 min; data from day 162 have been offset in amplitude by 0 mm and in time by 4 min; and data from day 163 have been offset in amplitude by -60 mm and in time by 0 min.

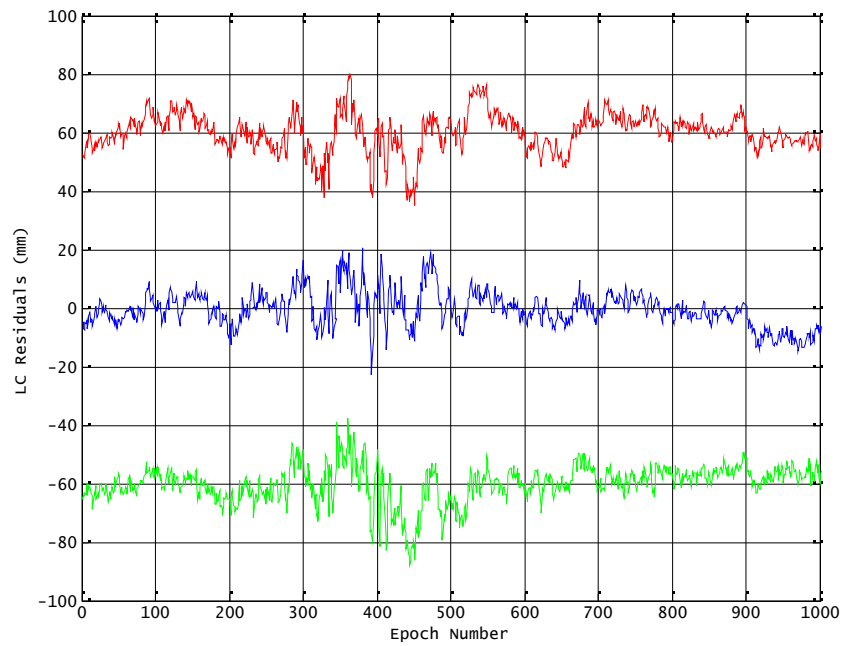
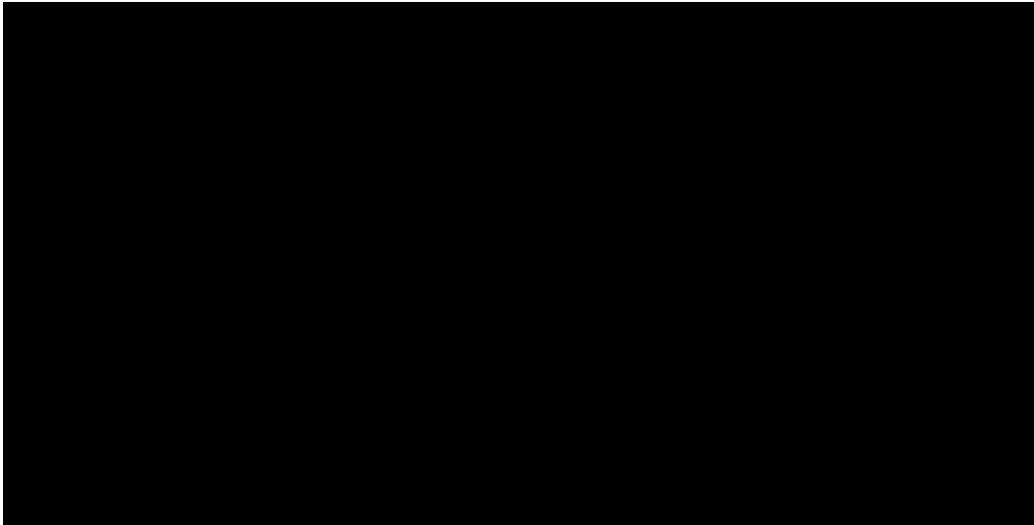


Figure 6.3 Day-to-day repeatability of LC one-way residuals. Curves show one-way errors for ARGN site DARW, satellite PRN 01, for three days. For clarity in comparison, the data from day 161 have been artificially offset in amplitude by +60 mm and in time by 8 min; data from day 162 have been offset in amplitude by 0 mm and in time by 4 min; and data from day 163 have been offset in amplitude by -60 mm and in time by 0 min.



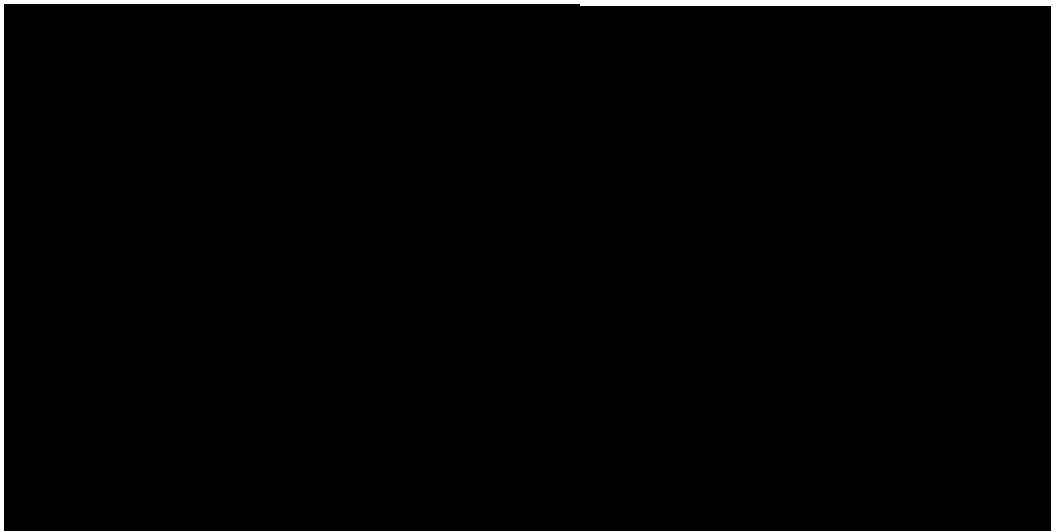
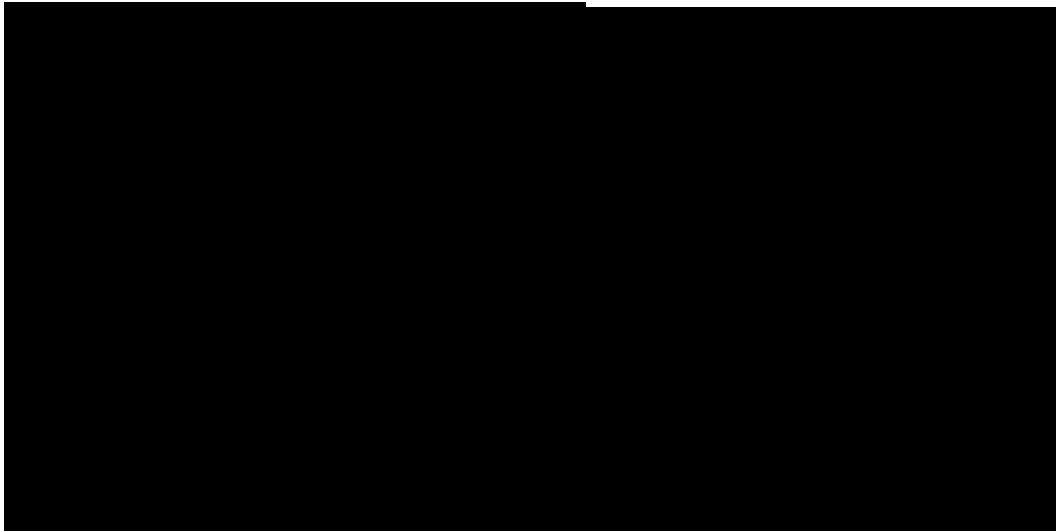


Figure 6.4 Slant path delay (SPD) residuals with respect to satellite elevation and azimuthal angles (“sky plot”) at ARGN site ALIC (left) and DARW (right) on day 161, 2000. The upper panel is the original postfit SPD residuals and the middle panel is the multipath constructed from 10 days SPD residuals. The lower panel is the corrected SPD residuals obtained by subtracting the multipath map from the observed SPD residuals.

Figure 6.5 illustrates the dependency of elevation angle and azimuth on the LC post-fit residuals at ARGN site ALIC on day 161, 2000. After the multipath effects were corrected using the stacking multipath map, both the elevation angle dependence and the azimuth dependence are reduced.

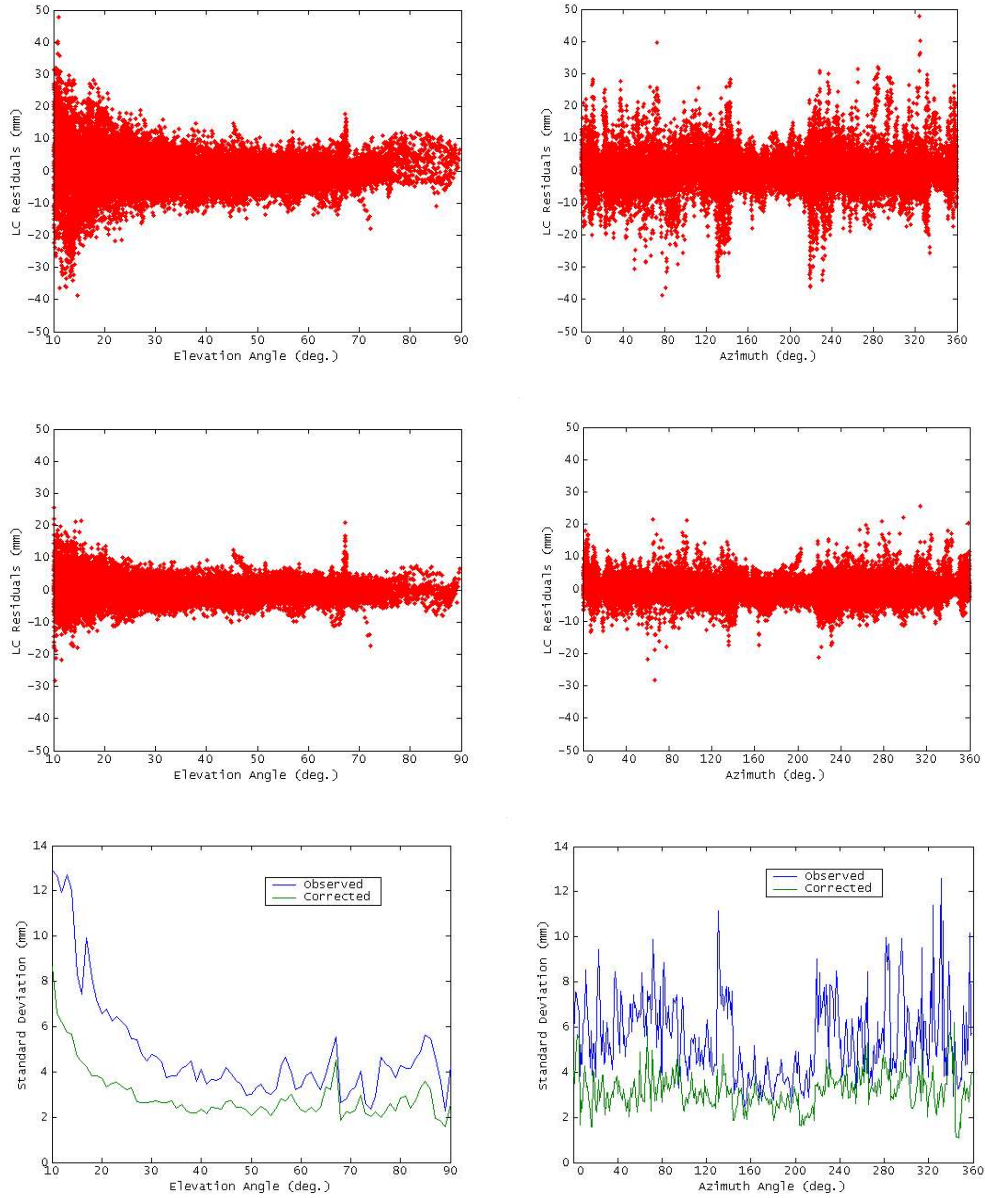


Figure 6.5 Illustration of dependency of the LC post-fit residuals on the elevation angle and azimuth at ARGN site ALIC on day 161, 2000.

Tables 6.1a-6.1e give the RMS of the LC post-fit residuals for the five ARGN sites ALIC, COCO, DARW, HOB2 and TOW2 before and after multipath correction, where SWV estimates were obtained for the experimental period (day 161-170, 2000). It can be clearly seen that all the RMS of the LC post-fit residuals

are reduced after multipath correction, which means the multipath exists at all the stations to a different extent. Better improvements were seen at ALIC and DARW while other sites have little improvements.

Table 6.1a RMS of LC post-fit residual before and after multipath correction for ALIC.

	161	162	163	164	165	166	167	168	169	170
Observed	6.2	6.5	6.1	6.2	6.1	6.4	7.0	6.4	6.7	6.3
Corrected	3.4	3.7	3.1	3.2	3.1	3.3	4.3	3.2	4.1	3.6

Table 6.1b RMS of LC post-fit residual before and after multipath correction for COCO.

	161	162	163	164	165	166	167	168	169	170
Observed	10.8	9.9	18.4	8.5	14.8	14.5	10.5	9.1	12.6	15.3
Corrected	9.4	9.4	16.9	7.1	13.3	13.1	9.2	7.5	11.4	13.5

Table 6.1c RMS of LC post-fit residual before and after multipath correction for DARW.

	161	162	163	164	165	166	167	168	169	170
Observed	7.2	8.2	8.3	8.3	10.0	11.0	9.3	7.9	10.1	7.2
Corrected	4.8	5.6	6.3	5.4	7.1	8.3	6.8	4.9	8.2	5.0

Table 6.1d RMS of LC post-fit residual before and after multipath correction for HOB2.

	161	162	163	164	165	166	167	168	169
Observed	9.3	9.3	6.9	8.0	7.4	7.7	10.5	10.0	11.3
Corrected	6.6	7.0	4.6	5.7	4.8	5.0	7.6	7.3	8.7

Table 6.1e RMS of LC post-fit residual before and after multipath correction for TOW2.

	161	162	163	164	165	166	167	168	169	170
Observed	8.3	7.4	5.1	6.2	5.7	8.3	7.2	6.5	6.8	5.5
Corrected	7.0	6.1	4.3	5.3	4.7	7.0	5.8	5.5	5.6	4.5

Figures 6.6 and 6.7 show the slant water vapour time series at ARGN sites ALIC and DARW respectively. Slant water vapour (green line) estimates were obtained at 30-second intervals and converted to zenith direction using Niell's wet mapping function to match the PWV estimates (blue dot). All the SWV estimates at the same epoch were then averaged to determine the SWV value at that epoch plotted in the figure. These values (the averaged SWV estimates after mapped into the zenith direction) have good agreement with the PWV estimates. But compared to PWV, SWV gives more information of the water vapour content in the atmosphere. In temporal resolution, PWV were obtained at 30-minute intervals while SWV were at 30-second intervals. In spatial resolution, PWV only gives the information in the zenith direction while SWV gives information in all directions.

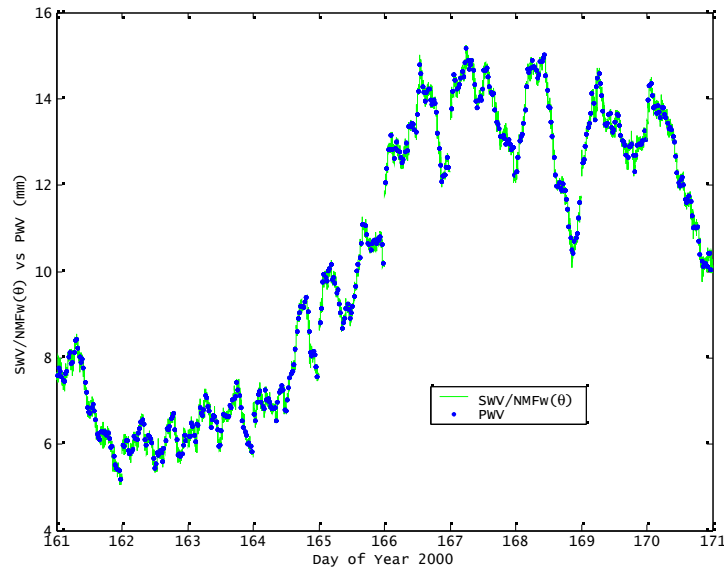


Figure 6.6 Slant water vapour time series at ARGN site ALIC.

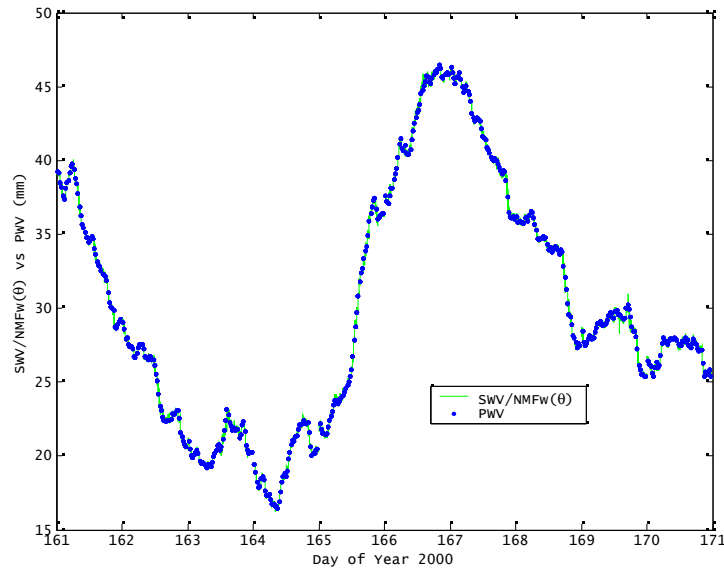


Figure 6.7 Slant water vapour time series at ARGN site DARW.

6.6 A Perspective for Applications of GPS Sensed SWV

SWV observations have the potential to be useful in reconstructing the three-dimensional water vapour field if they can be successfully assimilated into numerical weather models. Recent investigations into the potential use of line-of-sight estimates of path-integrated water vapour (derived from slant-path GPS signal delay measurements) to retrieve the 3-D moisture field have been very interesting and potentially significant [MacDonald and Xie, 2000]. The experiments involve assimilating simulated slant-path moisture measurements

from a wide area network of closely spaced stations into the Quasi-non-hydrostatic (QNH) model using variational techniques. In recent research, their simulations indicate that it may be possible to recover the three-dimensional structure of the moisture field from a densely spaced network of ground-based GPS receivers making a single line-of-sight, or slant path, measurement of the signal delay to all satellites in view. Assimilation techniques for this data type are currently under development at the National Centre for Atmospheric Research (NCAR).

GPS sensing of SWV should be possible down to 0° elevation angle and slightly below. At low elevation angles the method could be used to detect water vapour associated with fronts storms, and other weather and climate phenomena, at distances of several hundreds kilometres. SWV data could also be used to complement GPS occultation measurements [Ware *et al.*, 1996], and to correct for wet delay effects in GPS surveying, orbit determination and synthetic aperture radar (SAR) imaging of crustal deformation and topography [Delacourt *et al.*, 1998, Coops and Waring, 2001].

Chapter 7

Near-Real-Time GPS Water Vapour Estimation

As we mentioned earlier, improvements in numerical weather predictions are only possible if the atmospheric water vapour parameters can be monitored with high spatial and temporal resolution, which requires that GPS water vapour estimation must be completed in near-real-time and slant water vapour should be estimated. The slant water vapour estimation techniques have been discussed in Chapter 6. In this Chapter, we discuss the near-real-time data processing strategies in detail.

7.1 Requirements from Meteorological Community

The data qualities required for meteorology and climate applications are specified in Tables 7.1 and 7.2. Table 7.1 summarizes the generic requirements for operational meteorology, adapted from The General User Requirement Statement for Meteorological Data, drafted by World Meteorology Organisation (WMO).

Table 7.1 Generic requirements for operational meteorology.

	Column Specific Humidity	Total Zenith Delay
Horizontal Domain	Global / Regional	Global / Regional
Horizontal Resolution	< 300km / < 100km	< 300km / < 100km
Time Resolution	1-6 hrs / 1-2 hrs	1-6 hrs / 1-2 hrs
Absolute Accuracy	5000 g/m ² / 1000 g/m ²	30 mm / 6 mm
Timeliness	1-3 hrs / <1 hr	1-3 hrs / <1 hr

The Column Specific Humidity, or Integrated Water Vapour (IWV), is usually expressed in g/m², or alternatively as the equivalent height of the water column in mm (1000 g/m² = 1 mm). This is equivalent to about 6-7mm delay in the vertical (Zenith Wet Delay). The IWV can be computed from the Zenith Total Delay (ZTD) using surface pressure and the mean temperature of the atmosphere. Even if surface meteorological measurements are available, it is still difficult to compute the mean temperature, which is the main uncertainty in the conversion to IWV. Fortunately, the new generation of Numerical Weather Prediction (NWP) models, such as the so-called 3D- and 4D-VAR, can directly assimilate the ZTD from GPS.

Table 7.2 Generic requirements for climate monitoring and prediction.

	Column Specific Humidity
Horizontal Domain	Global
Horizontal Sampling ¹⁾	2.5° x 2.5°
Time Domain	> 10 years
Time Resolution	1/day → 1/hour
Absolute Accuracy	< 1000 g/m ²
No. of observations/grid box/day based on random accuracy	> 40
Long Term Stability	200-400 g/m ² /decade
Timeliness	1-2 months

Table 7.1 explicitly mentions users requiring data for regional and/or mesoscale NWP models. In general, the requirements are very similar except that horizontal resolution of 50km and timeliness of 1 hour are preferred for mesoscale applications. Table 7.2 illustrates in a similar way the user requirements for the climate community, in particular those for climate monitoring and prediction where trends in the past and future are analysed. The requirements for 'climatology' are very similar, except that long-term means are taken, and stable and low biases are demanded. To climate users, zenith delays are not desirable. They would either use time- and spaced-averaged individual water vapour columns, or use 3D analysed fields, which have assimilated GPS ground-based meteorology data via NWP systems.

To meet the needs for accurate measurements of atmospheric water vapour with precise spatial and temporal resolution for meteorological and climatological applications, it is necessary that GPS data be processed in near-real-time with a latency of 1 or 2 hours or less and slant path delay be estimated.

7.2 Near-Real-Time Data Processing

7.2.1 Definition

We define near-real-time (NRT) data processing as acquiring and processing GPS and ancillary observations to yield signal delay or PWV estimates within a single numerical weather prediction assimilation cycle [Gutman, *et al*, 2002]. In operational weather prediction, meteorological observations are typically

assimilated every 6 hours. With the new generation of meteorological satellite observations provided at intervals of 1 hour 40 minutes, the assimilation delay currently required by the World Meteorological Organization is approximately 2 hour 15 minutes or 3 hour 20 minutes at the latest. In the case of the Rapid Update Cycle, running operationally for Environmental Prediction, the assimilation delay is approximately 75 minutes [Dick *et al.* 2001]. In order to ensure that one cycle of observations is processed before the next satellite orbit is completed, GPS PWV must therefore be calculated in near-real-time with a minimum loss of accuracy if they are to be a useable data source in NWP models. To fulfil this objective, two main issues will be addressed in the following paragraphs: the use of real-time orbits, and the GPS processing strategy.

Near-real-time calculations of integrated water vapour measurements from GPS are difficult because of the necessity for precise orbit ephemerides for the GPS satellites. Precise orbit determination requires time series 48 hours in length or longer, i.e. several satellite passes, to accurately constrain the orbits. Thus, the orbits are calculated for the 48-72 hours previous to the time period for which the integrated water vapour is calculated, and given these parameters, the orbits are predicted for the time period of interest. Measurements must be made at a global network of stations in addition to the regional stations. This requires near-real-time communications and coordination with international data centres.

7.2.2 Differences between Near-Real-Time and Post Data Processing

Differences between post-processing and near-real-time data processing are given in Table 7.3. The main difference is the type of satellite orbit used. High precision rapid or final IGS orbits are available for post-processing, but they are not available for near-real-time processing. The precision of ultra-rapid and predicted orbits, which can be used for NRT processing, is relatively low. This in turn will affect the PWV accuracy achievable in NRT processing. Another difference is that NRT processing should be done within 1 or 2 hours after the last observation is made, while post- processing allows the process to be completed after 24 hours. GPS data processing is time consuming, especially for the networks of large number of stations. So some specific data processing techniques should be

adopted in NRT data processing.

Table 7.3 Differences between near-real-time and post data processing

Solution	Near-real-time processing	Post processing
Data organised and processed	Hourly	Daily
Orbits used	Ultra-rapid /predicted	Rapid / final
Delay	1-2 hours	1-10 days
Period	Last 24 hours	24 hours of current day
Solutions per day	24	1
ZTD resolution	5-30 minutes	5-30 minutes
Purpose	Meteorological applications	Climate applications

7.3 The Impact of Orbits on NRT Water Vapour Estimates

7.3.1 Availability of GPS Orbits

GPS satellite orbits play a critical role in GPS water vapour estimation [Beutler, Springer et al., 1999; Dousa and Mervart, 2001]. In terms of simplifying the data processing and estimating tropospheric parameters, precise GPS orbits are highly appreciated. Besides the demand for high orbit accuracy, there is a demand that the orbit product have stability as well as completeness of the data. The orbit product of the International GPS Service (IGS), based on the combination of up to 7 contributing individual solutions, is obviously the best choice. The product can be obtained freely from the IGS data centres. Currently, IGS provides three types of GPS orbit products: final, rapid and ultra rapid orbits. The most precise GPS orbits are the final orbits with an accuracy of about 2-3cm, which is sufficient to provide PWV estimates with an accuracy on the order of 1mm, however these orbits are available only after one or two weeks. IGS rapid orbits reach almost the same level of accuracy as the final orbits, but are available after 17 hours. IGS ultra rapid orbit generates 24 hours estimates, and 24 hours predicted orbits, every 12 hours with a latency of 3 hours, and can achieve an accuracy of 20cm with respect to the final product. Another IGS product, the IGS predicted orbits, have already been discontinued since the ultra rapid orbits became IGS official products on November 5 2000 with the start of GPS week 1087. The orbits availability from IGS is summarised in Table 7.4.

Individual IGS analysis centres and some other research institutes and

governmental agencies, also provide near-real-time GPS orbits for certain applications. Among of them, JPL provide near-real-time GPS orbits and satellite clocks with 15 minutes latency and updated every 15 minutes. The accuracy of the JPL 15min orbits reaches 30-40cm compared with the JPL final orbits.

Table 7.4 GPS satellite orbits available from IGS. More information can be found at <http://igscb.jpl.nasa.gov/components/prods.html>.

Product	Accuracy		Latency	Updates
	Orbits	Sat clocks		
Broadcast	~200 cm	~7 ns	real time	--
Ultra-Rapid (predicted half)	~10 cm	~5 ns	real time	twice daily
Ultra-Rapid (observed half)	<5 cm	~0.2 ns	real time	twice daily
Rapid	<5 cm	0.1 ns	17 hours	daily
Final	<5 cm	<0.1 ns	~13 days	weekly

With respect to their latency, only ultra-rapid and predicted orbits can be used for near-real-time GPS data processing. But great care has to be taken to assure the orbit quality.

7.3.2 Comparison of Orbits for Near-Real-Time Water Vapour Estimation

To assess the suitability of the predicted orbits in terms of the quality of the resulting GPS PWV estimates, GPS data of two weeks (GPS week 1257 and 1258, Feb 08-21, 2004) collected from the ARGN GPS network were processed with the IGS final, rapid and ultra rapid orbits and JPL 15min orbits. The IGS ultra rapid orbits consist of daily fitted and daily predicted portions of ephemerides. We used only the predicted segments of the orbit, i.e., the parts from 03:00 to 15:00 and from 15:00 to 03:00 UTC. There are only 13 days of predicted orbits available for processing. The results obtained using the IGS final orbits were taken as reference and all other results were compared to these. The results of the zenith tropospheric delay comparisons are summarized in Table 7.5. We see that the results using the IGS rapid orbits are almost indistinguishable from those that used the final results. The RMS of all ZTD difference is only 0.15mm, which may be considered to be within the noise level of the estimates. The results from the IGS ultra rapid orbits and JPL 15min orbits are also encouraging, the RMS is only 1.3mm and 1.2mm respectively. These results confirm that the IGS ultra rapid orbits and the JPL 15min orbits could be used for NRT GPS water vapour

estimation. Figure 7.1 plots the RMS of the above ZTD difference on an epoch-by-epoch basis over 13 days. It is clearly seen that the RMS on day 41 reaches up to 7mm, although the others remain within 2-3mm. The same error can be seen in Figure 7.2, which shows the mean ZTD difference epoch-by-epoch. The error of 7mm ZTD corresponds to approximately 1mm precipitable water vapour, which is not acceptable for meteorological applications. Therefore, this sort of error should be investigated and minimized in GPS NRT data processing.

Table 7.5 Comparison of ZTD estimates using different orbit products. The ZTD estimates obtained using the IGS Final orbits were used as reference to compare the other results with. All ZTD estimates at 30min interval from 15 ARGN stations over 2 weeks were included (there are only 13 days predicted orbits available for processing).

Orbit type	RMS	Std	Mean	Max	Min
IGS rapid	0.154	0.152	-0.026	0.760	-1.270
IGS Ultra Rapid	1.313	1.303	-0.163	24.680	-13.970
JPL 15min	1.181	1.169	-0.170	8.290	-9.670

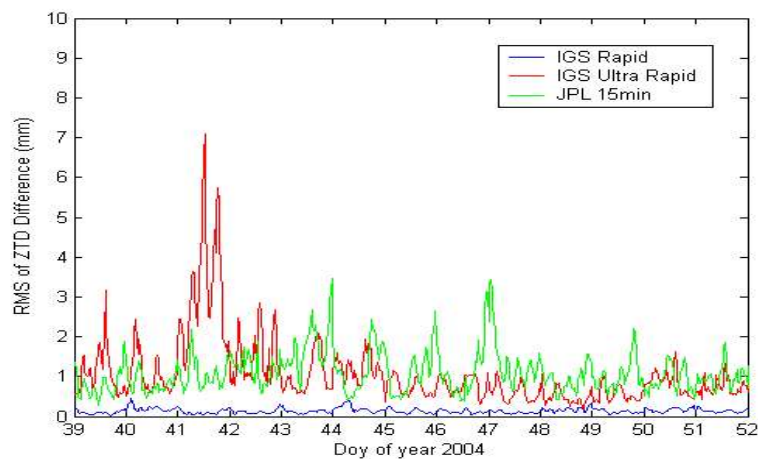


Figure 7.1 RMS of ZTD differences between the solutions using different IGS and JPL orbits.

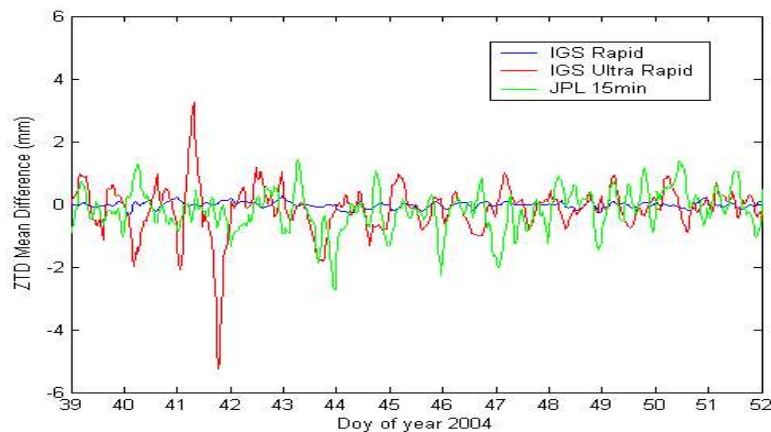


Figure 7.2 Mean differences of ZTD estimates between the solutions using different IGS and JPL orbits.

The orbits on day 41 are further analysed (Figure 7.4). It is clear that the error in Figures 7.1-7.3 is dominated by the large orbital error for satellite 29, which reaches 3.5 metres on that day. It is a quite common for certain predicted satellite orbits to have such occasional levels of inaccuracy. Fortunately, this doesn't happen very often. Therefore, if an appropriate satellite orbit quality assurance method is used, the orbits can still be used for NRT water vapour estimation. This will be discussed in the following paragraphs.

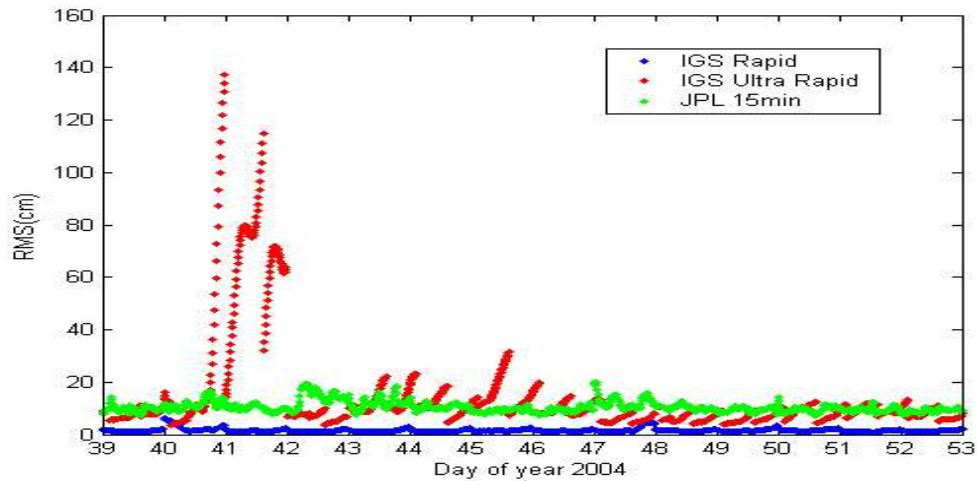


Figure 7.3 Comparison of IGS rapid, ultra rapid orbits and JPL 15 minute orbits with respect to IGS final orbit. For the IGS ultra rapid orbit, only the predicted portions (the parts from 3-15 and from 15-3 UTC) were used.

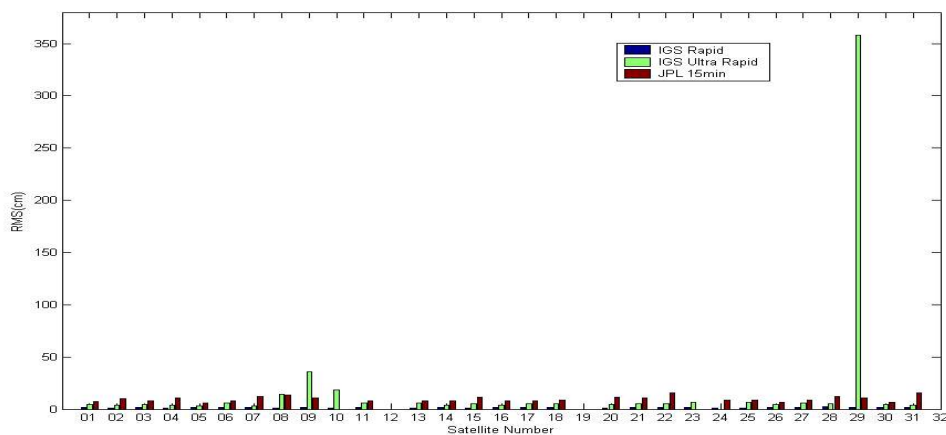


Figure 7.4 Comparison of IGS rapid, ultra rapid orbits and JPL 15 minute orbits with respect to IGS final orbit on day 41, 2004.

7.3.3 Reducing Effects of Orbital Errors on NRT Water Vapour Estimates

To achieve good accuracy in NRT water vapour estimation, we have to reduce the influence of badly predicted orbits. The predicted orbit errors could reach 10 metres in the along-track direction on some occasions [Dodson and Baker, 1998]. Although such large errors are rare, their effect on the accuracy of water vapour estimates is dramatic. Therefore the satellites with serious problems should be identified through the use of orbit quality control procedures and excluded or down-weighted in near-real-time GPS data processing.

Several strategies have been proposed for orbit quality control:

- The first technique is overlap checking. This approach first differences the overlap part of the orbital segment from adjacent solutions. Whenever the differences become greater than a certain pre-set criterium, the satellites are flagged and then excluded or de-weighted during the data processing. The major weakness of this procedure is that the differences may not be sensitive enough since the adjacent solutions use overlapped observations, and their orbit estimates become correlated.
- The second method uses accuracy codes as quality indexes, which are provided with the header of the orbit files, to define low accuracy satellites [Remondi, 1989]. The low accuracy satellites are flagged accordingly and then excluded or de-weighted during the data processing. However, the quality index is not always a reliable indicator of the orbit quality, and does not represent an actual estimation of the orbit accuracy because it is derived from the previous day's data processing.
- The third one implements a processing strategy based on an iterative estimation of three orbital parameters (semi-major axis, inclination and argument of perigee) together with the ZTD parameters. These orbital parameters and their apriori variance are updated iteratively until a detection criterium is no longer exceeded for any satellite. The final ZTD estimates are taken from the last iteration [Ge et al, 2000].

Compared to the first two approaches, the third one is more reliable though it is a little more sophisticated. The method was used in this study and implemented in

our automatic GPS data processing. Using this approach, the data were then reprocessed. The effect of the low accuracy satellite 29 on ZTD estimates on day 41 was successfully mitigated in the data processing. The ZTD results were significantly improved, exhibiting much better agreement with the ZTD estimates using the IGS final orbits, while the results for the other days remains almost the same. Figures 7.4 and 7.5 show the RMS and mean ZTD difference epoch-by-epoch after the proposed orbit quality control procedure was applied. Compared to Figures 7.1 and 7.2, we see that the large peak on day 41 in Figures 7.1 and 7.2 has disappeared. The maximum RMS of the ZTD differences between the IGS final orbit ZTD estimates and the IGS ultra rapid orbit ZTD estimates has reduced from 7.1mm to 3.6mm and the peak-to-peak mean ZTD difference is reduced from 9mm to 5mm. The results thus suggest that for near-real-time applications, IGS ultra rapid orbits or JPL 15min orbits are suitable as long as the low accuracy satellites are automatically removed from the GPS solution.

It should also be noted that it is possible to de-weight the low accuracy satellites, or remove them from the data processing, or to use orbit relaxation techniques [Kruse *et al.*, 1999]. The satellite exclusion approach is perhaps more useful because of the possible specification of the exclusion time interval. The second reason for exclusion is that changing the weights will influence the definition of apriori weights for troposphere parameters and coordinates. Another reason is orbit relaxation, i.e. estimating an along-track orbit parameter, also slightly degrades the results for “good” days. This, however, will most likely give similar results.

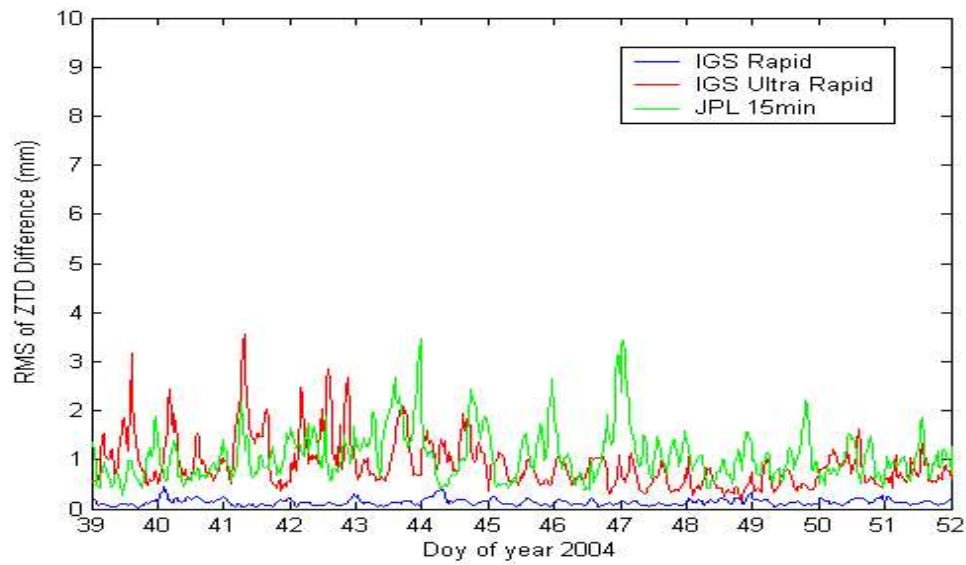


Figure 7.5 RMS of ZTD difference between the results from different orbits using the iterative satellite rejection method.

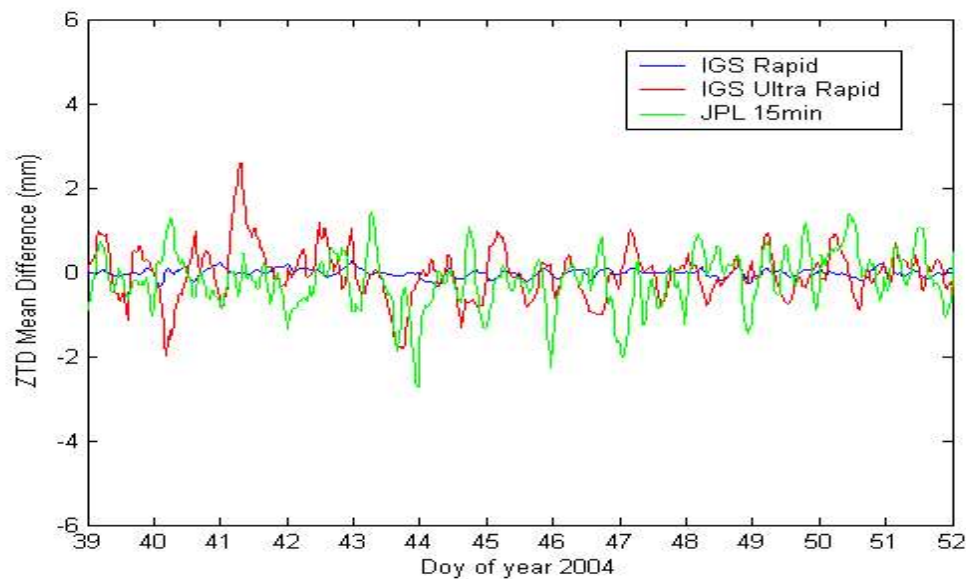


Figure 7.6 Mean difference between ZTD estimates from different orbits using the iterative satellite rejection method.

7.4 Data Processing Techniques

Another important issue for NRT processing is to achieve a good balance between data processing time and the quality of the results. The shorter the data session length is, the shorter the processing time is required to produce GPS tropospheric estimates. However the effect of reducing the processing time has to be balanced against the effect on the accuracy of the GPS tropospheric estimates.

There are two mainly strategies used in NTR data processing: one is the “sliding-window” technique and the other is the “stacking” technique, which are used by GAMIT and Bernese software respectively:

- ***Sliding-window***: This strategy processes one segment (window or session) of GPS data at a time. One segment may contain several hours of GPS data of the whole data set, called “window length”. Every hour, one hour of GPS data is removed from the beginning of the window and another hour of data is added to the end of the window. Thus processing window is advanced by one hour every hour, enabling the provision of the last hour of GPS estimates every hour.
- ***Stacking***: This strategy is to process the GPS data in 1-hour segments. The normal equation file for the 1-hour analysis is stored for later use. Then the normal equation files from the last 24 1-hour solutions are stacked to obtain the equivalent of a 24-hour GPS solution. The main reason for using this stacking technique, rather than re-processing many hours of data every hour, is the significant saving in CPU time.

In our NRT data processing using the GAMIT software, the sliding-window strategy is used.

In order to assess the accuracy of the ZTD estimates against the processing time, GPS data sets of 10 days length collected from the ARGN were processed using the sliding-window strategy with different window lengths and the IGS final orbits. We used the QUT supercomputer, which has 60 processors and 30G memory², to process the GPS data. The solutions from 24 hours of continuous GPS data were used as the reference solution. The comparison results are presented in Table 7.6 and Figure 7.6. From Table 7.6 we can see that when the window length varies from 3h to 24h, the RMS agreement with the 24h reference solution is improved gradually, but the processing time increases rapidly. The ZTD RMS results from window length of less than 8h are about 8mm, which is not accurate enough. Using a 12h window length, the RMS agreement with the 24h reference solution is approximately 4.5mm and the time taken to do the processing is reduced to 40%. This result is also not good enough for practical

² More information about QUT supercomputer can be found at <http://its.qut.edu.au/hpc/hardware/sirius.jsp>

application although it does dramatically saves on processing time.

The possible reason for this result is that the GPS stations in the ARGN are spaced widely apart. This requires longer data sessions to ensure high accuracy solutions. For medium-scale GPS networks (several hundred kilometres), the 12h window length might be appropriate choice, which balances the processing time and accuracy of PWV estimates for meteorological applications.

Table 7.6 Comparison of computing burden and accuracy of ZTD estimates for different session length.

window length (hours)	RMS (mm)	STD (mm)	Mean (mm)	processing time (min)
3	13.69	13.59	-1.60	5.72
4	12.22	12.17	-1.06	6.89
6	12.19	12.19	0.22	9.83
8	8.09	8.09	-0.05	13.40
12	4.49	4.38	-0.96	20.85
24	0	0	0	52.40

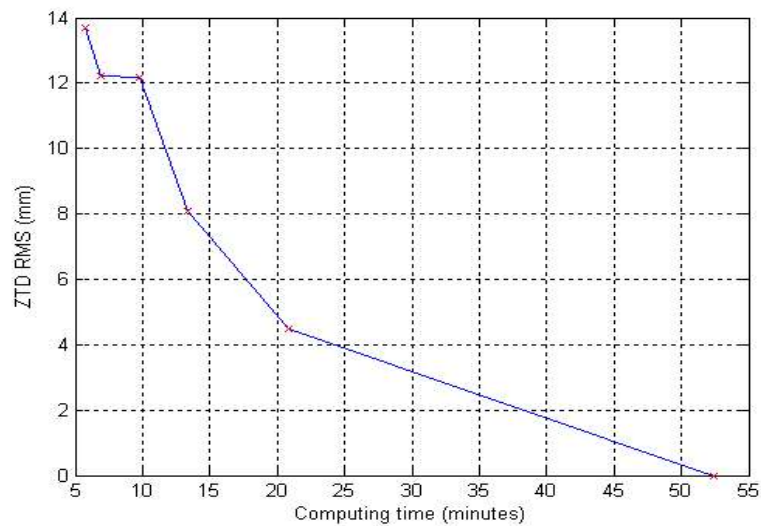


Figure 7.7 RMS difference versus processing time.

7.6. Conclusion

The requirements from the meteorological community are that GPS data should be processed in near-real-time with a latency about 1 or 2 hours or less. An investigation into the use of IGS ultra rapid orbits and JPL 15min orbits for

processing GPS data for near-real-time applications has shown that the orbits are suitable as long as an assessment of the orbital accuracy of each satellite is made before use. This is accomplished through an iteration approach, such as suggested by *Ge et al* [2000]. Low accuracy satellites must be identified, and removed or down-weighted in the GPS data processing in order to produce reliable tropospheric estimates. A sliding-window processing strategy has also been examined in terms of the effect of various processing window lengths on the accuracy of the tropospheric estimates and the time taken to process the data. Finally, based on the near real time data processing techniques discussed above, together with the slant water vapour estimation techniques discussed in Chapter 6, an operational NRT GPS water vapour observing system could be developed for meteorological applications.

Chapter 8

Conclusions and Recommendations

Ground-based GPS Meteorology is a very promising technology, which could significantly improve numerical weather and storm prediction, as well as benefit climate applications. The theory and practice of ground-based GPS water vapour estimation was systematically discussed and demonstrated through various experiments in this research. This is the first attempt to systematically investigate ground-based GPS Meteorology issues in Australia.

For GPS water vapour estimation in Australia:

- There are no meteorological sensors at most GPS sites. The research has developed a methodology for GPS PWV estimation using interpolated surface meteorological data from AWS stations and experimentally demonstrated its feasibility. This could save significant cost by not requiring the installation of meteorological sensors.
- Most GPS sites are located along the coast or on islands. This research studied the ocean loading effects and its impact on GPS-PWV estimates. The daily peak-to-peak vertical displacements could reach 10cm. Thus ocean loading modelling must be properly implemented for GPS-PWV estimation.
- This research takes advantage of the currently operating GPS reference network and Automatic Weather Stations in Australian for water vapour estimation. This would add significant extra value to these existing infrastructures.

Two challenges for operational GPS water vapour estimation have been successfully addressed in this research.

- The algorithms for Slant Water Vapour (SWV) estimation have been developed and demonstrated. Compared to PWV solutions, SWV solutions have higher temporal and spatial resolution and are more useful for meteorological applications.
- Near-real-time GPS water vapour estimation was investigated. The orbit

quality control strategies and sliding-window GPS data processing techniques have been implemented and tested.

Based on these investigations, an operational NRT GPS water vapour observing system can be implemented.

Scope and Limitation of the Research, Future Directions

This thesis focuses on water vapour estimation from ground-based GPS meteorology. The disadvantage of this technology is that it does not provide atmospheric profile information, presently does not provide data over the oceans, and most importantly GPS results have not yet yielded consistent and strong positive impact on weather models. In order to obtain information on the atmospheric profile, GPS slant observations have to be combined in tomographic or data assimilation analysis. Since low elevation GPS observations contain the most atmospheric information, improved mapping functions are needed. Water vapour estimation using GPS receivers on moving platforms such as cars or ships is more challenging than for static networks. However enhanced algorithms may allow obtaining estimates with sufficient accuracy, and thereby extending the scope of GPS Meteorology considerably. This would be a challenging research objective for future study.

Another interesting perspective for GPS Meteorology can be seen in the radio occultation technique: A low-earth orbiting satellite receives GPS signals during an occultation event and can determine the atmospheric bending angle that can be used to derive the vertical refractivity profile in the stratosphere and the upper troposphere, and may thereby improve the numerical weather models. Quite a number of such LEO missions are planned and some have already been realized, so that even an operational use of the radio occultation method may become reality in the near future.

References

- Alber, C., R. Ware, C. Rocken and J. Braun (1997). "GPS surveying with 1 mm precision using corrections for atmospheric slant path delay." Geophysical Research Letters 24(15): 1859-1862.
- Alber, C., R. Ware, C. Rocken and J. Braun (2000). "Obtaining single path phase delays from GPS double differences." Geophysical Research Letters 27(17): 2661-2664.
- Agnew, D. C. (1996). "SPOTL: Some programs for ocean-tide loading." SIO Ref. Ser. 96-8: 35, Scripps Inst. of Oceanogr., La Jolla, Calif.
- Bai, Z. and Feng, Y., (2002) "Accuracy Assessment for GPS Water Vapor Estimation Using Surface Meteorological Data from Automatic Weather Stations in Australia", 2002 international Symposium on GPS/GNSS, Wuhan, China.
- Bai, Z. and Feng, Y. (2003a). "GPS Water Vapor Estimation Using Hourly Meteorological Data from Australian Automatic Weather Stations." Australian International Aerospace Congress 2003, Brisbane, Australia.
- Bai, Z. and Feng, Y. (2003b). "Measuring Ocean Loading And Its Effects On GPS Derived Precipitable Water Vapor: A Case Study for Australian regional GPS Network Sites." the 6th International Conference on Satellite Navigation Technology, Melbourne, Australia.
- Baker, H.C., A.H. Dodson, N.T. Penna, M. Higgins and D. Offiler (2001). "Ground-based GPS water vapour estimation: potential for meteorological forecasting." Journal of Atmospheric and Solar-Terrestrial Physics 63(12): 1305-1314.
- Baker T. F., Curtis D. J. and Dodson AH (1995). "Ocean tide loading and GPS." GPS World 6(3): 54-59.
- Bean, B. R. and E. J. Dutton (1966). "Radio Meteorology." National Bureau of Standards Monograph 92: 435, US Department of Commerce.
- Berbeneva, N.A., V.E. Kunitsyn, O.G. Razinkov and V.I. Zakharov (2001). "Atmospheric sounding by ground-based and space-based systems." Physics and Chemistry of the Earth, Part A: Solid Earth and Geodesy 26(3): 131-138.
- Beutler, G., Rothacher, M., Schaer, S., Springer, T.A., Kouba, J. and Neilan, R.E. (1999). "The International GPS Service (IGS): An interdisciplinary service in

- support of earth sciences.” Advances in Space Research 23(4): 631-653.
- Bevis M., S. Businger, TA Herring, C. Rocken, R.A. Anthes and RH Ware (1992). “GPS meteorology: remote sensing of atmospheric water vapor using the global positioning system.” Journal of Geophysical Research 97(D14): 15,787-15,801.
- Bevis, M., S. Businger, S. Chiswell, TA Herring, R. A. Anthes, C. Rocken, and RH Ware (1994). “GPS meteorology: mapping zenith wet delays onto precipitable water.” Journal of Applied Meteorology 33(3): 379-386.
- Black, H. D., (1978). “An easily implemented algorithm for the tropospheric range correction”, Journal of Geophysical Research 83(4): 1825-1828.
- Black, H. D. and A. Eisner (1984). “Correcting satellite Doppler data for tropospheric effects”, Journal of Geophysical Research 89(D2): 2616-2626.
- Blewitt, G. (1990). “An Automated Editing Algorithm for GPS Data.” Geophys. Res. Lett. 17(3): 199-202, March.
- Bock, O. and E. Doerflinger (2001). “Atmospheric modeling in GPS data analysis for high accuracy positioning.” Physics and Chemistry of the Earth, Part A: Solid Earth and Geodesy 26(6-8): 373-383.
- Bock Y, Nikolaidis RN, de Jonge PJ and Bevis M (2000). “Instantaneous geodetic positioning at medium distances with the global positioning system.” J Geophys Res 105: 28,223–28,253.
- Bonforte, A., A. Ferretti, C. Prati, G. Puglisi and F. Rocca (2001). “Calibration of atmospheric effects on SAR interferograms by GPS and local atmosphere models: first results.” Journal of Atmospheric and Solar-Terrestrial Physics 63(12): 1343-1357.
- Borbas, E. (1998). “Derivation of precipitable water from GPS data: an application to meteorology.” Physics and Chemistry of the Earth 23(1): 87-90.
- Boucher C, Altamimi Z and Sillard P (1999). “Results and analysis of the ITRF97.” IERS Tech note 27, Int Earth Rotation Service, Paris
- Bouma, H. R. and B. Stoew (2001). “GPS observations of daily variations in the atmospheric water vapor content.” Physics and Chemistry of the Earth, Part A: Solid Earth and Geodesy 26(6-8): 389-392.
- Braun, J., C. Rocken and R. Ware (2001). “Validation of line-of-sight water vapor measurements with GPS.” Radio Sci. 36(3): 459-472.
- Brunner, F. K. and S. McCluskey (1991). “Tropospheric zenith delay parameters:

- how many should be estimated in GPS processing?" Australian Journal of Geodesy, Photogrammetry & Surveying 55: 67-75.
- Brunner, F. K. and P. Tregoning (1994). "Tropospheric propagation effects in GPS height results using meteorological observations." Australian Journal of Geodesy, Photogrammetry & Surveying 60: 49-65.
- Brunner, F. K. and W. M. Welsch (1993). "Effect of the troposphere on GPS measurements." GPS World 4(1): 42,44,46,48,50-51.
- Businger, S., SR Chiswell, M. Bevis, J. Duan, RA Anthes, C. Rocken, RH Ware, M. Exner, T. Van Hove, and FS Solheim (1996). "The promise of GPS in atmospheric monitoring." Bulletin - American Meteorological Society 77(1): 5-18.
- Chao, C.C. (1972), "A Model for Tropospheric Calibration from daily Surface and Radiosonde Balloon Measurements", Technical Report: 391-350, Jet Propulsion Laboratory, Pasadena, California.
- Coops, N. C. and R. H. Waring (2001). "The use of multiscale remote sensing imagery to derive regional estimates of forest growth capacity using 3-PGS." Remote Sensing of Environment 75(3): 324-334.
- Cucurull, L., B. Navascues, G. Ruffini, P. Elosegui, A. Rius and J. Vila (2000). "The use of GPS to validate NWP systems: The HIRLAM model." Journal of Atmospheric and Oceanic Technology 17(6): 773-787.
- Dabberdt, W. F. and T. W. Schlatter (1996). "Research opportunities from emerging atmospheric observing and modeling capabilities." Bulletin - American Meteorological Society 77(2): 305-323.
- Dach R. and Dietrich R. (2000). "Influence of the ocean loading effect on GPS derived precipitable water vapor." Geophys Res Lett 27(18): 2953-2957.
- Davis, J. L., T. A. Herring, I. I. Shapiro, A. E. E. Rogers and G. Elgered (1985). "Geodesy by Radio Interferometry: Effects of Atmospheric Modeling Errors on Estimates of Baseline Length." Radio Sci. 20(6): 1593-1607.
- Davis, J. L. (2001). "Atmospheric water-vapor signals in GPS data: synergies, correlations, signals and errors." Physics and Chemistry of the Earth, Part A: Solid Earth and Geodesy 26(6-8): 513-522.
- Davis, J. L. and G. Elgered (1998). "The spatio-temporal structure of GPS water-vapor determinations." Physics and Chemistry of the Earth 23(1): 91-96.
- Delacourt, C., P. Briole and J. Achache (1998). "Tropospheric corrections of SAR

- interferograms with strong topography. Application to Etna.” Geophysical Research Letters 25(15): 2849-2852.
- Dick, G., G. Gendt and C. Reigber (2001). “First experience with near real-time water vapor estimation in a German GPS network.” Journal of Atmospheric and Solar-Terrestrial Physics 63(12): 1295-1304.
- Dodson, A. H. and H. C. Baker (1998). “Accuracy of orbits of GPS atmospheric water vapour estimation.” Physics and Chemistry of the Earth 23(1): 119-124.
- Dodson, A.H., W. Chen, N.T. Penna and H.C. Baker (2001). “GPS estimation of atmospheric water vapour from a moving platform.” Journal of Atmospheric and Solar-Terrestrial Physics 63(12): 1331-1341.
- Dorsel, D.S., and T. LaBreche (1997). http://www.cee.vt.edu/program_areas/environmental/teach/smprimer/kriging/kriging.html
- Dousa, J. (2001). “The impact of ultra-rapid orbits on precipitable water vapor estimation using a ground GPS network.” Physics and Chemistry of the Earth, Part A: Solid Earth and Geodesy 26(6-8): 393-398.
- Dousa, J. (2001). “Towards on operational near real-time precipitable water vapor estimation.” Physics and Chemistry of the Earth, Part A: Solid Earth and Geodesy 26(3): 189-194.
- Dousa, J. and L. Mervart (2001). “On hourly orbit determination.” Physics and Chemistry of the Earth, Part A: Solid Earth and Geodesy 26(6-8): 555-560.
- Dragert F, Janes TS and Lambert A (2000). “Ocean loading corrections for continuous GPS: a case study at the Canadian coastal site Holberg.” Geophys Res Lett 27(14): 2045–2048.
- Duan, J., M. Bevis, P. Fang, Y. Bock, S. Chiswell, S. Businger, C. Rocken, F. Solheim, T. VanHove, R. Ware, S. Mc Clusky, TA Herring and RW King (1996). “GPS meteorology: direct estimation of the absolute value of precipitable water.” Journal of Applied Meteorology 35(6): 830-838.
- Dziewonski A. and Anderson DL (1981). “Preliminary reference Earth model.” Phys Earth Planet Int 25: 297–356.
- Eanes, R. J. (1994). “Diurnal and semidiurnal tides from TOPEX/POSEIDON altimetry.” Eos Trans. AGU, 75(16):108.
- Eanes R. J. and Shuler A (1999). “An improved global ocean tide model from TOPEX/Poseidon altimetry: CSR4.0.” in European Geophysical Society, 24th

General Assembly, The Hague.

- Egbert, G.D., Bennett, A.F., and Foreman, M. G.G. (1994). "TOPEX/POSEIDON tides estimated using a global inverse model." *J. Geophys. Res.*, 99(C12): 24,821-24,852.
- Egbert, G.D. and Erofeeva, L.(2002). "Efficient inverse modeling of barotropic ocean tides." *Journal of Atmospheric and Oceanic Technology*. 19.
- Elgered G., JM Johansson, BO Ronnang, and JL Davis (1997). "Measuring regional atmospheric water vapor using the Swedish permanent GPS network." *Geophysical Research Letters* 24(21): 2663-2666.
- Elosegui, P., A. Rius, JL Davis, G. Ruffini, SJ Keihm, B. Burki and LP Kruse, (1998). "An experiment for estimation of the spatial and temporal variations of water vapor using GPS data." *Physics and Chemistry of the Earth* 23(1): 125-130.
- Emardson, T.R., G. Elgered and J.M. Johansson (1998). "Three months of continuous monitoring of atmospheric water vapor with a network of Global Positioning System." *Journal of Geophysical Research* 103(D2): 1807-1820.
- Fang, P., M. Bevis, Y. Bock, S. Gutman and D. Wolf (1998). "GPS meteorology: reducing systematic errors in geodetic estimates for zenith delay." *Geophysical Research Letters* 25(19): 3583-3586.
- Fang, P., G. Gendt, T. Springer and T. Mannucci (2001). "IGS near real-time products and their applications", *GPS Solutions* 4(4): 2-8.
- Farrell W.E. (1972). "Deformation of the Earth by surface load". *Rev Geophys Space Phys* 10(3): 761-797.
- Feng, D. D. and B. M. Herman (1999). "Remotely sensing the earth's atmosphere using the Global Positioning System (GPS)-the GPS/MET data analysis." *Journal of Atmospheric and Oceanic Technology* 16(8): 989-1002.
- Feng Y, Bai Z, Fang P. and Williams A. (2003) "GPS water vapour experimental results from observations of the Australian Regional GPS network". *Geomatics Res. Australasia* 79: 21-41.
- Foelsche, U. and G. Kirchengast (2001). "A new "geometric" mapping function for the hydrostatic delay at GPS frequencies." *Physics and Chemistry of the Earth, Part A: Solid Earth and Geodesy* 26(3): 153-157.
- Garrison, J. L. and S. J. Katzberg (2000). "The Application of Reflected GPS Signals to Ocean Remote Sensing." *Remote Sensing of Environment* 73(2):

175-187.

- Ge M., Calais E. and Haase J. (2000). "Reducing satellite orbit error effects in near real-time GPS zenith tropospheric delay estimation." Geophysical Research Letters 27(13): 1915-1918.
- Ge, M., E. Calais and J. Haase (2001). "Automatic orbit quality control for near real-time GPS zenith tropospheric delay estimation." Physics and Chemistry of the Earth, Part A: Solid Earth and Geodesy 26(3): 177-181.
- Gelb, A. (Ed) (1996). "Applied Optimal Estimation." MIT Press: 374, 14th printing.
- Gendt, G., G. Dick, A. Rius and P. Sedo (2001). "Comparison of software and techniques for water vapor estimation using German near real-time GPS data." Physics and Chemistry of the Earth, Part A: Solid Earth and Geodesy 26(6-8): 417-420.
- Gendt, G., C. Reigber and G. Dick (2001). "Near real-time water vapor estimation in a German GPS network-first results from the ground program of the HGF GASP project." Physics and Chemistry of the Earth, Part A: Solid Earth and Geodesy 26(6-8): 413-416.
- Glaus, R., B. Bürki and HG Kahle (1995). "Recent results of water vapor radiometry in assessing vertical lithospheric movements by using space geodetic techniques." Journal of Geodynamics 20(1): 31-39.
- Gore Albert (1999). Vice President of the United States, "New Global Positioning System Modernization Initiative.", The White House, Office of the Vice President, Public Announcement on the Global Positioning System, Washington, DC, January 25, 1999.
- Gregorius, T. L. H. and G. Blewitt (1999). "Modeling weather fronts to improve GPS heights: A new tool for GPS meteorology?" Journal of Geophysical Research B: Solid Earth 104(7): 15,261-15,279.
- Guldner, J. (2001). "Validation of integrated water vapor using independent measurement techniques." Physics and Chemistry of the Earth, Part A: Solid Earth and Geodesy 26(6-8): 427-431.
- Guo Y. R., Kuo Y. H., Dudhia J., Parsons D. and Rocken C. (2000). "Four-dimensional variational data assimilation of heterogeneous mesoscale observations for a strong convective." Monthly Weather Review 128(3): 619-643.

- Haase, J., H. Vedel, M. Ge and E. Calais (2001). "GPS zenith tropospheric delay (ZTD) variability in the Mediterranean." Physics and Chemistry of the Earth, Part A: Solid Earth and Geodesy 26(6-8): 439-443.
- Hanssen, R, I. Weinreich, S. Lehner and A. Stoffelen (2000). "Tropospheric wind and humidity derived from spaceborne radar intensity and phase observations." Geophysical Research Letters 27(12): 1699-1702.
- Hendy, M. R. and F. K. Brunner (1990). "Modelling the zenith wet component of the tropospheric path delay for microwaves." Australian Journal of Geodesy, Photogrammetry & Surveying 53: 53-73.
- Herring, T. A., J. L. Davis and I. I. Shapiro (1990), "Geodesy by Radio Interferometry: The Application of Kalman Filtering to the Analysis of Very Long Baseline Interferometry Data." Journal of Geophysical Research 95 (B8): 12,561-12,581.
- Herring, T. A. (1992). "Modeling Atmospheric Delays in the Analysis of Space Geodetic Data." Proc. the Symposium: Refraction of the Transatmospheric Signals in Geodesy, the Hague, the Netherlands.
- Herring T. A. and King R. W. (1996). "GPS meteorology: direct estimation of the value of precipitable water." J Appl Meteorol 35(6): 830–838.
- Higgins, M. (2001). "Progress in 3D-variational assimilation of total zenith delay at the Met Office." Physics and Chemistry of the Earth, Part A: Solid Earth and Geodesy 26(6-8): 445-449.
- Hocke, K. and A. G. Pavelyev (2001). "General aspect of GPS data use for atmospheric science." Advances in Space Research 27(6-7): 1313-1320.
- Hofmann-Wellenhof, B., H. Lichtenegger and J. Collins (1997). "GPS: Theory and Practice". 4th revised ed., SpringerWien, NewYork.
- Hopfield, H. S. (1971). "Tropospheric effect on electromagnetically measured range: Prediction from surface weather data." Radio Science 6(3): 357-367.
- Ingold, Th., B. Schmid, C. Mätzler, P. Demoulin and N. Kämpfer (2000). "Modeled and empirical approaches for retrieving columnar water vapor from solar transmittance measurements in the 0.72, 0.82 and 0.94 μm absorption bands." Journal of Geophysical Research D: Atmospheres 105 (19): 24,327-24,343.
- Ifadis, I. (1986). "The Atmospheric Delay of Radio Waves: Modeling The Elevation Dependence on a Global Scale". Technical Report No 38L,

Chalmers University of Technology, Gothenburg, Sweden.

- Ifadis, I. (1987), "Contribution to the Study of the Atmospheric Refraction, on Radiowaves Used in Modern Geodetic Techniques in Long Distance Measurements." Thesis Report, Vol. IA'.6, School of Engineering, Faculty of Civil Engineering Thessaloniki.
- Iwabuchi, T., I. Naito, and N. Mannoji (2000). "A comparison of Global Positioning System retrieved precipitable water vapor with the numerical weather prediction data over the Japanese Islands." Journal of Geophysical Research D: Atmospheres 105(4): 4573-4585.
- Jacob, D. (2001). "The role of water vapour in the atmosphere. A short overview from a climate modeller's point of view." Physics and Chemistry of the Earth, Part A: Solid Earth and Geodesy 26(6-8): 523-527.
- Johnsen, K. P. and B. Rockel (2001). "Validation of a regional weather forecast model with GPS data." Physics and Chemistry of the Earth, Part B: Hydrology, Oceans and Atmosphere 26(5-6): 415-419.
- Kimata, F., Y. Hirose and Y. Sasaki. (1993). "Effects of troposphere on horizontal vector of GPS baseline determination." Journal - Geodetic Society of Japan 39(3): 317-319.
- King, R. W. and Y. Bock, (2001) "Documentation of the GAMIT GPS analysis software", V10.03, MIT, Cambridge.
- Kruse, L.P., B. Sierk, T. Springer and M. Cocard (1999). "GPS-Meteorology: Impact of predicted orbits on precipitable water estimates." Geophysical Research Letters 26(14): 2045-2048.
- Kuo, Y. H., X. Zou and W. Huang (1998). "The impact of Global Positioning System data on the prediction of an extratropical cyclone: an observing system experiment." Dynamics of Atmospheres and Oceans 27(1-4): 439-470.
- Kursinski, ER, GA Hajj, WI Bertiger, SS Leroy, T. K. Meehan, L. J. Romans, J. T. Schofield, DJ McCleese, WG Melbourne, CL Thournton, TP Yunck, JR Eyre and R. N. Nagatani (1996). "Initial results of radio occultation observations of Earth's atmosphere using the Global Positioning System." Science 271(5252): 1107-1110.
- Kursinski, E. R. and G. A. Hajj (2001). "A comparison of water vapor derived from GPS occultations and global weather analyses." Journal of Geophysical

Research D: Atmospheres 106(1): 1113-1138.

- Kursinski, ER and Hajj, GA and Hardy, KR and Romans, LJ and Schofield, JT (1995). "Observing tropospheric water vapor by radio occultation using the global positioning system." Geophysical Research Letters 22(17): 2365-2368.
- Kuzyrska, K. and A. Gabryszewska (2001). "Atmospheric water vapour content determined from zenith delay assuming a local model of troposphere." Physics and Chemistry of the Earth, Part A: Solid Earth and Geodesy 26(3): 159-163.
- Le Provost, C., Genco, M. L., Lyard, F., Vincent, P. and Canceil, P. (1994). "Spectroscopy of the world ocean tides from a finite-element hydrodynamic model." J. Geophys. Res. 99(C12):24,777-24,797.
- Le Provost, C., Lyard, F., Molines, J. M., Genco, M. L., and Rabilloud, F. (1997). "A hydrodynamic ocean tide model improved by assimilating a satellite altimeter-derived data set." J. Geophys. Res. 103(C3):5513-5529.
- Lefèvre, F., Lyard, F. H. and LeProvost, C. (2000). "FES98: A new global tide finite element solution independent of altimetry." Geophys. Res. Letters 27 (17):2717-2720,
- Leick, A. (2004). "Satellite GPS Surveying." 3rd ed., Wiley-InterScience.
- Leinen, ST. (1997). "Hochpräzise Positionierung über große Entfernungen und in Echtzeit mit dem Global Positioning System." Deutsche Geodätische Kommission, ISBN 3 76969512 7.
- Li, J. and J. Mao (1998). "The approach to remote sensing of water vapor based on GPS and linear regression T(m) in eastern region of China." Acta Meteorologica Sinica 12(4): 450-458.
- Liou, Y.A., C.Y. Huang and Y.T. Teng (2000). "Precipitable water observed by ground-based GPS receivers and microwave radiometry." Earth, Planets and Space 52(6): 445-450.
- Liou, Y.A., Y.T. Teng, T. van Hove and J.C. Liljegren (2001). "Comparison of precipitable water observations in the near tropics by GPS, microwave radiometer, and radiosondes." Journal of Applied Meteorology 40(1): 5-15.
- Liu, Y. (2000). "Remote Sensing of Atmospheric Water vapour using GPS Data in the Hong Kong region." PhD thesis, Department of Land surveying & Geo-informatics The Hong Kong Polytechnic University. Hong Kong.

- Liu, Y., Y. Chen and HB Iz (2000). "Precision of precipitable water vapor from radiosonde data for GPS solutions." Geomatica 54(2): 171-175.
- McDonald, Keith D. (2002). "The Modernization of GPS: Plans, New Capabilities and the Future Relationship to Galileo." Journal of Global Positioning Systems 1(1):1-17.
- MacDonald, A., Y. Xie, and R. Ware (2001). "Use of a Network of Surface GPS Receivers to Recover Three Dimensional Temperature and Moisture." IAMAS 2001, Innsbruck, Austria.
- MacDonald, A., Y. Xie, and R. Ware (2002). "Diagnosis of Three Dimensional Water Vapor Using Slant Observations from a GPS Network." Mon. Wea. Rev. 130: 386-397.
- MacMillan, D. S. and C. Ma (1998). "Using meteorological data assimilation models in computing tropospheric delays at microwave frequencies." Physics and Chemistry of the Earth 23(1): 97-102.
- Mansilla, G. A. and V. H. Rios (1996). "Diurnal and latitudinal behavior of ionospheric delay time of GPS signals in South American stations." Bollettino di Geodesia e Scienze Affini 55(2): 105-118.
- Marini, J.W. (1972). "Correction of Satellite Tracking Data for an Arbitrary Atmospheric Profile", Radio Science 7: 223-231.
- Marquardt, C., K. Labitzke, C. Reigber, T. Schmidt and J. Wickert (2001). "An assessment of the quality of GPS/MET radio limb soundings during February 1997." Physics and Chemistry of the Earth, Part A: Solid Earth and Geodesy 26(3): 125-130.
- Matsumoto, K., Ooe, M., Sato, T., and Segawa, J. (1995). "Ocean tide model obtained from TOPEX/POSEIDON altimetry data." J. Geophys. Res., 100 (C12):25,319-25,330
- Matsumoto, K., Takanezawa, T. and Ooe, M. (2000). "Ocean Tide Models Developed by Assimilating TOPEX/POSEIDON Altimeter Data into Hydrodynamical Model: A Global Model and a Regional Model Around Japan." J. of Oceanog 56: 567-581.
- Matsumoto, K., T. Sato, T. Takanezawa and M. Ooe (2001). "GOTIC2: A Program for Computation of Oceanic Tidal Loading Effect." J. Geod. Soc. Japan 47: 243-248.
- Mendes, V. B. and R. B. Langley (1994). "A Comprehensive Analysis of Mapping

- Functions Used in Modeling Tropospheric Propagation Delay in Space Geodetic Data". KIS94, Proc. of the Int. Symp. on Kinematic Systems in Geodesy, Geomatics and Navigation: 87-98, The University of Calgary, Calgary, Alberta.
- Mendes, V. B. and R. B. Langley (1998). "Optimization of Tropospheric Delay Mapping Function Performance for High-Precision Geodetic Applications." Proc. DORIS Days, April 27-29, Toulouse, France.
- Mendes, V. B. (1998). "Modeling the neutral-atmosphere propagation delay in radiometric space techniques." Ph.D. Thesis:353, Univ. New Brunswick.
- Mendes, V. B. and R. B. Langley (2000). "An analysis of high-accuracy tropospheric delay mapping functions." Physics and Chemistry of the Earth, Part A: Solid Earth and Geodesy 25(12): 809-812.
- Miyazaki S., Tsuji H., Hatanaka Y., Abe Y., Yoshimura A., Kamada K., Kobayashi K., Morishita H. and Iimura Y. (1996). "Establishment of the nationwide GPS array (GRAPES) and its initial results on the crustal deformation of Japan." Bull. geograph. Surv. Inst 135:27-41.
- Moen, R., Pastor, J. and Cohen, Y. (1997). "Accuracy of GPS telemetry collar locations with differential correction." Journal of Wildlife Management 61 (2): 530-539.
- Murakami, M. (1996). "Precise determination of the GPS satellite orbits and its new applications - GPS orbit determination at the Survey Institute." Journal - Geodetic Society of Japan 42(1): 1-14.
- Naito, I., Y. Hatanaka, N. Mannoji, R. Ichikawa, S. Shimada, T. Yabuki, H. Tsuji and T. Tanaka, (1998). "Global Positioning System project to improve Japanese weather, earthquake predictions." Eos 79(26): 301+308-311.
- Niell, A. E. (1996). "Global Mapping Functions for the Atmosphere Delay at RadioWavelengths." J. Geophys. Res. 101(B2), 3227-3246.
- NOAA/NASA/USAF (1976). "U.S. Standard Atmosphere." U.S. Government Printing, Washington DC.
- Ohtani, R. and I. Naito (2000). "Comparisons of GPS-derived precipitable water vapors with radiosonde observations in Japan." Journal of Geophysical Research D: Atmospheres 105(22): 26917-26929.
- Owens, J.C. (1967). "Optical refractive index of air: Dependence on pressure, temperature and composition." Applied Optics 6: 51-58.

- Pacione, R., Sciarretta, C., Vespe, f., Faccani, C., Ferretti, R., Fionda, E., Ferraro, C. and Nardi, A. (2001). "GPS metrology: Validation and comparisons with ground-based microwave radiometer and mesoscale model for the GPS permanent stations." Physics and Chemistry of the Earth, Part A: Solid Earth and Geodesy 26(3): 139-145.
- Pany, T., P. Pesec and G. Stangl (2001). "Atmospheric GPS slant path delays and rays tracing through numerical wheather models, a comparison." Physics and Chemistry of the Earth, Part A: Solid Earth and Geodesy 26(3): 183-188.
- Pany, T., P. Pesec and G. Stangl (2001). "Elimination of tropospheric path delays in GPS observations with the ECMWF numerical weather model." Physics and Chemistry of the Earth, Part A: Solid Earth and Geodesy 26(6-8): 487-492.
- Ray, R.D. (1999). "A Glob al Ocean Tide Model From TOPEX/POSEIDON Altimetry: GOT99.2." NASA Technical Memorandum 209-478
- Resch, G. M. (1984). "Water vapor radiometry in geodetic applications." Geodetic refraction. F. K. Brunner, Springer-Verlag: 53-84.
- Rizos, C., Han, S., Chen, H.Y. and Goh, P.C. (1999). "Continuously operating GPS reference station networks: new algorithms and applications of carrier phase-based, medium-range, static and kinematic positioning." In "Quo vadis geodesiaŠ?", Dept. of Geodesy & Geoinformatics, University of Stuttgart, ISSN 0933-2839, 367-378.
- Rocken, C., RH Ware, T. Van Hove, F. Solheim, C. Alber, J. Johnson and MG Bevis (1993). "Sensing atmospheric water vapor with the Global Positioning System." Geophysical Research Letters 20(23): 2631-2634.
- Rocken, C., JM Johnson, JJ Braun, H. Kawawa, Y. Hatanaka and T. Imakiire (2000). "Improving GPS surveying with modeled ionospheric corrections." Geophysical Research Letters 27(23): 3821-3824.
- Rocken, C., T. Van Hove and R. Ware (1997). "Near real-time GPS sensing of atmospheric water vapor." Geophysical Research Letters 24(24): 3221-3224.
- Rothacher, M. and G. Beutler (1998). "The role of GPS in the study of global change." Physics and Chemistry of the Earth 23(9-10): 1029-1040.
- Ruff, C. S. and C. T. Swift (1988). "Atmospheric profiling of water vapour with a 20.5-23.5 GHz autocorrelation radiometer." Remote sensing. Proc. IGARSS '88 symposium, Edinburgh, 1988. 2: 957-960, T. D. Guyenne. Esa Sp-284,

European Space Agency ESTEC Noordwijk.

- Ruffini, G., LP Kruse, A. Rius, B. Burki, L. Cucurull and A. Flores (1999). "Estimation of Tropospheric Zenith delay and gradients over the Madrid area using GPS and WVR data." Geophysical Research Letters 26(4): 447-450.
- Saastamoinen, J. (1973). "Contributions to the theory of atmospheric refraction Part II, Refraction corrections in satellite geodesy." Bulletin Geodesique (107): 13-14.
- Scherneck, H. G. (1991). "A parameterized solid earth tide model and ocean tide loading effects for global geodetic baseline measurements." Geophys. J. Int. 106: 77-694.
- Scherneck, H.-G., Johansson J.M. and Webb, F.H. (2000). "Ocean loading tides in GPS and rapid variations of the frame origin." Geodesy 2000 - The Challenges in the First Decade 121, Schwarz, Springer - Verlag Berlin Heidelberg.
- Schrama, E. J.O. and Ray, R.D. (1994). "A Preliminary Tidal Analysis Of TOPEX/POSEIDON Altimetry." J. Geophys. Res. 99(C12):24,799-24,808.
- Schwiderski, E.W. (1980). "On Charting Global Ocean Tides." Rev. Geophys. Space Phys. 18(1):243-268.
- Sierk, B., Bürki, B., Becker-Ross, H., Florek, S., Neubert, R., Kruse, LP and HG Kahle (1997). "Tropospheric water vapor derived from solar spectrometer, radiometer, and GPS measurements." Journal of Geophysical Research 102 (B10): 22411-22424.
- Silvestrin, PJ Baptista and P. Hoeg (1998). "Radio occultation data analysis: from planetary atmosphere sounding to operational meteorology." The 32nd ESLAB Symposium on remote sensing methodology for Earth observation and planetary exploration: 179-187, E. Attema. Netherlands, Estec.
- Smith, E.K., and S. Weitraub, (1953), "The constants in the equation for atmospheric refractive index at radio frequencies." Proceedings of the I.R.E. 41: 1035-1037.
- Solheim, F.S., J. Vivekanandan, R.H. Ware and C. Rocken, C. (1999). "Propagation delays induced in GPS signals by dry air, water vapor, hydrometeors, and other particulates." Journal of Geophysical Research D: Atmospheres 104(8): 9663-9670.
- Springer, T. A. and U. Hugentobler (2001). "IGS ultra rapid products for (near-)

- real-time applications.” Physics and Chemistry of the Earth, Part A: Solid Earth and Geodesy 26(6-8): 623-628.
- Stoew, B., P. Jarlemark, J.M. Johansson and G. Elgered (2001). “Real-time processing of GPS data delivered by SWEPOS.” Physics and Chemistry of the Earth, Part A: Solid Earth and Geodesy 26(6-8): 493-496.
- Stolz, A., Masters, EG and Rizos, C. (1984). “Determination of GPS satellite orbits for geodesy in Australia.” Australian Journal of Geodesy, Photogrammetry & Surveying 40: 41-52.
- Tanaka T., Ohba M., Hirahara K. and Nakamura K. (1993). “Preliminary results of water vapor radiometer observations for correction of excess path delay on precise by GPS.” Journal - Geodetic Society of Japan 39(2): 97-105.
- Thayer, G.D. (1974). “An Improved Equation for the Radio Refractive Index of Air.” Radio Science 9: 803-807.
- Tralli, D., T. Dixon and S. Stephens (1988). “Effect of wet tropospheric path delays on estimation of geodetic baselines in the Gulf of California using the Positioning System (Mexico).” Journal of Geophysical Research 93(B6): 6545-6557.
- Tregoning P., R. Boers and D. O’Brien (1999). “Accuracy of absolute precipitable water vapor estimates from GPS observations.” Journal of Geophysical Research D: Atmospheres 103(D22): 28,701-28,710.
- Teunissen, P.J.G. and Kleusberg, A.(1998). “GPS for Geodesy”. Delf University of Technology. 2nd edition.
- Vedel, H., K.S. Mogensen and X.Y. Huang (2001). “Calculation of zenith delays from meteorological data comparison of NWP model, radiosonde and GPS delays.” Physics and Chemistry of the Earth, Part A: Solid Earth and Geodesy 26(6-8): 497-502.
- Wackernagel, H. (1998): “Multivariate Geostatistics.” Springer-Verlag: 291.
- Ware, R., F. Solheim, C. Rocken, T. Van Hove, C. Alber and J. Johnson (1993). “Pointed water vapor radiometer corrections for accurate Global Positioning System surveying.” Geophysical Research Letters 20(23): 2635-2638.
- Ware, R., M. Exner, D. Feng, M. Gorbunov, K. Hardy, B. Herman, W. Kuo, T. Meehan, W. Melbourne, C. Rocken, W. Schreiner, S. Sokolovskiy, F. Solheim, X. Zou, R. Anthes and S. Businger (1996). “GPS sounding of the

- atmosphere from low Earth orbit: preliminary results.” Bulletin - American Meteorological Society 77(1): 19-40.
- Ware, R., D. Fulker, S. Stein, D. Anderson, S. Avery, R. Clark, K. Droegemier, J. Kuettnner, J. Minster and S. Sorooshian (2001). “Real-time national GPS networks for atmospheric sensing.” Journal of Atmospheric and Solar-Terrestrial Physics 63(12): 1315-1330.
- Watkins, M.M. and Eanes, R.J. (1997). “Observations of tidally coherent diurnal and semidiurnal variations in the geocenter.” Geophys. Res. Lett. 24(17): 2231-2234.
- Wickwar, V. B. and H. C. Carlson (1999). “Ionospheric and thermospheric couplings: vertical, latitudinal and longitudinal.” Journal of Atmospheric and Solar-Terrestrial Physics 61(1-2): 141-152.
- Williams, S., Y. Bock and P. Fang (1998). “Integrated satellite interferometry: Tropospheric noise, GPS estimates and implications for interferometric aperture radar products.” Journal of Geophysical Research B: Solid Earth 103(11): 27,051-27,067.
- Wolfe, D. E. and S. I. Gutman (2000). “Developing an operational, surface-based, GPS, water vapor observing system for NOAA: Network design and results.” Journal of Atmospheric and Oceanic Technology 17(4): 426-440.
- Yan, H., D. Huang and C. Huang (1999). “Sequential atmospheric profiles near a fixed location derived from GPS-LEO occultation measurements.” Geophysical Research Letters 26(4): 451-453.
- Yang, X., B. Sass, G. Elgered, J.M. Johansson and T.R. Emardson (1999). “A comparison of precipitable water vapor estimates by an NWP simulation and GPS observations.” Journal of Applied Meteorology 38(7): 941-956.
- Zheng, Y. (2004). “Interpolating Residual Zenith Tropospheric Delays for Improved Wide Area Differential GPS Positioning”. ION GNSS 2004, September 21-24, Long Beach Convention Center, Long Beach, California.
- Zumberge, J. F., M. B. Heflin, D. C. Jefferson and M. M. Watkins (1997). “Precise point positioning for the efficient and robust analysis of GPS data from large networks.” Journal of Geophysical Research 102: 5005-5017.

Appendix A

Useful Meteorological Constants and Equalities

Table A.1 Some useful meteorological constants and equalities.

Constants	Symbol	Standard Unit	Conversion
Absolute temperature	T	Kelvin (K)	K = Celsius degree + 273.16 1 mbar = 1 hPa = 100 Pa
Water vapour pressure	e	Millibars (mbar)	1 Pascal (Pa) = 1 Newton / m ² 1 Bar (b) = 1000 mbar
Specific gas constant for water vapour	R_v	J/kg/K	1 J = 1 Newton·m = 1 kg·m ² /sec ²
Density of water vapour	ρ_v	Kg/m ³	1 Kg/m ³ = 10 ⁻³ g/cm ³
Universal gas constant	R_0	J/ mol/K	$R_0 = 8.31434$ J/ mol/K
Molar weight of dry air	M_d	Kg/kmol	$M_d = 28.9644$
Molar weight of wet air	M_w	Kg/kmol	$M_w = 18.0152$

Table A.2 The empirical values and uncertainties (standard errors) for the atmospheric refractivity constants k_1 , k_2 and k_3 (Bevis, 1994).

	k_1		k_2		k_3	
Reference	Value	Error	Value	Error	Value	Error
	$K \cdot mbar^{-1}$	$K \cdot mbar^{-1}$	$K \cdot mbar^{-1}$	$K \cdot mbar^{-1}$	$10^5 K^2 \cdot mbar^{-1}$	$10^5 K^2 \cdot mbar^{-1}$
Smith and Weintraub (1953)	77.607	0.013	71.60	8.50	3.747	0.031
Thayer (1974)	77.604	0.014	64.79	0.08	3.776	0.004
Hasagawa and Stokesbury (1975)	77.600	0.032	69.40	0.15	3.701	0.003
Present study	77.600	0.050	70.40	2.20	3.739	0.012

Appendix B

ITRF 2000 Coordinates for ARGN Stations

Site	X (m)	Y (m)	Z (m)	B	L	Ellipsoid Height (m)	AHD Height* (m)
ALIC	-4052051.8800	4212836.1099	-2545105.7901	-23° 40' 12.43886"	133° 53' 7.85303"	603.2653	587.643
CAS1	-901776.1616	2409383.4124	-5816748.4309	-66° 17' 0.09183"	110° 31' 10.94050"	22.4600	40.889
CEDU	-3753472.2849	3912741.0004	-3347960.8212	-31° 52' 0.00946"	133° 48' 35.38068"	144.7605	153.284
COCO	-741950.0803	6190961.6282	-1337768.5439	12° 11' 18.06266"	96° 50' 2.27877"	-35.2669	N/A**
DARW	-4091358.8388	4684606.7397	-1408580.4059	12° 50' 37.35103"	131° 7' 57.85302"	125.1282	73.933
DAV1	486854.5489	2285099.2998	-5914955.6898	68° 34' 38.36169"	77° 58' 21.40925"	44.4085	27.874**
HOB2	-3950071.4009	2522415.1934	-4311638.3228	42° 48' 16.97851"	147° 26' 19.43939"	41.0671	44.756
JAB1	-4236442.8411	4559929.5989	-1388624.5831	12° 39' 31.86754"	132° 53' 38.02470"	82.1544	26.667
KARR	-2713832.3061	5303935.0991	-2269514.9621	20° 58' 53.16303"	117° 5' 49.87859"	109.1539	115.902
MAC1	-3464038.5198	1334172.7813	-5169224.3053	54° 29' 58.31670"	158° 56' 9.00133"	-6.7669	12.891**
MAW1	1111287.1675	2168911.2784	-5874493.6018	67° 36' 17.15910"	62° 52' 14.57713"	59.1442	32.473**
STR1	-4467102.4723	2683039.4967	-3666949.7514	35° 18' 55.93108"	149° 0' 36.18435"	800.0011	780.860
TID1	-4460996.2318	2682557.0864	-3674443.5980	35° 23' 57.14690"	148° 58' 47.98953"	665.3690	646.322
TOW2	-5054582.7327	3275504.4388	-2091539.6545	19° 16' 9.42109"	147° 3' 20.47026"	88.1318	29.474
YAR2	-2389025.8048	5043316.9306	-3078530.4494	29° 2' 47.60130"	115° 20' 49.11297"	241.3066	266.528

* Australian Height Datum [AHD] Height ** Mean Sea Level [MSL] Height

Appendix C

Ocean Loading Tide Coefficients for ARGN Stations

Ocean Loading Tide coefficients for ARGN stations computed from the Schwiderski model, the CSR 4.0 model, the GOT99.2b model and the NAO.99b model are listed in Table C.1-C.4. Only the eight principal diurnal and semi-diurnal constituents (K1, O1, P1, Q1, M2, S2, N2, and K2) are listed here and the 1066A Earth Model is used in the computation. For each station, 6 lines are up, west and south amplitudes (m) and phases (deg) for the above 8 components.

Table C.1 Ocean Loading Tide Coefficients for ARGN Stations using Schwiderski model.

Site	M2	S2	N2	K2	K1	O1	P1	Q1
ALIC	0.0025	0.0008	0.0007	0.0003	0.0023	0.0026	0.0008	0.0006
	0.0017	0.0008	0.0003	0.0002	0.0018	0.0011	0.0006	0.0002
	0.0004	0.0001	0.0001	0.0000	0.0009	0.0007	0.0003	0.0001
	149.2	-60.7	108.8	-50.4	3.0	7.7	3.7	6.9
	80.4	107.4	71.2	110.0	-170.2	173.3	-170.9	164.0
CAS1	-122.0	76.1	-157.9	82.6	-87.9	-113.2	-88.8	-130.9
	0.0080	0.0039	0.0022	0.0011	0.0113	0.0111	0.0038	0.0024
	0.0028	0.0013	0.0006	0.0004	0.0008	0.0009	0.0003	0.0003
	0.0019	0.0011	0.0005	0.0003	0.0021	0.0021	0.0007	0.0005
	-29.1	23.2	-52.2	25.0	58.9	50.3	58.3	46.6
CEDU	-161.6	-105.3	177.1	-101.6	18.2	-31.4	14.6	-42.6
	-28.4	26.0	-46.5	28.2	64.1	52.9	63.1	49.4
	0.0025	0.0031	0.0006	0.0009	0.0052	0.0052	0.0017	0.0012
	0.0018	0.0010	0.0004	0.0003	0.0017	0.0011	0.0006	0.0002
	0.0006	0.0009	0.0002	0.0003	0.0018	0.0015	0.0006	0.0003
COCO	-171.3	-72.5	83.8	-66.8	45.6	32.7	44.9	27.8
	99.8	111.6	113.0	114.0	-169.7	179.9	-170.2	175.5
	114.2	114.0	168.9	116.9	-111.0	-130.8	-111.9	-141.4
	0.0212	0.0080	0.0048	0.0022	0.0116	0.0077	0.0038	0.0015
	0.0062	0.0030	0.0011	0.0008	0.0018	0.0012	0.0006	0.0002
DARW	0.0021	0.0011	0.0004	0.0003	0.0012	0.0004	0.0004	0.0001
	120.4	143.5	109.4	144.8	-13.4	-23.4	-13.2	-36.7
	-122.9	-81.2	-137.1	-77.5	22.8	5.9	21.3	4.2
	-123.9	-103.6	-130.4	-102.2	99.7	95.0	98.6	114.5
	0.0022	0.0021	0.0006	0.0006	0.0065	0.0051	0.0021	0.0012
DAV1	0.0020	0.0008	0.0004	0.0002	0.0034	0.0020	0.0011	0.0004
	0.0017	0.0007	0.0004	0.0002	0.0008	0.0006	0.0003	0.0001
	36.4	35.9	43.8	36.4	-4.6	-8.8	-4.9	-9.2
	87.1	123.2	71.2	126.3	-170.9	165.7	-172.5	158.5
	-16.2	66.6	-45.4	74.0	-11.1	-22.6	-12.2	-24.6
HOB2	0.0057	0.0032	0.0019	0.0009	0.0091	0.0098	0.0031	0.0022
	0.0003	0.0007	0.0001	0.0002	0.0011	0.0012	0.0004	0.0003
	0.0025	0.0012	0.0006	0.0003	0.0013	0.0018	0.0005	0.0004
	8.3	119.6	-22.6	124.1	77.7	75.4	77.7	73.3
	-46.2	10.9	-129.5	12.6	14.0	-21.8	10.9	-32.6
JAB1	14.3	96.6	-10.9	101.5	90.3	82.8	90.0	78.8
	0.0103	0.0015	0.0026	0.0004	0.0074	0.0067	0.0024	0.0016
	0.0046	0.0019	0.0008	0.0005	0.0011	0.0006	0.0004	0.0001
	0.0010	0.0006	0.0002	0.0002	0.0015	0.0013	0.0005	0.0003
	155.4	-120.4	130.7	-101.6	88.8	56.5	86.8	46.0
KARR	102.0	134.5	101.0	138.8	-162.0	-165.7	-161.8	-171.6
	119.3	104.5	122.5	103.3	-142.8	-162.3	-143.0	-175.3
	0.0046	0.0007	0.0013	0.0002	0.0042	0.0046	0.0014	0.0011
	0.0022	0.0006	0.0005	0.0002	0.0033	0.0020	0.0011	0.0004
	0.0015	0.0008	0.0003	0.0002	0.0007	0.0007	0.0003	0.0001
MAC1	103.3	108.8	78.3	96.1	12.0	7.3	11.7	5.5
	102.3	137.2	85.6	140.6	-171.4	162.5	-173.2	154.1
	53.4	120.6	25.5	125.2	37.7	21.7	35.7	20.6
	0.0163	0.0090	0.0029	0.0026	0.0103	0.0074	0.0034	0.0016
	0.0019	0.0010	0.0003	0.0003	0.0013	0.0008	0.0004	0.0002
MAW1	0.0070	0.0035	0.0013	0.0010	0.0018	0.0012	0.0006	0.0002
	-130.5	-58.4	-162.3	-52.7	-1.9	-8.7	-2.2	-11.6
	-104.9	-50.8	-120.4	-46.2	155.9	146.8	155.7	142.2
	-121.3	-62.6	-148.4	-58.0	-16.5	-42.7	-18.4	-53.7
	0.0133	0.0050	0.0034	0.0013	0.0073	0.0072	0.0024	0.0018
	0.0016	0.0011	0.0002	0.0003	0.0009	0.0008	0.0003	0.0002
	0.0029	0.0008	0.0006	0.0002	0.0015	0.0013	0.0005	0.0003
	-155.3	-124.1	-175.5	-123.6	50.1	27.7	48.7	21.2
	49.3	139.9	20.6	146.3	-79.8	-98.4	-80.9	-106.2
	124.4	144.9	112.7	146.7	170.8	156.7	170.6	149.3
	0.0036	0.0014	0.0013	0.0005	0.0082	0.0090	0.0028	0.0021

Table C.2 Ocean Loading Tide Coefficients for ARGN Stations using CSR 4.0 model.

Site	M2	S2	N2	K2	K1	O1	P1	Q1
ALIC	0.0026	0.0008	0.0007	0.0003	0.0022	0.0025	0.0008	0.0006
	0.0017	0.0008	0.0003	0.0002	0.0016	0.0010	0.0005	0.0002
	0.0004	0.0001	0.0001	0.0000	0.0008	0.0007	0.0003	0.0001
	151.0	-63.6	110.7	-52.9	3.1	7.5	3.8	6.7
	82.8	108.3	74.2	110.7	-170.6	172.8	-171.3	163.5
CAS1	-124.5	90.3	-158.6	93.9	-86.2	-112.7	-87.3	-130.5
	0.0081	0.0039	0.0022	0.0011	0.0113	0.0111	0.0038	0.0024
	0.0027	0.0012	0.0006	0.0003	0.0009	0.0009	0.0003	0.0002
	0.0019	0.0011	0.0005	0.0003	0.0020	0.0021	0.0007	0.0005
	-30.2	22.0	-53.0	23.9	59.0	50.4	58.5	46.3
CEDU	-158.6	-102.2	-179.3	-98.3	26.1	-19.6	23.3	-34.5
	-29.3	24.7	-47.6	26.9	64.6	53.5	63.7	49.8
	0.0026	0.0031	0.0006	0.0009	0.0052	0.0052	0.0017	0.0012
	0.0019	0.0011	0.0004	0.0003	0.0016	0.0010	0.0005	0.0002
	0.0007	0.0010	0.0002	0.0003	0.0017	0.0014	0.0006	0.0003
COCO	-172.1	-73.4	85.1	-67.7	45.8	32.4	45.0	27.8
	100.4	112.9	114.3	115.3	-168.8	-179.4	-169.4	176.7
	111.8	115.2	168.9	118.2	-111.2	-131.3	-112.1	-141.6
	0.0215	0.0081	0.0049	0.0022	0.0117	0.0077	0.0039	0.0015
	0.0055	0.0029	0.0010	0.0008	0.0015	0.0010	0.0005	0.0002
DARW	0.0019	0.0009	0.0004	0.0003	0.0010	0.0004	0.0003	0.0001
	120.3	143.3	109.3	144.6	-13.5	-23.5	-13.4	-37.0
	-121.6	-80.3	-135.5	-76.8	19.9	4.0	18.5	2.7
	-122.9	-100.1	-131.5	-98.5	111.9	117.8	111.2	146.0
	0.0055	0.0024	0.0014	0.0007	0.0074	0.0060	0.0024	0.0013
DAV1	0.0017	0.0006	0.0004	0.0001	0.0037	0.0021	0.0012	0.0004
	0.0020	0.0010	0.0004	0.0003	0.0012	0.0009	0.0004	0.0002
	69.3	79.1	53.4	77.6	6.1	-3.7	5.0	-3.8
	130.3	-177.9	109.6	-173.5	-172.3	164.9	-173.9	159.3
	22.4	93.2	-6.6	98.2	10.8	-7.0	8.7	-5.8
HOB2	0.0060	0.0035	0.0019	0.0010	0.0095	0.0103	0.0033	0.0023
	0.0004	0.0007	0.0001	0.0002	0.0010	0.0011	0.0004	0.0003
	0.0025	0.0011	0.0006	0.0003	0.0013	0.0018	0.0004	0.0004
	8.7	121.4	-22.0	125.7	78.4	75.4	78.4	73.3
	-66.8	6.1	-140.8	8.0	12.0	-25.4	8.7	-36.1
JAB1	13.9	95.4	-11.1	100.5	91.4	83.8	91.2	79.5
	0.0101	0.0016	0.0025	0.0004	0.0072	0.0066	0.0024	0.0016
	0.0042	0.0018	0.0008	0.0005	0.0012	0.0006	0.0004	0.0001
	0.0011	0.0007	0.0002	0.0002	0.0015	0.0013	0.0005	0.0003
	155.1	-121.2	130.5	-103.9	88.0	55.9	86.0	45.6
KARR	103.7	135.1	104.8	139.3	-162.8	-167.8	-162.8	-173.7
	100.5	100.3	97.7	100.1	-140.9	-160.3	-141.4	-171.8
	0.0043	0.0008	0.0013	0.0002	0.0042	0.0044	0.0014	0.0010
	0.0022	0.0006	0.0005	0.0002	0.0031	0.0019	0.0010	0.0004
	0.0016	0.0008	0.0003	0.0002	0.0007	0.0007	0.0003	0.0002
MAC1	100.1	96.8	76.7	85.4	7.2	4.7	7.2	3.2
	103.6	138.1	86.9	141.5	-171.2	163.0	-172.9	154.3
	49.2	116.7	20.5	121.5	32.5	20.5	31.1	19.6
	0.0173	0.0095	0.0031	0.0027	0.0105	0.0074	0.0034	0.0016
	0.0019	0.0010	0.0003	0.0003	0.0013	0.0008	0.0004	0.0002
MAW1	0.0073	0.0037	0.0014	0.0010	0.0018	0.0012	0.0006	0.0002
	-129.5	-57.9	-161.2	-52.3	-2.0	-9.0	-2.3	-11.9
	-108.5	-52.7	-125.4	-47.8	154.8	146.6	154.6	142.2
	-120.7	-61.8	-147.8	-57.2	-15.2	-40.0	-17.0	-49.5
	0.0136	0.0050	0.0034	0.0014	0.0074	0.0073	0.0025	0.0018
	0.0014	0.0009	0.0001	0.0003	0.0009	0.0009	0.0003	0.0002
	0.0027	0.0008	0.0006	0.0002	0.0015	0.0012	0.0005	0.0003
	-155.1	-124.0	-175.4	-123.6	50.1	27.7	48.7	21.2
	34.5	139.0	-10.1	145.8	-89.7	-106.1	-90.6	-113.6
	121.8	143.1	109.3	145.1	175.3	157.9	174.8	149.4
	0.0037	0.0016	0.0014	0.0005	0.0086	0.0095	0.0029	0.0023

Table C.3 Ocean Loading Tide Coefficients for ARGN Stations using GOT99.2b model.

Site	M2	S2	N2	K2	K1	O1	P1	Q1
ALIC	0.0028	0.0011	0.0008	0.0002	0.0022	0.0025	0.0008	0.0007
	0.0017	0.0008	0.0003	0.0002	0.0017	0.0010	0.0006	0.0002
	0.0003	0.0001	0.0001	0.0000	0.0008	0.0007	0.0003	0.0002
	148.4	-48.8	110.4	-59.2	4.2	8.4	4.6	4.1
	83.5	110.2	77.1	104.6	-170.6	173.5	-171.6	158.5
CAS1	-127.4	80.3	-160.5	-163.5	-87.6	-112.3	-89.6	-131.1
	0.0080	0.0042	0.0022	0.0012	0.0115	0.0110	0.0039	0.0025
	0.0027	0.0012	0.0006	0.0004	0.0009	0.0009	0.0003	0.0002
	0.0019	0.0012	0.0005	0.0004	0.0021	0.0021	0.0007	0.0005
	-29.3	21.4	-50.6	27.4	57.9	49.1	57.0	43.3
CEDU	-157.3	-101.8	178.2	-101.7	27.6	-19.3	23.1	-33.1
	-25.6	26.4	-43.5	29.7	63.1	53.0	62.1	46.2
	0.0026	0.0033	0.0006	0.0008	0.0053	0.0051	0.0018	0.0013
	0.0019	0.0011	0.0004	0.0003	0.0017	0.0011	0.0005	0.0002
	0.0007	0.0010	0.0002	0.0003	0.0018	0.0014	0.0006	0.0004
COCO	-175.9	-66.2	83.3	-68.6	46.6	33.4	45.3	23.8
	100.6	115.3	117.8	111.7	-168.9	-179.1	-169.6	171.9
	112.5	118.1	170.5	123.0	-111.3	-130.2	-112.9	-145.4
	0.0216	0.0082	0.0048	0.0022	0.0117	0.0078	0.0038	0.0015
	0.0055	0.0028	0.0010	0.0008	0.0015	0.0010	0.0005	0.0002
DARW	0.0019	0.0009	0.0004	0.0003	0.0010	0.0004	0.0003	0.0001
	120.0	143.4	109.1	149.8	-13.6	-23.6	-14.3	-39.1
	-121.7	-78.9	-136.5	-83.2	20.3	4.2	19.2	-6.0
	-123.5	-100.3	-130.3	-107.2	112.5	116.9	112.6	149.5
	0.0055	0.0024	0.0014	0.0006	0.0073	0.0058	0.0024	0.0014
DAV1	0.0017	0.0006	0.0004	0.0001	0.0037	0.0021	0.0012	0.0004
	0.0019	0.0010	0.0004	0.0003	0.0012	0.0009	0.0004	0.0002
	69.3	61.9	55.3	82.4	8.2	-2.3	7.3	-5.6
	129.3	-176.9	111.0	-177.5	-171.4	165.8	-172.8	155.4
	20.2	87.9	-10.2	86.9	8.2	-6.8	7.0	-10.3
HOB2	0.0060	0.0034	0.0021	0.0011	0.0098	0.0104	0.0034	0.0024
	0.0003	0.0007	0.0001	0.0002	0.0011	0.0012	0.0004	0.0003
	0.0026	0.0012	0.0007	0.0003	0.0014	0.0018	0.0005	0.0004
	7.9	121.2	-22.9	123.2	78.9	75.9	78.6	71.0
	-60.0	11.1	-163.7	6.3	10.9	-25.6	7.0	-36.8
JAB1	14.7	92.7	-10.7	92.1	89.4	83.0	88.6	75.5
	0.0100	0.0015	0.0025	0.0002	0.0073	0.0066	0.0024	0.0018
	0.0042	0.0017	0.0008	0.0005	0.0012	0.0006	0.0004	0.0001
	0.0011	0.0007	0.0002	0.0002	0.0015	0.0012	0.0005	0.0003
	153.1	-105.7	130.4	-138.8	88.4	56.9	85.6	44.6
KARR	104.8	136.2	107.3	130.8	-162.1	-166.8	-162.4	173.6
	101.7	100.9	94.3	100.7	-141.6	-160.5	-143.2	-172.4
	0.0046	0.0008	0.0013	0.0002	0.0040	0.0043	0.0014	0.0011
	0.0023	0.0007	0.0005	0.0002	0.0032	0.0019	0.0010	0.0004
	0.0016	0.0007	0.0003	0.0002	0.0007	0.0007	0.0002	0.0002
MAC1	99.2	46.6	77.7	104.5	9.7	6.7	9.4	1.7
	104.2	139.7	88.9	128.9	-170.2	163.4	-171.8	150.0
	48.5	112.0	18.9	113.8	31.9	22.7	30.9	20.9
	0.0170	0.0098	0.0031	0.0027	0.0106	0.0074	0.0035	0.0017
	0.0019	0.0010	0.0003	0.0003	0.0013	0.0008	0.0004	0.0002
MAW1	0.0073	0.0037	0.0014	0.0010	0.0019	0.0012	0.0006	0.0002
	-130.0	-56.0	-162.7	-62.7	-1.7	-8.6	-2.2	-17.6
	-109.9	-54.2	-128.6	-57.5	155.2	146.9	154.7	133.0
	-120.8	-61.0	-148.1	-67.2	-15.5	-39.3	-17.0	-59.5
	0.0135	0.0049	0.0034	0.0013	0.0075	0.0074	0.0025	0.0019
	0.0014	0.0010	0.0001	0.0002	0.0009	0.0009	0.0003	0.0002
	0.0028	0.0008	0.0005	0.0002	0.0015	0.0012	0.0005	0.0003
	-155.2	-119.3	-175.9	-131.7	51.6	28.9	49.3	21.6
	33.2	141.5	-19.2	144.6	-91.8	-103.5	-93.0	-116.4
	120.6	141.9	108.2	128.9	174.6	159.3	173.4	147.8
	0.0037	0.0017	0.0015	0.0006	0.0087	0.0097	0.0030	0.0023

Table C.4 Ocean Loading Tide Coefficients for ARGN Stations using NAO.99b model.

Site	M2	S2	N2	K2	K1	O1	P1	Q1
ALIC	0.0026	0.0010	0.0008	0.0003	0.0023	0.0025	0.0007	0.0007
	0.0017	0.0008	0.0003	0.0002	0.0017	0.0010	0.0005	0.0002
	0.0003	0.0001	0.0001	0.0000	0.0009	0.0007	0.0003	0.0001
	150.7	-55.8	115.6	-56.7	2.4	8.4	3.7	4.3
	83.0	112.3	78.2	109.1	-170.7	173.0	-171.3	162.7
CAS1	-125.5	81.9	-158.0	87.0	-86.2	-112.4	-86.5	-127.5
	0.0084	0.0040	0.0022	0.0011	0.0122	0.0113	0.0040	0.0025
	0.0027	0.0012	0.0006	0.0003	0.0009	0.0011	0.0003	0.0002
	0.0021	0.0011	0.0005	0.0003	0.0022	0.0021	0.0007	0.0005
	-32.3	23.3	-53.4	19.0	58.0	50.8	57.9	44.8
CEDU	-157.8	-101.6	177.2	-104.8	21.8	-19.6	17.7	-35.7
	-27.9	25.3	-47.7	21.0	63.9	55.5	63.7	48.3
	0.0026	0.0032	0.0006	0.0010	0.0052	0.0051	0.0017	0.0012
	0.0019	0.0011	0.0004	0.0003	0.0016	0.0010	0.0005	0.0002
	0.0007	0.0010	0.0002	0.0003	0.0018	0.0014	0.0006	0.0003
COCO	-170.9	-71.8	84.4	-72.8	44.7	32.8	44.6	25.4
	100.2	114.9	117.0	111.2	-168.7	-179.3	-168.9	172.7
	109.8	112.4	172.4	110.7	-112.0	-132.3	-112.2	-142.7
	0.0213	0.0080	0.0047	0.0022	0.0116	0.0077	0.0037	0.0016
	0.0055	0.0029	0.0010	0.0008	0.0015	0.0010	0.0005	0.0002
DARW	0.0019	0.0009	0.0004	0.0003	0.0010	0.0004	0.0003	0.0001
	119.8	140.5	109.3	134.9	-13.0	-22.4	-13.1	-30.4
	-121.9	-79.2	-137.2	-82.5	18.6	3.9	17.6	-0.8
	-123.3	-99.6	-130.5	-104.2	113.1	120.1	110.7	151.5
	0.0052	0.0020	0.0017	0.0005	0.0080	0.0061	0.0025	0.0014
DAV1	0.0015	0.0006	0.0004	0.0002	0.0036	0.0021	0.0011	0.0004
	0.0018	0.0009	0.0004	0.0002	0.0013	0.0009	0.0004	0.0002
	78.8	82.7	68.4	88.0	1.1	-4.4	0.4	-8.0
	129.0	-162.2	108.7	-162.0	-174.6	165.4	-176.3	160.1
	15.4	92.0	2.3	102.4	-0.5	-9.7	-1.8	-15.8
HOB2	0.0066	0.0032	0.0021	0.0010	0.0105	0.0105	0.0034	0.0024
	0.0004	0.0006	0.0001	0.0002	0.0012	0.0014	0.0004	0.0003
	0.0027	0.0012	0.0007	0.0003	0.0015	0.0019	0.0005	0.0004
	6.8	118.4	-22.9	116.3	82.5	81.8	83.1	76.9
	-77.0	11.0	-164.2	8.3	4.1	-22.7	2.4	-35.7
JAB1	12.1	90.1	-13.5	88.2	91.7	87.3	92.9	78.8
	0.0097	0.0017	0.0024	0.0004	0.0072	0.0066	0.0023	0.0015
	0.0042	0.0017	0.0008	0.0005	0.0012	0.0006	0.0004	0.0001
	0.0012	0.0007	0.0002	0.0002	0.0015	0.0013	0.0005	0.0003
	154.3	-116.4	130.9	-108.8	87.4	56.7	85.3	46.6
KARR	104.1	137.3	105.5	134.9	-162.0	-166.0	-161.8	-173.4
	103.7	99.2	95.3	92.4	-139.9	-160.1	-140.4	-170.1
	0.0047	0.0005	0.0015	0.0001	0.0046	0.0045	0.0015	0.0012
	0.0023	0.0007	0.0004	0.0002	0.0032	0.0019	0.0010	0.0004
	0.0016	0.0008	0.0004	0.0002	0.0007	0.0008	0.0003	0.0002
MAC1	104.5	107.9	82.7	147.7	3.0	3.7	3.7	-3.1
	97.1	131.8	82.8	119.0	-174.4	162.9	-176.2	154.8
	49.9	117.5	23.0	123.5	19.2	20.9	19.9	11.4
	0.0169	0.0095	0.0031	0.0028	0.0105	0.0075	0.0033	0.0017
	0.0019	0.0010	0.0003	0.0003	0.0013	0.0008	0.0004	0.0002
MAW1	0.0071	0.0037	0.0014	0.0010	0.0018	0.0012	0.0006	0.0002
	-131.4	-58.6	-165.4	-60.7	-2.4	-8.8	-2.6	-12.9
	-107.2	-52.9	-125.1	-55.1	155.8	147.1	156.1	138.7
	-122.6	-63.7	-150.9	-66.7	-16.8	-40.1	-18.7	-48.0
	0.0136	0.0050	0.0033	0.0014	0.0075	0.0076	0.0025	0.0017
	0.0013	0.0009	0.0001	0.0003	0.0010	0.0009	0.0003	0.0002
	0.0027	0.0008	0.0005	0.0002	0.0015	0.0013	0.0005	0.0003
	-154.1	-123.2	-175.9	-129.9	51.1	27.4	48.8	21.7
	33.6	139.7	0.3	139.8	-91.6	-102.3	-91.4	-114.2
	119.5	142.1	107.0	137.4	173.6	159.3	174.1	144.5
	0.0039	0.0017	0.0015	0.0006	0.0090	0.0097	0.0030	0.0022

